Ph.D. Thesis

Eran Kot

Efficient interfacing of light and surface plasmon polaritons for quantum optics applications

Danish National Research Foundation Centre for Quantum Optics (QUANTOP)
Niels Bohr Institute
Graduate School of Science
Faculty of Science
University of Copenhagen

Eran Kot
Copenhagen, September 21, 2012

Principal academic supervisor: Anders S. Sørensen
Thesis submitted : September 21, 2012

Abstract

The research of light and matter interactions is the most fascinating and powerful tool in advancing our understanding of both atomic and light physics. From the pioneering work of Niels Bohr in devising a model for the atom to recent research in manipulation of single atoms, light matter interaction are the window to the underlying quantum world. It is no surprise then that there has always been push to find more, and gain better control over systems in which this interaction can be studied. In the past two decades, this end was further motivated as applications were envisioned to coherent control of matter. These include applications such as efficient photon collection, single-photon switching and transistors, and long-range optical coupling of quantum bits for quantum communications. However, generating and controlling strong coherent interaction between otherwise very weakly interacting light and quantum emitters proves a difficult task. Current days solutions range from cavities, atomic ensembles, photonic band gaps structures, ion traps and optical latices are all being improved and studied but none has yet to emerge as superior.

Recently, another proposal for such a strong coupling system has been put forward. By exploiting the strong confinement of light in a surface plasmon mode, a cavity-free, broadband tool can be designed to engineer the light-emitter interaction in the vicinity of metallic nano-structures. These surface plasmons, hybrid waves of light and electronic oscillations propagating on the surface of metals have been shown to be useful in coupling to quantum dots, nanodiamond NV-centers defects and other quantum emitters. However, being lossy these modes too need to be efficiently coupled out to photons in order to facilitate experimental control of the system. This have proved to be the Achilles heel of this application.

In this thesis we study the interaction of surface plasmons on nanometallic structures and light. We suggest two configurations in which efficient coupling to the surface plasmon modes can be achieved on the nanoscale, allowing to transfer single photons from one mode to the other. The first, applicable to plasmonic guides, exploits the phenomena of adiabatic following to transfer the plasmonic excitation to an adjacent photonic waveguide by slowly tapering the plasmonic guide into and then out of resonance with the photonic guide. For this end we develop a general perturbative description for guides of arbitrary cross section, and go on to apply it to slab guides showing up to 90% coupling efficiencies for realistic experimental parameters. The second coupling configuration suggested is a plasmonic coupling lens, constructed around the emitter in a proximity to a metallic interface. Concentric grating rings then couple light propagating normal to the surface to a inward propagating plasmons, showing coupling efficiencies of 70% and enhancement of the emitters decay rate by up to 45 times that of the isolated emitter's decay rate.

Finally, we explore a nonclassicality criterion for the state of a continuous variable, local system. This is done by inferring the breakdown of classical models from quadrature measurements, expressed as the lack of

a proper distribution function of the underlying generalized coordinates. This provides a useful tool in characterizing new candidate systems for quantum applications and by its simplicity, also furthers the understanding of the quantum-classical transition.

Sammendrag

Forskningen i vekselvirkningen mellem lys og stof er et fascinerende og kraftfuldt værktøj til at forstå både atomfysik og optisk fysik. Fra Niels Bohrs banebrydende arbejde med at udtænke en model for atomet til nutidens forskning i at manipulere enkelte atomer, har lys-stof vekselvirkninger været vinduet til den underliggende kvanteverden. Det er ikke overraksende, at man altid har stræbt efter at få bedre kontrol over eksisterende systemer samt at finde nye systemer til at studere disse vekselvirkninger med. I de seneste to årtier er motivationen for dette blevet styrket, idet nye anvendelsesmuligheder for kohærent kontrol af stof er blevet udviklet. Disse anvendelser er effektiv fotonopsamling, enkelt-foton opererede kontakter og transistorer samt langtrækkende, optiske koblinger mellem kvante-bits, der bruges til kvantekommunikation. Det har dog vist sig at være særdeles udfordrende at skabe og kontrollere stærke kohærente vekselvirkninger mellem normalt meget svagt vekselvirkende lys og kvante-emitters. Nutidens løsninger tæller optiske kaviteter, atomare ensembler, fotoniske båndgabsstrukturer, ionfælder og optiske gitre. De er alle blevet nøje studeret og forbedret, men ingen har endnu vist sig som den ideelle løsning.

For nylig blev et nyt forslag til et stærk-kobling-system foreslået. Ved at udnytte den meget stærke indespærring af lys i en plasmonisk overfladetilstand, kan man udvikle et kavitets-fri, bredbåndet værktøj til at designe lys-emitter vekselvirkninger nær ved metalliske nanostrukturer. Disse plasmoner, hvilket er hybridbølger mellem lys og elektroniske svinginger som bevæger sig på overfladen af metaller, har vist sig at være nyttige til at koble kvante-dots, nanodiamant NV-center defekter og andre kvante-emittere. På grund af tab skal plasmonerne dog kobles effektivt til fotoner for at give eksperimental kontrol over systemerne. Dette har vist sig at være forslagets Achilleshæl.

I denne afhandling undersøger vi vekselvirkningen mellem overfladeplasmoner på nanometalliske strukturer og lys. Vi foreslår to konfigurationer, hvor effektiv kobling til overflade-plasmonerne kan opnås på nanoskala, hvilket muliggør overførsel af enkel-fotoner fra en tilstand til en anden. Den første konfiguration, anvendelig for plasmonisk bølgeledere, udnytter fænomenet adiabatisk følgen til at overføre plasmoniske eksitationer til en tilstødende fotonisk bølgeleder ved langsomt at bringe den plasmoniske bølgeleder ud og ind af resonans med den fotoniske bølgeleder. I forbindelse med dette, udvikler vi en generel pertubativ beskrivelse af bølgeledere med arbitrært tværsnit og ved at anvende denne på plane bølgeledere, viser vi op til 90% koblingseffektivitet for realistiske eksperimentelle parametre. Den anden koblingskonfiguration, som vi foreslår, er en plasmoniske koblingslinse konstrueret omkring emitteren i nærheden af en metalliske grænseflade. Koncentriske, indridsede ringe kobler lys,

der bevæger sig vinkelret på overfladen til indadgående plasmoner med koblingseffektiviteter på 70% og en forbedring af emitterens henfaldsrate med op til 45 gange i forhold til en isoleret emitters henfaldsrate.

Til sidst undersøger vi et kriterium for ikke-klassisk beskrivelse af tilstanden af et lokalt, kontinuært-variabel system. Dette gøres ved at udlede de klassiske modellers sammenbrud ud fra kvadraturmålinger, der udtrykker en manglende fordelingsfunktion for de underliggende generelle koordinater. Dette giver et nyttigt værktøj til at karakterisere nye anvendelige kvantesystemer, og dets enkelthed giver bedre forståelse for grænsen mellem kvantemekanik of klassisk fysik.

Acknowledgements

The work presented here is the result of three and a half years of research at the Danish National Research Foundation Center for Quantum Optics (QUANTOP). This has been a fascinating period for me, in which I have learned and grew wise in more than just the accumulated knowledge I have gained.

First and foremost I wish to thank my supervisor, professor Anders S. Sørensen. Anders' supervision has been that of patience and encouragement. His deep understanding of the field and his true enjoyment of discussing physics has made the time spent at the Niels Bohr Institute into an enlightening tour through this intriguing field of quantum optics and atomic physics. This experience was further intensified by the stimulating discussions I have had over the years within the theoretical optics group. I had the pleasure to work side by side with a very talented group of researchers. Martjin Wubs, Dirk Witthaut, Jonatan Bohr Brask, Anna Grodecka-Grad, Florentin Reiter, Johannes Borregaard and Emil Zeuthen to name them, have made every paper, seminar and even coffee breaks into a potential long and fascinating conversation emerging out of the core physics, curiosity. But the uniqueness of QUANTOP under the leadership of professor Eugene Polzik is in the bringing together experiments and theory together in a few of the most novel systems this research field has to offer. This also draws in the most talented and interesting people, and I am very thankful to have gotten to know them, both professionally, but mostly personally. This group is a home away from home in its hospitalities and warmth, and I am proud to have been a part of it and in calling its members friends and colleagues.

I wish to thank the Willum Kann Rasmussen foundation for funding this great adventure.

And finally, I extend my warmest thanks to my family and friends for all the support I received during this long journey.

Contents

Publications

Peer reviewed

1. Eran Kot, Niels Grønbech-Jensen, Bo M. Nielsen, Jonas S. Neergaard-Nielsen, Eugene S. Polzik and Anders S. Sørensen,
Breakdown of the classical description of a local system
Phys. Rev. Lett. 108, 233601 (2012)

Abbreviations and Acronyms

BS Beam Splitter

DOS Density of Sates

EOT ExtraOrdinary Transmission
LDOS Local Density of States
LO Local Oscillator

NA Numerical Aperture
NBI Niels Bohr Institute (organisation)
NV Nitrogen Vacancy

QUANTOP Danish National Research Foundation Centre for Quantum Optics (organisation)

SPP Surface Plasmon Polariton
SNOM Scanning Near-field Optical Microscopy

TE Transverse Electric
TM Transverse Magnetic

Chapter 1

Introduction

1.1 Motivation

That Quantum mechanics is quite different in its predictions is by now well understood. Recent years have seen the ideas and limits of quantum mechanics implemented in a wide range of system no one has envisioned. From nanomechanical devices through gravitational interferometry to precise measurement, the gain earned by the constant improvement of both scientific and technological control over coherent processes seems to be increasing steadily. This has also drove the search for ever new, and bigger system manifesting quantum behavior. The past decade saw numerous candidates systems emerging. Plasmonic systems ([Zayats03]), photonic crystals ([Sakoda05]), tapered optical nanofibers ([Tong03]), and metamaterials ([Smith04]) are all being actively studied for their potential to manipulate light-matter interactions.

As these proposals accumulate, their actual implementation does at time encounters more difficulties than was is suggested by the initial idea. These difficulties require a more detailed research into the specific systems and are often a opportunity to examine both the underlying physics of the actual experimental setup, and the and the foundations of the abstract idea to be implement. From it first proposal as a candidate for the research of light matter interaction in the strong coupling regime in the middle of the last decade ([Chang06, Akimov07]), through research efforts in implementations (e.g., [Huck09, Falk09, Kolesov09]) and suggested future directions of research([Dzsotjan10, Gonzalez-Tudela11]), quantum plasmonics seems yet to have reached the full potential as a research tool in the field of quantum optics. It is the aim of this work to examine one of the problems in this field, namely that of the surface plasmon-light coupling, and to suggest ways to overcome it.

1.2 Surface plasmon polaritons

When considering the response of the free electrons in a metal to electromagnetic waves, one interesting result is they respond out of phase to the driving of electric field. This can be seen, for example, from the Drude model considering the electrons equation of motion with a damp-

ing force:

$$\epsilon(\omega) = 1 - \frac{\omega_p^2}{\omega^2 + i\Gamma\omega}, \tag{1.1}$$

with $\omega_p^2 = 4\pi n e^2/m_e$ being plasma frequency at the equilibrium density n. This means that the real part of the dielectric constant is negative. This has two interesting results: the first, as is well known, is that the electromagnetic cannot penetrate into the metal beyond the so called skin depth. The refractive index of the of the metal is imaginary, $n = \sqrt{\epsilon}$. The imaginary part of the dielectric constant also leads to dissipation of energy in the metal.

There is, however, a much more interesting result, hinted already in the appearance of the natural frequency above. To see this, consider the flat interface between two dielectric materials of dielectric constants ϵ_d and ϵ_m. As we shall consider this problem in detail in the following work, we not solve it to the full here but rather aim at the general idea. With the understanding that we are looking for a surface wave of the electrons, driven by the electromagnetic field, we assume there exist a solution to the homogeneous macroscopic Maxwell equation on the surface

$$\nabla \times \nabla \times \mathbf{E} - \frac{\omega^2\epsilon}{c^2}\mathbf{E} = 0 \tag{1.2}$$

which propagates in the along the surface, but decays exponentially away form the surface, in both directions,

$$\mathbf{E} \propto e^{ikx - \kappa|z|}, \tag{1.3}$$

where the interface was chosen as the XY plane. The first thing to note, when comprising solutions of this kind is that because of the continuity of the the electric field parallel to the surface, no transverse electric (TE) solutions exist. This will somewhat simplify our account in chapter 2. The resulting boundary conditions for our problem are

$$E_{d,x} - E_{m,x} = 0 \tag{1.4}$$

$$\epsilon_d E_{d,z} - \epsilon_m E_{m,z} = 0 \tag{1.5}$$

leading to the dispersion relation

$$\epsilon_d \kappa_m - \epsilon_m \kappa_d = 0. \tag{1.6}$$

Since we are looking for decaying solutions in both directions, κ are both real and positive. Therefore, such waves exist on the surface of metal, obeying the dispersion relation (1.6). This means that their propagation constant is determined by

$$k^2 = \frac{\epsilon_d\epsilon_m}{\epsilon_d + \epsilon_m}\frac{\omega^2}{c^2}, \qquad \kappa_i^2 = \frac{-\epsilon_i^2}{\epsilon_d + \epsilon_m}\frac{\omega^2}{c^2}, \tag{1.7}$$

Which can be seen to always be bigger than the wave number of a photon of the same frequency. The lateral decay is what makes the plasmon so attractive to our proposes - the higher the propagation constant k is the more confined is the electric field around the surface, generating higher

intensities and smaller mode volume generating stronger and stronger interaction with adjacent atoms.

The is a price to pay, though, hidden within the the above relations. As stated the metal dielectric constant is accompanied by an imaginary part, representing dissipation in the metal. If the dielectric constant is written as $\epsilon_m = \bar{\epsilon}_m + i\bar{\bar{\epsilon}}_m$ then the propagation constant is

$$\Re\{k\} = \sqrt{\frac{\bar{\epsilon}_m \epsilon_d}{\bar{\epsilon}_m + \epsilon_d}} \frac{\omega}{c} \tag{1.8}$$

$$\Im\{k\} = \sqrt{\frac{\bar{\epsilon}_m \epsilon_d}{\Re\bar{\epsilon}_m + \epsilon_d}} \frac{\bar{\bar{\epsilon}}_m \epsilon_d}{2\bar{\epsilon}_m(\bar{\epsilon}_m + \epsilon_d)} \frac{\omega^2}{c^2}. \tag{1.9}$$

The higher the confinement of the field at the surface, the lossier is the mode becoming. Therefore, any surface plasmon device for strong coupling to the quantum emitters will suffer propagation losses, and it is the need to extract the plasmonic excitation onto a photonic state that we were set to solve with this work.

1.3 Interaction with single emitters

1.3.1 The Purcell effect and the modification of the decay rate in the proximity of a dielectric/metallic body

The key advantage of plasmons to surface quantum optics applications is the coupling of the strongly confined fields of the *SPP* excitation to an adjacent emitter. In this section we first describe the influence of the local density of states on the emission of a dipole. The methods reviewed here will also prove useful in calculating the decay rate of an emitter above the plasmonic lens presented in chapter (3).

We start by considering the classical dipole. In classical electromagnetic theory the dipole is the lowest order term of the current distribution when expanded in the distance from the source. For harmonic time dependence $\propto e^{-i\omega t}$, it can be written as

$$\mathbf{j}(\mathbf{r}) = -i\omega \mathbf{p} \delta(\mathbf{r} - \mathbf{r}_0). \tag{1.10}$$

Which, when plugged into the expression for the fields when those are written in the Green's function formalism are simplified to

$$\mathbf{E}(\mathbf{r}) = i\frac{1}{c}\mu \int_V \mathbf{G}(\mathbf{r}, \mathbf{r}')\mathbf{j}(\mathbf{r}') = \frac{\omega^2}{c}\mu \mathbf{G}(\mathbf{r}, \mathbf{r}_0)\mathbf{p} \tag{1.11}$$

$$\mathbf{H}(\mathbf{r}) = \frac{\omega}{c}\mathbf{G}(\mathbf{r}, \mathbf{r}_0)\mathbf{p}. \tag{1.12}$$

If we are interested in the energy radiated from away from our classical dipole, the straight forward way will be to integrate the far field Poynting vector (taking only the components proportional to r^{-1} in the fields)

$$\mathbf{S} = \frac{c}{8\pi}\mathbf{E} \times \mathbf{H}, \tag{1.13}$$

around the dipole. However, this becomes tricky when the dipole is embedded in an inhomogeneous environment. The total fields need to be calculated everywhere on the enclosing surface. Instead, Poynting theorem can be used. Stating the energy conservation, the radiated energy is equal to the energy dissipation given by

$$\frac{dW}{dt} = -\frac{1}{2}\int \Re\{\mathbf{j}^* \cdot \mathbf{E}\} dV, \tag{1.14}$$

V being the source volume. For our dipole this is just

$$\frac{dW}{dt} = \frac{\omega}{2}\Im\left\{\mathbf{p}^* \cdot \mathbf{E}(\mathbf{r}_0)\right\} = \frac{\omega^3 |\mathbf{p}|^2}{2c^2}\left[\hat{p}\Im\left\{\mathbf{G}(\mathbf{r}_0, \mathbf{r}_0)\right\}\hat{p}\right], \tag{1.15}$$

where $\hat{p}$ is the unit vector in the dipole direction. Using this relation, the calculation of the decay of the dipole now reduces to calculation of the electric field at the dipole's position.

Dependence on the density of states, and the mode volume of a specific mode

In quantum theory, the interaction between a two level system and the radiation field is described in the dipole approximation by the Hamiltonian term

$$H = -\mathbf{p} \cdot \mathbf{E}, \tag{1.16}$$

where this time the field and dipole are to be understood as the second quantization operators

$$\mathbf{p} = \vec{p}^*|e\rangle\langle g| + \vec{p}|g\rangle\langle e|, \qquad \mathbf{E} = \sum_k \left(\mathcal{E}_k^+ a_k(t) + \mathcal{E}_k^- a_k^\dagger(t)\right). \tag{1.17}$$

The notation $\vec{p}$ was introduced to distinguish between the operator and the classical vector and summation on in the field operator is done over all radiation modes.

For an initial state of the two level system in the excited state and no excitation in the radiation field, the decay rate of the dipole can be calculated using the Fermi golden rule:

$$\begin{aligned}\Gamma &= \frac{2\pi}{\hbar^2}\sum_f |\langle f|H|e, \{0\}\rangle|^2 \delta(\omega_{eg} - \omega_f) = \\ &= \frac{2\pi}{\hbar^2}\sum_k \left[\vec{p}^* \cdot \mathcal{E}_k^+ \mathcal{E}_k^- \cdot \vec{p}\right]^2 \delta(\omega_{eg} - \omega_k)\end{aligned} \tag{1.18}$$

However, using the normal mode expansion, $\mathcal{E}_k^+ = \sqrt{\frac{\hbar\omega_k}{2\epsilon_0}}\mathbf{u}_k$ the sum over the modes can be written as

$$\Im\{\mathbf{G}(\mathbf{r}, \mathbf{r})\} = \frac{\pi c^2}{2\omega}\sum_k \mathbf{u}_k^* \mathbf{u}_k \delta(\omega - \omega_k). \tag{1.19}$$

This finally enables us to write

$$\Gamma = \frac{2\omega_{eg}^2}{\hbar c^2}|p|^2\left[\hat{p}^*\Im\mathbf{G}(\mathbf{r}_0, \mathbf{r}_0)\hat{p}\right] \tag{1.20}$$

Thus, the decay rate of the emitter depends on the environment. The enhancement of the decay rate by a near by surface of a dielectric is used in enhancing the Raman scattering from vibrational modes of molecules, for example. The importance of this result is in that it enables the calculation of the spontaneous decay rate in arbitrary setting, all that is need is the Green function of the system.

Another essential feature to the work described here, is the equivalence of the classical and quantum mechanical descriptions for the interaction of a two level systems with the radiation fields. As the key ingredient to both calculations is the classical Green's function, and we shall focus in this work on its calculation. We therefore preform all the calculation presented in the classical regime, solving the Maxwell equations.

The above result is at the heart of many systems used in quantum optics. The emission rate is directly proportional to the local density of optical states (LDOS)

$$\rho_\mu(\mathbf{r},\omega) = 3\sum_k \left[\mathbf{n}_\mu \cdot (\mathbf{u}_k^* \mathbf{u}_k) \cdot \mathbf{n}_\mu\right] \delta(\omega - \omega_k), \tag{1.21}$$

and so by engineering the local density of states around the emitter the decay rate can be controlled. This is done for example by placing the emitter in a photonic crystals [Sakoda05], inside a hollow core fibers [Knight03] or in the vicinity of of a tapered dielectric nanofiber [Vetsch10]. However, the diffraction limit is still the lower limit for any mode volume, and thus an upper limit to the enhancement of the local density of states.

1.3.2 Coupling of the single emitter to a nanowire

The advantage of *SPP* in control of the emission of single emitters was suggested by Chang [Chang07a], Akimov [Akimov07]. In these works, the emission properties of a nanoscale optical emitter were shown to be significantly modified by the proximity of a nanowire that supports surface plasmons. As the mode volume is smaller than the wavelength squared, the diffraction can be circumvented and the coupling to the plasmonic mode can be made to dominate the emitters decay process. For its importance to the work presented here, we shall review and the resulting decay rates of a closely placed single emitter. In their papers, Chang *et al.* analyzed the normal modes of a metallic nanowire (similar calculations where performed for a dielectric nanofiber in [Klimov04]). In the following we will consider the nanowire to have a dielectric constatnt ϵ_m embbeded in a surounding of dielectric constant ϵ_d. The basic guided plasmonic modes, satisfying the dispersion relation

$$\frac{k_m^2}{k_{m,\perp}} \frac{J_0'(k_{m,\perp}R)}{J_0(k_{m,\perp}R)} - \frac{k_d^2}{k_{d,\perp}} \frac{H_0'(k_{d,\perp}R)}{H_0(k_{d,\perp}R)} = 0 \tag{1.22}$$

with H_0, J_0 the Hankel and Bessel functions, prime denoting a derivation with respect to the functions argument, $k_i = \sqrt{\epsilon_i} k_0$ and $k_{i,\perp} = \sqrt{k_i^2 - k_\parallel^2}$, was shown not to posses a cutoff, and have an effective refractive index $k_\parallel \propto 1/R$ the radius of the nanowire. Other modes were shown to either

have a cutoff, or to asymptotically approach the wave number of the surrounding medium as the nanowire's radius was reduced. This means two thing contributing to the strong coupling. The first is that the wire can be operatated in a single mode regime, inhibiting the decay into higher modes. For the basic mode, the diverging $k_{\|}$ means tighter confinement as the radius of the wire is reduced, as $\kappa_{\perp}$, the decay length in the transverse direction also scales as R^{-1}. This in turn results in smaller volume and stronger coupling to the mode. This is in contrast to dielectric waveguides, where the index of refraction approaches that of the surrounding bulk wave number. For the photonic waveguide, this means less confinement, and weaker coupling of the guided mode to nanoscale emitters.

The diverging wavenumber of the guided mode in inverse proportionality to the system typical length scale is a key feature for this application. As we shall explore in chapter (2), this also applies to slab plasmonic wave length. This scaling can be understood by considering the electrostatic limit as the system become much smaller than the wavelength, leaving the radius as the only length scale in the problem. It is accompanied by a group velocity proportional to the radius, slowing as the plasmon propagates toward smaller radii. This again can help explain the strong resulting interaction with the localized emitter, as the effective interaction time increases.

Quantifying the decay mechanism to the different channels next to dielectric/metallic cylinder

The decay channels were identified as belonging to one of three distinct modes- radiative processes, resulting in a outgoing photon propagating in the bulk, nonradiative, thermal loses to the metal and decay into guided plasmonic mode.

The decay into the radiation modes can be calculated in the far field away from the wire, as this is the only channel by which energy transport far from the source can occur. In this limit, the total radiation can be seen as coming from a dipole, combining the the source and the reflecting field

$$\Gamma_{rad} \propto |\mathbf{p}_0 + \delta\mathbf{p}|, \tag{1.23}$$

with $\mathbf{p}_0 = p_0\hat{\rho}$ being the source dipole. The reflected dipole contribution was shown to be [Klimov04]

$$\delta\mathbf{p} = p_0 \frac{\epsilon - 1}{\epsilon + 1} \frac{R^2}{d^2} \hat{\rho} \tag{1.24}$$

here $\epsilon \equiv \epsilon_m/\epsilon_d$, R is the nanowire radius and d is the distance between the dipole and the wire axis of symmetry ($d \geq R$). This gives a total decay rate (relative to the isolated dipole source) of

$$\frac{\Gamma_{rad}}{\Gamma_0} \approx \left| 1 + \frac{\epsilon - 1}{\epsilon + 1} \frac{R^3}{d^3} \right|^2 < 4. \tag{1.25}$$

The addition of the metallic nanowire is seen to be able to change the radiative decay rate, but in a limited way.

Another decay mechanism considered is that of nonradiative modes originating in the joule heating of the metal/dielectric. As the emitter is brought closer to the wire surface, its near fields induce strong currents in the metal which dissipate. The resulting decay rate is then calculated by considering the near field in the vicinity of the surface $h \equiv (d - R) \to 0$ of all modes, including those cutoff. This results in

$$\frac{\Gamma_{non-rad}}{\Gamma_0} \approx \frac{3c^3}{16\omega^3 h^3 \epsilon_d^{3/2}} \Im\{\frac{\epsilon - 1}{\epsilon + 1}\}. \tag{1.26}$$

The decay to the non-radiative channel is seen to depend on the dissipative part of the dielectric constant of the metal ($\Im\{\epsilon_m\}$) and decay like h^3 as a function of the distance from the surface. Note, that the geometry of the metallic object does not play a role in the qualitative behavior described in (1.26), and we shall encounter the same behavior discussing the slab plasmonic wave guide in chapter (2).

The contribution of the bound modes (plasmons in the metallic case, guided dielectric waveguide modes in the dielectric cylinder case) confined to the surface of the wire, requires further knowledge of the normal modes of the system. Using the cylindrical coordinate decomposition and the regime at which the wire is a single mode waveguide, Chang *et al.* showed the lowest bounded solution to have the form

$$\mathbf{E} = \Theta(\rho - R)\mathbf{E}_d + \Theta(R - \rho)\mathbf{E}_m \tag{1.27}$$

$$\mathbf{E}_d = b_d \left[\frac{ik_{\parallel} k_{d,\perp}}{k_d^2} H_0'(k_{d,\perp}\rho)\hat{\rho} + \frac{k_{d,\perp}^2}{k_d^2} H_0(k_{d,\perp}\rho)\hat{z} \right] e^{ik_{\parallel} z} \tag{1.28}$$

$$\mathbf{E}_m = b_m \left[\frac{ik_{\parallel} k_{m,\perp}}{k_m^2} J_0'(k_{m,\perp}\rho)\hat{\rho} + \frac{k_{m,\perp}^2}{k_m^2} J_0(k_{m,\perp}\rho)\hat{z} \right] e^{ik_{\parallel} z}. \tag{1.29}$$

The amplitudes are connected via the boundary condition

$$\frac{b_d}{b_m} = \frac{k_{m,\perp}}{k_{d,\perp}} \frac{J_0'(k_{m,\perp}R)}{H_0'(k_{d,\perp}R)}. \tag{1.30}$$

The decomposition allows writing the the Green's function of the nanowire which, in the limit of no dissipation ($\Im\{\epsilon_m\} = 0$) exhibits a pole at the wavenumber corresponding to this mode. The contribution of the plasmonic mode to the decay rate can thus be evaluated by considering (1.20) around this pole. This results in

$$\frac{\Gamma_{spp}}{\Gamma_0} \approx \alpha_{spp} \frac{K_1^2(k_{d,\perp}d)}{(k_0 R)^3} \tag{1.31}$$

where α_{spp} depends only on ϵ_d, ϵ_m. The decay into the plasmonic channel is seen to depend on the the radius of the nanowire like $1/R^3$, and exponentially on the distance of the emitter from the wire. The latter is an indication to the coupling being a result of the tight field confinement.

The different scaling of the decay channels as a function of the geometry of the nanowire allows for optimization of the Purcell factor of the plasmonic channel, defined as $\Gamma_{spp}/(\Gamma_{total} - \Gamma_{spp})$. The advantage of the

plasmonic nano wire demonstrated in the works discussed here was the ability to reach $\Gamma_{spp}/(\Gamma_{total} - \Gamma_{spp}) \approx 5.2 \times 10^2$, equivalent to 99.8% of the emitter energy decaying into the plasmon channel. Note, however, that depends strongly on the orientation of the dipole along the radial direction. The authors suggested using a nanotip to overcome this problem and further increase the coupling. In chapter (3) We suggest yet another way by which the emission of a dipole emitter parallel to the metal-dielectric interface can be strongly coupled to surface plasmon modes.

1.4 Quantum Surface plasmons

1.4.1 Coherent coupling and manifestations of quantum surface plasmon optics

The enhanced coupling in itself is not sufficient for quantum information applications if the coupling is not coherent (as is the case for the radiative and non radiative decay channels discussed above), or if the resulting excitation cannot be manipulated on the quantum mechanics level. the advantage of the strong coupling to the surface plasmon lies in the coherence of the coupling and the control achieved over these excitations.

The quantum nature of a few plasmonic excitations has been researched extensively in recent years. As a first step towards integrating surface plasmons in quantum information systems, the ability to generate, manipulate and measure the quantum nature of the surface plasmons has to be established. In this subsection we mention a few of these results, manifesting the ability to utilize SPPs for quantum optics purposes.

In the experiments aimed at measuring the strong coupling Akimov *et al.* [Akimov07] using chemically grown silver nanowires coated with nanodiamonds containing color nitrogen vacancy (NV) centers as emitters, showed that the resulting radiation scattering of the wire ends bears the signature of the singe emitter. They have demonstrated a Hanbury Brown-Twiss experiment showing no coincidence peak in the intensity correlation function. This indicates the single quantum character of the source is carried coherently by the SPP. Kolesov *et al.* [Kolesov09] went further to show not only that the statistics of the emitter is preserved in the radiation emitted of the ends of the wire, indicating the coherent nature of the coupling between the single emitter and the plasmonic propagating mode, but also the quantum nature of the excitation by demonstrating a self interference of the emitted quantum using the two possible directions of the out going plasmon as the different arms of the beam splitter using the diffraction to show an interference. Together with the particle-like intensity coincidence correlations this has shown the particle wave duality of the SPP, a quantum mechanical feature. Another evidence to the ability to manipulate surface plasmons on the quantum level was demonstrated by Huck *et al.* [Huck09] by demonstrating the ability of a plasmonic guide to preserve the noise features of a non classical beam coupled to it. In their experiment, a light source producing -1.9 ± 0.1dB P-squeezed vacuum was end-coupled to the long range plasmon propagating on the interface of a gold slab. They then measured the light

emitted at the end of the slab and showed that the nonclassical squeezing was preserved. The importance of this work was also in demonstrating that both coupling propagation losses can be modeled as beam splitter losses- incoherence which can be simulated by introducing a mixture of vacuum state.

1.4.2 Quantization of the plasmonic modes

As collective modes of the the electrons and photons, surface plasmon can also be quantized as "quasi-particles". The existence of such quanta is essential if we wish to consider coherent excitations between photons or atomic excitations and the SPP modes. Here we sketch the quantization procedure of SPP.

The appearance of the normal modes in the decomposition 1.17 as basic excitations of Hamiltonian 1.16 is the first step towards the quantization of the plasmonic modes. For the lossless system the linearity of the equations, it would be tempting to replace the c-number amplitudes of the electric field with the creation operators

$$\mathbf{E} = \int_0^\infty \mathbf{E}(\mathbf{r},\omega)d\omega + \int_{-\infty}^0 \mathbf{E}(\mathbf{r},\omega)d\omega \rightarrow \int_0^\infty \hat{\mathbf{E}}(\mathbf{r},\omega)d\omega + h.c. \tag{1.32}$$

However, some care is needed when treating the quantization of the electromagnetic fields in the presence of dielectrics, especially when losses are introduced as is crucial for the case of surface plasmons. the dielectric constant represents the average polarization, but does not account for the noise. Naïve quantization thus leads to decaying operators, as the dissipation is not acompanied by fluctuations.to account for the quantum noise in the dielectric, one adds additional polarization noise to the displacement current

$$\mathbf{D}(\mathbf{r},\omega) = \epsilon\epsilon_0\mathbf{E}(\mathbf{r},\omega) + \mathbf{P}(\mathbf{r},\omega) \tag{1.33}$$

which leads to inhomogeneous macroscopic Maxwell equations

$$\nabla\cdot(\epsilon\epsilon_0\mathbf{E}(\mathbf{r},\omega)) = \rho(\mathbf{r},\omega) \tag{1.34}$$
$$\nabla\times\mathbf{B}(\mathbf{r},\omega) = -i\omega\mu_0\epsilon\epsilon_0\mathbf{E}(\mathbf{r},\omega) + \mu_0\mathbf{j}(\mathbf{r},\omega) \tag{1.35}$$
$$\nabla\cdot\mathbf{B}(\mathbf{r},\omega) = 0 \tag{1.36}$$
$$\nabla\times\mathbf{E}(\mathbf{r},\omega) = i\omega\mathbf{B}(\mathbf{r},\omega). \tag{1.37}$$

with

$$\mathbf{j} = -i\omega\mathbf{P}(\mathbf{r},\omega) \tag{1.38}$$
$$\rho = -\nabla\cdot\mathbf{P}(\mathbf{r},\omega). \tag{1.39}$$

As the current and charge noises added here have to do with the dissipation in the metal, the description is related to the imaginary part of the dielectric constant. It can be shown that the source is associated with a bosonic field

$$\hat{\mathbf{j}}(\mathbf{r},\omega) = \frac{\omega}{\mu_0 c^2}\sqrt{\frac{\hbar}{\pi\epsilon_0}\Im\{\epsilon_m\}}\;\hat{\mathbf{f}}(\mathbf{r},\omega) \tag{1.40}$$

satisfaying the commutation relation

$$[\hat{f}_i(\mathbf{r},\omega),\hat{f}_j^{\dagger}(\mathbf{r}',\omega')] = \delta_{i,j}\delta(\mathbf{r}-\mathbf{r}')\delta(\omega-\omega') \tag{1.41}$$

and diagonalizing the field Hamiltonian

$$H = \int \mathrm{d}^3\mathbf{r} \int_0^{\infty} d\omega\, \hbar\omega \hat{\mathbf{f}}^{\dagger}(\mathbf{r},\omega)\cdot\hat{\mathbf{f}}(\mathbf{r},\omega) \tag{1.42}$$

With the solution of the equation written using the Green's function, the resulting fields can be written as

$$\mathbf{E} = i\omega\mu_0 \int \mathrm{d}^3 r' \overline{\overline{G}}(\mathbf{r}-\mathbf{r}',\omega,\omega')\hat{\mathbf{j}}(\mathbf{r}',\omega') \tag{1.43}$$

$$= i\sqrt{\frac{\hbar}{\pi\epsilon_0}}\frac{\omega^2}{c^2}\int \mathrm{d}^3 r' \sqrt{\Im\{\epsilon_m(\mathbf{r}',\omega')\}}\overline{\overline{G}}(\mathbf{r}-\mathbf{r}',\omega,\omega')\hat{\mathbf{f}}(\mathbf{r}',\omega') \tag{1.44}$$

where $\overline{\overline{G}}$ is the classical dyadic Green's function for the field.

The importance of the second quantization of surface plasmons is that it enables the application of both techniques and schemes developed in quantum electrodynamics (QED). The mapping of the system description onto the basic Hamiltonian of interacting quantized field and a two level atomic system [Dzsotjan10] has allowed the calculation of quantum optical effects in this system. A few examples are spontaneous emission rates [Archambault10], estimation of strong coupling to ensemble of emitters [Gonzalez-Tudela12], of the superradiance regime [Martín-Cano10, Dzsotjan10], suggestion of a two qubit gates [Dzsotjan10], and dissipative entangled state preparation [Martín-Cano11, Gonzalez-Tudela11]. Future possibilities, stemming from this unique channel have also emerged,such as the proposal for a single photon transistor [Chang07b] and photon number resolvers [Witthaut12].

1.5 in- and outcoupling of light to Surface plasmon

Having showed the usefulness of surface plasmons as a quantum interface to single emitters, it remains to show how these excitations are to be coupled out of the system. Due to the dissipative losses discussed in 1.2, in particular in the regime of high confinement at which strong coupling was demonstrated, the *SPP* modes are not suitable as information carriers over distances beyond a few hundreds of a wave lengths. However, if an efficient coupling of free propagating or optically guided photons can be achieved, the plasmonic devices can serve as an effective intermediate step between light and matter qubits, single photon generators, quantum simulators and even quantum computation gates. It is the main aim of the entire work presented here to demonstrate such coupling and the facilitation of such devices.

It is useful however, to discuss first the techniques used in the classical field of plasmonics for surface plasmons excitations. The key for all the

described coupler is that for the photon to couple to a surface plasmon, the momentum gap is to bridged somehow.

As we have seen the surface plasmons can couple efficiently to localized emitters using the strong near field confinement. For this to become a useful tool, they must also be coupled to far field radiation, allowing for them to be recorded and measured. In order to couple and excite surface plasmons, the coupled field must be matched in energy and momentum. We start by looking at the dispersion relation describing the relation between the energy and the momentum of the surface plasmon, as appearing in Eq. (1.9). For a given frequency ω, the wave number in the propagation direction k_z is always larger than the wavenumber of light in the dielectric, which is also clearly visible from Eq. (1.7). As illustrated above this is due to the polariton nature of the plasmon, where the light field has to drag along the massive electrons. This means that free propagating light cannot couple directly to an SPP on a flat surface. Excitation of the SPP can only occur if the momentum of the exciting light can be increased beyond the free space one.

In this section we review some of the means to do so, coupling light to surface plasmon. We start by considering far field excitations using attenuated reflections and grating, describe end coupling to plasmonic waveguides and end with near field excitations using localized sources.

1.5.1 Far field excitation of surface plasmons

Attenuated total reflection (ATR)

One way to compensate the missing momentum of the free propagating light is the usage of evanescent fields. When light propagates in a homogeneous dielectric with a dielectric constant ϵ_p, its wavenumber is $k = \sqrt{\epsilon_p}\omega/c$. Upon impingement at an angle θ on boundary with another dielectric of smaller dielectric constant ϵ_0, the in-plane component of the momentum equals

$$k_z = \sqrt{\epsilon_p}\frac{\omega}{c}\sin(\theta), \tag{1.45}$$

which can be larger than the propagation constant in the dielectric ϵ_0, $k_z > k_0 = \sqrt{\epsilon_0}\frac{\omega}{c}$, corresponding to total internal reflection at the boundary and evanescent field in ϵ_0. The dispersion relation of an SPP propagating on the interface of the dielectric ϵ_0 and a metal can thus be satisfied in the region between the two light lines ck_{prism} and ck_0 . There are two well-known geometries of coupler suggested for the implementation of this idea. The first, suggested by Kretschmann and Raether [Kretschmann68] utilizes a thin metallic film on the back of a prism (see Fig. (1.1b)). In this configuration, the evanescent wave from the internal reflection in the prism is used to excite the SPP on the other side of the film (The evanescent wave momentum is still smaller than the momentum of the plasmon propagating on the prism end of the film.). This imposes the limitation on the film thickness, as the it needs to be thinner than the penetration depth in the metal to allow the evanescent wave to overlap with the plasmon mode on the other side. To use this technique in thicker

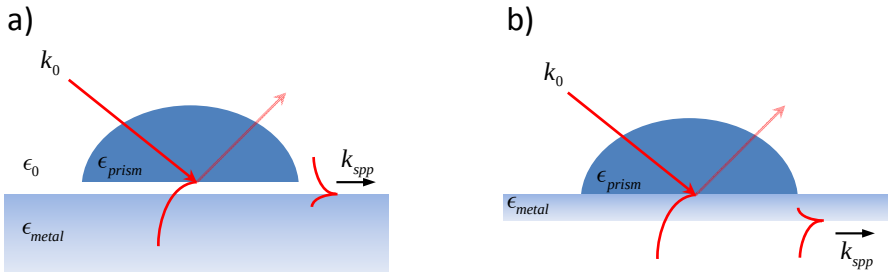

Figure 1.1: Otto (*a*) and Kretschmann and Reather (*b*) configurations for attenuated total reflection coupling to surface plasmons. A prism of dielectric constant ϵ_{prism} is placed slightly above (*a*) or in contact to (*b*) a metallic film of dielectric ϵ_{metal}. The total internal reflection generates an evanescent wave out side the prism

films, the closer side needs to be excited. This is done by introducing a thin layer of either air or a low dielectric constant material between the prism and the metal as is demonstrated in Fig. (1.1a), suggested by Otto [Otto68]. In this configuration gap is the critical parameter, as small gaps will lead to broadening of the plasmon resonance as a result of radiation damping, and too larger gap will lead to small overlap of the evanescent waves of the prism and the surface plasmon.

In both configurations, the coupling to the surface plasmon can be seen examining the reflected wave coming out of the prism. When the resonance conditions are satisfied, a dip appears in the reflection curves from the prism, as the energy is being transferred to the SPP. For exactly tailored parameters (thickness of the film for the Kretschmann configuration, gap width for the Otto configuration) the coupling can theoretically reach 100% efficiency ([Polzik92]), however both configurations are sensitive to the the mention parameters, and are thus not practical for use in nano-optical systems, though theoretical suggestions for these coupler on the nanoscale were put forward, including a their quantum mechanical description [Ballester09].

Grating

Another way to provide momentum conservation in order to excite SPPs is to use diffraction effects. Light diffracted off surface features can contain components whose wavevector coincides with that of the SPP. If light of wave number $k = \omega/c$ hits a sinusoidal grating with a period of a at an angle θ_0 its component in plane can have wave vectors

$$k_x = \frac{\omega}{c} \sin\theta_0 \pm \nu g \tag{1.46}$$

with ν an integer, and $g = 2\pi/a$ the lattice momentum. The momentum mismatch can thus be bridged by choosing

$$k_{spp} = k_{0,x} + \Delta k_x = k_{x,0} + \nu g \tag{1.47}$$

This allows choosing the angle at which coupling occurs. For example, if the grating periodicity matches that of the SPP, the light coupling will occur at normal angle to the surface.

The coupling is experimentally observed by a minimum as a dip in the reflection curve as a function of the angle of the incoming/outgoing light. The dependence on the grating height has been investigated in several regimes. For a shallow grating the dispersion of the plasmon propagating on the surface is unaltered by the corrugations. The efficiency of coupling is increased with increasing depth of the lattice, which is then only changing the scattering strength. As the height is further increased the plasmon mode change to match the new boundary condition. This then results in a mismatch of the grating momentum and the plasmon momentum reducing the coupling efficiency. This means the grating periodicity and depth must be We shall discuss this in detail in chapter (3) where we use a coupling grating as a part of the plasmonic lens we suggest.

1.6 Quantum nature of a system

In the previous sections, we have touched upon a point of greater importance to the understanding and control of quantum systems. The conceptual differences between classical and quantum physics have intrigued and sometimes bewildered the physics community since the early days of quantum mechanics. This has led to a search for indisputable manifestations of the quantum world through observations of non-classical behavior in experiments. A field of particular curiosity is that of identifying the quantum to classical cross-over for ever larger systems, thereby eventually identifying non-classical effects in macroscopic systems. Recently this has led to the observation of, e.g., macroscopic entangled atomic ensembles [Hammerer10, Kimble08], interference of large molecules [Arndt99] and experiments pushing toward observing non-classical effects in mechanical oscillators [Regal08, Teufel11, Chan11]. In parallel to this fundamental interest, non-classicality is of central importance to quantum information processing, the essence of which is to advance computation beyond what is classically possible [Nielsen04]. However, as with some of the examples given in Sec. (1.4.1), in some instances quantum effects are claimed by demonstrating consistency with an appropriate quantum model. Yet any rigorous demonstration of genuine quantum behavior must exclude the possibility of classical explanations. The importance of this is exemplified in Ref. [Grønbech-Jensen10], where a pair of coupled classical oscillators is shown to exhibit signatures easily mistaken for those of entanglement expected from a quantum model. Thus, a definite conclusion on the quantum nature of a system can only result from the breakdown of the classical description and not from verified agreement with quantum mechanics. This approach is most rigorously demonstrated by the

Bell-inequalities, where the underlying model of the system is stripped of any physics and is reduced to the very basic assumptions of locality and realism, resulting in an indisputable non-classicality criterion. The Bell-inequalities cannot however, by their very nature, be investigated by data obtained from a single system.

1.6.1 Nonclassicallity criteria and demonstrations

A large class of such non-classicality demonstrations relies on showing measurable effects which, according to quantum mechanics, cannot be obtained for a system being prepared classically. For instance, any light field being prepared by a classical source, must have its Glauber-Sudrashan P-function, a representation of the density matrix,

$$\hat{\rho} = \int d^2\alpha \, P(\alpha)|\alpha\rangle\langle\alpha|, \tag{1.48}$$

represent a probability distribution and is therefore positive and well behaved in the sense of a classical probability distribution [Sudarshan63]. As a classical state is understood to be described in quantum mechanics by a mixture of coherent states, the arbitrary state described by distribution of coherent state appearing in (1.48) is classical only if $P(\alpha)$ is a non-negative probability function. It is an argument that can be used to say that any state with an ill-behaved P-function is considered non-classical [Vogel00]. Yet, the direct probability of the P-function is not possible, and for nonclassical states, it is not only negative but highly singular, clearly not being determined by measurements. To work around this problem and prescribe a measurable criterion, Vogel [Vogel00] suggested examining the the characteristic function $G(k(\phi))$ of any quadrature probability distribution $x(\phi) = \hat{a}e^{i\phi} + \hat{a}^\dagger e^{-i\phi}$ defined as

$$p(x(\phi)) = \frac{1}{2\pi}\int dk \, e^{-ikx} G(k). \tag{1.49}$$

The advantage of using the characteristic function is that the vacuum noise contained in $p(x)$ can be convoluted out simply by dividing

$$G(k) = \tilde{G}(k)\, e^{-ik^2/2}, \tag{1.50}$$

and the resulting new characteristic function supplys the desired link between the quadrature and the P-function of the state

$$\tilde{p}(x) = \frac{1}{2\pi}\int dk \, e^{-ikx} G(k) = \int d^2\alpha \, P(\alpha)\delta(x - x_\alpha(\phi)) \tag{1.51}$$

with $x_\alpha(\phi) = \alpha e^{i\phi} + \alpha^* e^{-i\phi}$. That is, removing the ground state fluctuations the P-function is identified by Vogel as the classical distribution.

As it results from the regularity of the P-function, the new noise-reduced distribution should also be a proper distribution function. This is then translated, using Bochner's theorem [Bochner33] to the demand that $\tilde{G}$ be positive definite. Violation of this condition is equivalent to

$$\left|\tilde{G}(k)\right| > 1 \tag{1.52}$$

which, using (1.50), gives the final criterion

$$|G(k)| > e^{-ik^2/2}. \tag{1.53}$$

Though the derivation of this criterion is rather mathematical, the final result can be rather intuitively understood. If the characteristic function G shows features decaying slower than those of the coherent state, the distribution itself will exhibit structures narrower than that of the coherent state, render non classical by the quantum description. A squeezed state, for example, is considered non-classical because the quantum fluctuations of a coordinate are reduced below the vacuum fluctuations [Kiesel11], which according to quantum physics are inherently present even for a classical source. While such non-classicality arguments are perfectly adequate for, e.g., verifying the non-classicality of a source [Neergaard-Nielsen07] or validating the performance of a quantum information protocol [Mišta10, Furusawa98, Lee11b], they inherently rely on quantum mechanics.

1.6.2 The second order coherence

An example for a criterion making no assumption based on quantum mechanics, is that of the second order coherence function. The second order coherence function is the normalized intensity intensity fluctuations, two time correlation function. It is defined as

$$g^{(2)}(\tau) \equiv \frac{\langle \bar{I}(t)\bar{I}(t+\tau)\rangle}{\langle \bar{I}(t)\rangle^2} = \frac{\langle E^*(t)E^*(t+\tau)E(t+\tau)E(t)\rangle}{\langle E^*(t)E(t)\rangle^2}. \tag{1.54}$$

where $\bar{I}(t)$ is the intensity averaged over several cycles, and stationary statistical ensemble is assumed. The last term is the expression for light measurements, in terms of the electric fields. The possible range of values for such a measurement can by calculated by considering the Cauchy inequality for the two real valued intensities

$$2\bar{I}(t_1)\bar{I}(t_2) \leq \bar{I}^2(t_1) + \bar{I}^2(t_2), \tag{1.55}$$

which on a set of measurements, means the averages obey

$$\langle \bar{I}(0)\rangle^2 \leq \langle \bar{I}^2(0)\rangle. \tag{1.56}$$

This leads to the zero time delay correlation being constrained to

$$g^{(2)}(0) \geq 1. \tag{1.57}$$

Though no such constraint exist for the general time delay $\tau \neq 0$, one can still show that

$$g^{(2)}(\tau) \geq g^{(2)}(0). \tag{1.58}$$

These two characteristics of the intensity fluctuations are based solely on the existence of an underlying distribution function leading to Eq. (1.56).

In the quantum mechanical description, however, the intensity is described in term of the fields (for light) operators

$$E \to \hat{E}^+ + \hat{E}^- = \sqrt{\frac{\hbar\omega}{2\epsilon_0 V}}\left(\hat{a}^\dagger e^{i\phi} + \hat{a}e^{-i\phi}\right) \tag{1.59}$$

or in the general case, by the generalized coordinate $x \to \left(\hat{a}^\dagger e^{i\phi} + \hat{a} e^{-i\phi}\right)$, $a\,(a^\dagger)$ being the annihilation (creation) operator for the bosonic field of energy excitation in the system. The second order coherence function then becomes

$$g^{(2)}(\tau) = \frac{\langle a^\dagger a^\dagger a a \rangle}{\langle a^\dagger a \rangle^2}. \tag{1.60}$$

For simplicity, we limit our discussion here to the single mode field which explains the lack of dependance on both position and time. This can be expressed using the mean number of excitons in the system

$$g^{(2)}(\tau) = \frac{\langle n(n-1) \rangle}{\langle n \rangle^2} = 1 - \frac{1}{\langle n \rangle} + \frac{(\Delta n)^2}{\langle n \rangle^2} \geq 1 - \frac{1}{\langle n \rangle}, \tag{1.61}$$

where we have used that the variance in exciton number, $(\Delta n)^2 \equiv \langle n^2 \rangle - \langle n \rangle^2$ is a non negative value. The range of coherence accessible according to the quantum description is thus different than the one permitted by the classical description. This is not merely a theoretical bound, as one can immediately verify by examining the coherence of a Fock state, for which $\Delta n = 0$. The coherence of the Fock state $|n\rangle$ is therefore

$$g^{(2)}(\tau) = 1 - \frac{1}{n}, \tag{1.62}$$

which cannot be explained by the classical argumentation. In measuring $g^{(2)} < 1$, one therefore shows the system to be inexplicable by a classical model, and not the disagreement of the results with the quantum mechanical description of the classical state.

1.6.3 continuous variables and phase-space distributions

The nonclassicality criterion presented in the previous section requires the ability to measure the intensity. In chapter (4), we shall present such a nonclassicality criterion which is based on the indirect inferring of the phase space distribution of the state. We shall therfore review the concept of a phase space distribution.

In classical physics, the state of a system is completely determined by its generalized coordinates, x and p, for each degree of freedom. Even in the case where only statistical knowledge of the position and momentum can be obtained. The state of such a system is fully characterized by the phase space distribution $W(x, p)$; that is, given the phase space distribution, the ensemble averaged result of any measurable quantity A can be obtained by

$$\langle A \rangle = \int dx dp\, W(x, p)\, A(x, p)\,, \tag{1.63}$$

where $A(x, p)$ is the decomposition of the quantity A in terms of the generalized coordinate x and its canonically conjugated momentum p. Classically, the phase space distribution $W(x_i, p_i)$ is the joint probability of finding the system in an infinitesimal phase space volume around $x = x_i, p = p_i$ and hence it obeys all the requirements of a probability distribution, including being a non-negative function. In the case of a

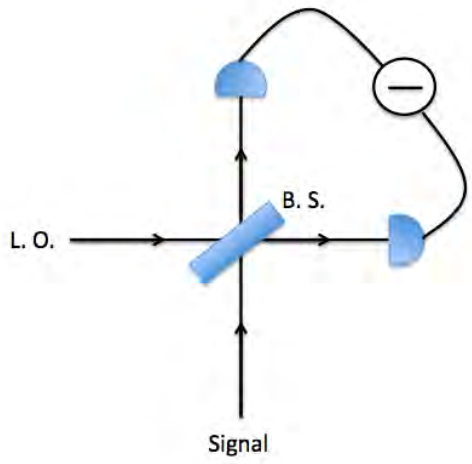

Figure 1.2: Homodyne detection scheme. The signal is mixed on a 50 : 50 beam splitter with a strong coherent light source and the resulting intensity in two arms is then measured and subtracted to give measurements of the quadratures of the signal light. See text for details.

quantum phase space function, the Heisenberg uncertainty renders this definition meaningless, as a joint probability distribution for x and p does not exist.

The phase space distribution is only defined through Eq. (1.63) [Nha08] and this relaxation of constraints allows for negative values of the function in areas smaller than $\hbar$. This negativity is not observable directly due to the vacuum fluctuations preventing simultaneous measurement of x and p. However, using classical arguments one can still infer the phase space distribution from measurements of only a single observable at a time (see below) and detect such negativities, thereby illuminating the failure of classical theory.

the statistics of the position and momentum in classical physics can be completely characterized by a phase space distribution $W(p, q)$. The distribution quantifies the probability of finding a pair of x and p

However, the existence of an equivalent quantum mechanical phase space formulation, as introduced by Wigner [Wigner32], offers a valuable tool for investigating the discrepancies between classical and quantum mechanical expectations, such as the one studied here.

Probing the phase space distribution - homodyne detection

It is left, therefore, to describe the way these phase space (quasi-) probabilities can be sampled. In this section we review the main technique to measure the quadratures of the light field, called homodyne detection. The scheme of the balanced homodyne detector is depicted in Fig. (1.2). The signal light is interfered with a coherent laser beam whose intensity much stronger than that of the signal. Furthermore, the intensity is assumed large enough to be treated classically . That is, the quantum fluctuations of the local oscillator can be ignored. After the optical mixing of the signal and the local oscillator on the 50 : 50 beam splitter, each

emerging beam is measured by a photodetector. The photocurrents are then subtracted from each other. An important feature is that the photodetection need only be proportional to the photon number of the beams (a linear response photodiode, for example) but not necessarily photon number resolving. This allows for higher detection efficiencies. assuming the photocurrents to be proportional to the photon number impinging beams $\hat{n}_1$, $\hat{n}_2$ the final quantity of interest is

$$I_c - I_d = \hat{c}^\dagger \hat{c} - \hat{d}^\dagger \hat{d} \tag{1.64}$$

Writing these operators in terms of the original signal annihilation operator $\hat{a}$ and the the complex amplitude of the strong LO coherent field α_{LO},

$$\hat{c} = \frac{1}{\sqrt{2}} \left(\hat{a} - \alpha_{LO} \right), \quad \hat{d} = \frac{1}{\sqrt{2}} \left(\hat{a} + \alpha_{LO} \right), \tag{1.65}$$

leads to the difference being

$$I_c - I_d = \sqrt{2} |\alpha_{LO}| q_\theta \tag{1.66}$$

with the angel θ, which determines the quadrature, being the LO phase. Thus,the different field quadratures can be probed by varying the phase of the laser.

A note should also be made on errors and inefficiencies in the balanced homodyne scheme. As the signal is amplified by the imposed high intensity laser, such that high efficiency yet noisy photodetectors can be used. In [Polzik92] the detectors efficiencies were cited to be $\eta = 1 \pm 0.02$. Even for a finite efficiency of the detectors and imperfect mode matching of the beams, losses in the two arms of the homodyne do not change the operation of the detector and can be mapped to a beam splitter loss on the entrance port of the homodyne detector.

1.7 Thesis structure

The thesis is structured in the following manner; In part I we suggest devices for efficient coupling of surface plasmons and photons. This include two different schemes. In chapter) we discuss adiabatic coupling of a dielectric slab waveguide with a plasmonic slab guide, allowing for an effective transfer of energy from one waveguide to the other. This is done by choosing the geometry of the wave guides such that their dispersion curves cross a some point along the guides. the variation of propagation constant with the distance is achieved by tapering the plasmonic slab, where the tapering is made slow enough to ensure negligible backscattering. To describe the propagation of energy along the wire, we develop a perturbation method based on casting the Maxwell equations into a Schödinger like form. The method developed is applicable to any cross section of the guide, allowing future use in more realistic experimental setups.

In chapter (2) we go on to suggest a different method of using surface plasmons as a mediator between light and a quantum emitter. We examine an emitter placed above a structured metallic surface. The structure

consists of concentric grooves, optimized to generate a coupling grating between light propagating perpendicular to the sample and radially propagating surface plasmons. These groove also generate a lossy cavity effect, as a fraction of the out-going plasmons are reflect back towards the emitter. This results in significant increase of the emitter's decay rate. In addition, solid state quantum dots in layered semiconductor structures have their dipole moment aligned parallel to the plane of the lens, reducing the coupling efficiency to surface plasmon. To overcome this, we add a central groove to the metallic structure and show this results in improved coupling and higher decay rates.

The second part of the thesis deals with nonclassicality of a quantum state, and in chapter (4) we suggest a criterion for showing the breakdown of classical theory for a local state, when limited to quadrature measurements only. We take the approach suggested above, where no assumptions based on quantum mechanics are made. Instead, we use the quadrature measurements to classically infer the underlying distribution function. The non negativity constraint on the distribution function results in an inequality on moments of the distribution function. However, non classical states violate this inequality, showing the resulting distribution function to contain negativity. By that we show that no classical model can be devised which will reproduce the quadrature measurements of that state. We test this criterion on a set of quadrature measurements of a noisy single photon source, demonstrating the negativity, and the essential nonclassicality of the single photon state.

Part I

Efficient coupling of light and surface plasmons for quantum optics applications

Chapter 2

Adiabatic coupling of plasmonic and photonic waveguides

2.1 Introduction

In the introduction we presented the possibility of reaching strong coupling to a single emitter near a metallic surface [Chang06, Chang07a, Akimov07] for the use in quantum optics and quantum information applications [Chang07b]. This regime is reached when the surface supports modes with high spatial confinement. However, as discussed, these highly confined modes are short-range plasmon modes which are rapidly damped in the metal. This makes a reliable in and out coupling to the plasmon modes very important. Current experiments mostly use end-coupling to the plasmonic waveguide (see, e.g. [Huck09]). However, this is lossy and restricted to the long-range surface plasmon modes. Another option suggested by Chang *et al.* in [Chang07a] is that of generating a resonant cross talk between the plasmonic nanowire and an adjacent dielectric waveguide. In doing so the excitation experiences Rabi flipping between the wire and the waveguide, due to the evanescent fields overlaps of both the guides. The authors then showed that terminating the interaction at the point were the excitation is completely in the photonic waveguide, by either the termination of one of the guides or by increasing the separation, will lead to efficient extraction of the plasmonic excitation. The technical details of the termination were not treated. Recently, adiabatic changes of a plasmon mode by tapering of the waveguide have also been investigated theoretically [Stockman04] and experimentally [Verhagen09].

In this chapter we investigate the possibility of performing an adiabatic transfer between a plasmon mode and another guided mode of a dielectric waveguide. Different varieties of these adiabatic transfer techniques are well established in atomic physics (see, e.g., [Bergmann98]) and some of them have also been demonstrated for dielectric waveguides [Longhi07]. Here we suggest here a general formalism under which such general coupling structures can be investigated. We utilize the understanding of the process of adiabatic passage reached in quantum mechanics over the years since the work of Born and Fock in 1928 [Born28]. The advantage of the method presented here is its straight forward gen-

eralization to arbitrary cross section of the samples, allowing for easier numerical modeling and optimization of experimental setups.

The chapter is structured as follows. In Sec. (2.2) we review the main example used in this work, that of the slab waveguide and slab plasmonic channel. InSec. (2.3) we introduce the formalism used here. We cast the Maxwell equations in a quantum-mechanical-like form and discuss the requirements for applying the techniques of adiabatic passage. In Sec. (2.5) we present the results for the adiabatic transfer of plasmonic excitation from the metallic nanoslab to an adjacent dielectric waveguide, and discuss adiabatic condition for such tapering to insure the efficient transfer of the energy. Finally we summarize and conclude the results in Sec. (2.6).

2.2 Slab waveguide and plasmonic waveguide

Though the method used here is general and applicable to three dimensional configurations, we shall limit ourselves to discussing a two dimensional systems, namely a slab waveguide and a slab plasmonic waveguide. For this reason it will be useful to review here the dispersion relation and modes of these wave guides. The planar slab waveguide is shown in Fig. (2.1). It consists of a core layer of thickness $2a$ infinitely long in the $\hat{y}$ direction, surrounded by a uniform medium, with the waves guided along the $\hat{z}$ direction. The core layer is characterized by a dielectric constant ϵ_2 which can be either positive (for the photonic waveguide) or negative (for the plasominc waveguide). We shall work in the frequency domain for a fixed wavelength and will neglect the dispersion of the metal. For the plasmonic waveguide, only TM mode can occur [Zayats03], and thus we need consider only three components of the fields, namely H_y, E_x and E_z. Though the dielectric guide support transverse electric (TE) modes, these will not interact with the plasmonic modes, and we therefore consider only the TM modes of the dielectric waveguide as well.

Next we calculate the dispersion curves for the two waveguides. As we are looking for a solution decaying exponentially from the metal-dielectric interface into the dielectric, the following solution can be assumed

$$E^{(I)}, H^{(I)} \propto e^{-\kappa_1(x-a)}e^{iqz}$$
$$E^{(III)}, H^{(III)} \propto e^{\kappa_1(x+a)}e^{iqz}$$

$$\left.\begin{array}{l} E_+^{(II)}, H^{(II)} \propto e^{\kappa_2(x-a)}e^{iqz} \\ E_+^{(II)}, H^{(II)} \propto e^{-\kappa_2(x+a)}e^{iqz} \end{array}\right\} \textit{for the plasmonic waveguide}$$

$$\left.\begin{array}{l} E_+^{(II)}, H^{(II)} \propto e^{ik_2(x-a)}e^{iqz} \\ E_+^{(II)}, H^{(II)} \propto e^{-ik_2(x+a)}e^{iqz} \end{array}\right\} \textit{for the dielectric waveguide}$$

where the superscripts refer to the different regions of the guide section plotted in Fig. (2.1a), and $\kappa_{1,2}$ and k_2 are to be determined later as a

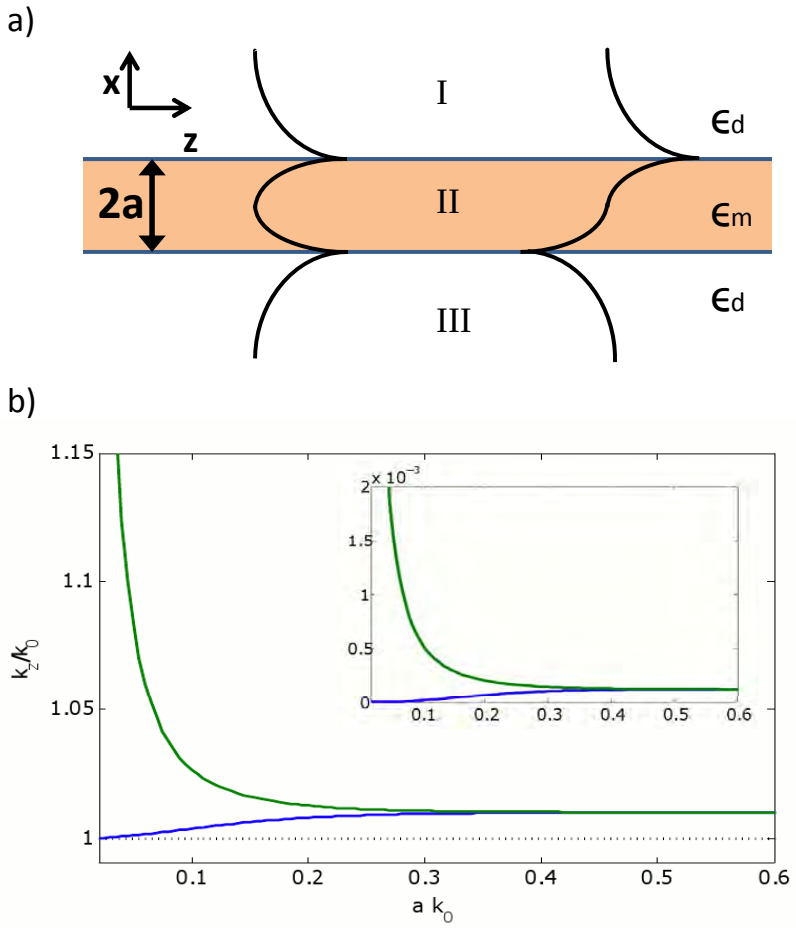

Figure 2.1: In *a*) a section of the slab plasmon waveguides considered in sec. 2.2. The structure is assumed infinite in the y-direction. In black, the long (left) and short range (right) modes, depicted by H_y the amplitude of the magnetic field in the y direction, see text for details. In *b*) the dispersion curve for the two modes is plotted. In the inset the imaginary part of the wave number is shown, corresponding to the decay of the two modes

function of the wave number q.

The complete mode is obtained by equating the boundary conditions and the amplitudes in each region. The parallel electric field E_z and magnetic field H_y are continuous across the interface, as well as the electric displacement $D_x = \epsilon E_x$ perpendicular to the surface. These equations give the relation between $\kappa_{1,2}$ (k_2), the decay (propagation) constant in the transverse direction, and the wave number q, namely

$$\kappa_i^2 = q^2 - k_0^2 \epsilon_i, \tag{2.1}$$

for the plasmonic guide and

$$-k_2^2 = q^2 - k_0^2 \epsilon_2, \tag{2.2}$$

for the region *II* in the dielectric waveguide case.

The resulting dispersion relation for the plasmon is

$$e^{2\kappa_2 a}(\frac{\kappa_2}{\epsilon_2}+\frac{\kappa_1}{\epsilon_1})^2 = e^{-2\kappa_2 a}\left(\frac{\kappa_2}{\epsilon_2}-\frac{\kappa_1}{\epsilon_1}\right)^2, \tag{2.3}$$

which according to the root sign chosen yields one of the two plasmonic modes,

$$\frac{\kappa_2}{\epsilon_2}\tanh(\kappa_2 a) = -\frac{\kappa_1}{\epsilon_1} \tag{2.4}$$

$$\frac{\kappa_2}{\epsilon_2}\coth(\kappa_2 a) = -\frac{\kappa_1}{\epsilon_1} \tag{2.5}$$

plotted in Fig. (2.1b). The corresponding magnetic field amplitudes are

$$H_{lr} = \frac{1}{2}\begin{pmatrix} 1 \\ 1-\frac{\kappa_2\epsilon_1}{\kappa_1\epsilon_2} \\ 1-\frac{\kappa_2\epsilon_1}{\kappa_1\epsilon_2} \\ 1 \end{pmatrix} \qquad H_{sr} = \frac{1}{2}\begin{pmatrix} 1 \\ 1-\frac{\kappa_2\epsilon_1}{\kappa_1\epsilon_2} \\ -1+\frac{\kappa_2\epsilon_1}{\kappa_1\epsilon_2} \\ -1 \end{pmatrix} \tag{2.6}$$

where the symmetric, first mode is the long range plasmon, and the second the short range one. These names can be justified examining the dispersion curves of both modes plotted in Fig. (2.1). For the long range mode, both real and imaginary parts of the wave number approach that of the bulk photons. This means lower losses, but also less confinement of the fields around the metal making it less useful for strong coupling to single emitters. The short range plasmon however exhibits the divergence of the wavenumber as the width of the slab is reduced. As we discussed in the introduction this implies tight confinement of the fields and make the short range plasmon couple strongly to quantum emitters when the width is reduced, similar to the the plasmonic mode on a cylindrical nanowire.

For the dielectric waveguide the dispersion relation of the TM modes in the slab is

$$\epsilon_2\kappa_{\perp,1} = \epsilon_1 k_2 \tan(k_2 a) \qquad \textit{even modes} \tag{2.7}$$

$$\epsilon_2\kappa_{\perp,1} = -\epsilon_1 k_2 \cot(k_2 a) \qquad \textit{odd modes} \tag{2.8}$$

The resulting k-numbers for the TM_0 mode in the slab are plotted in Fig. (2.2). Examining Eqs. (2.7) and (2.8) the different modes have a cutoff when the mode is no longer bound on the cross-section. for the mode j this happens when $\kappa_2 a = j\pi/2$. At this point the $\kappa_{\perp,1} = 0$, which means $q = k_0$ and no guiding. We will focus here on the the single mode regime of the wire, where $\kappa_2 a < \pi/2$. in this regime the only guided mode is the TM_0 mode which does not exhibit a cutoff, but its wave vector approaches the surrounding medium as the radius is decreased. This behavior is opposite to the one discussed above for the plasmonic wire. As the waveguide is narrower the extension of the electric field outside the wire increases.

In Fig. (2.2), the dispersion curves of the wire and the wave guide are plotted for the different half-width in isolation. The different trends of

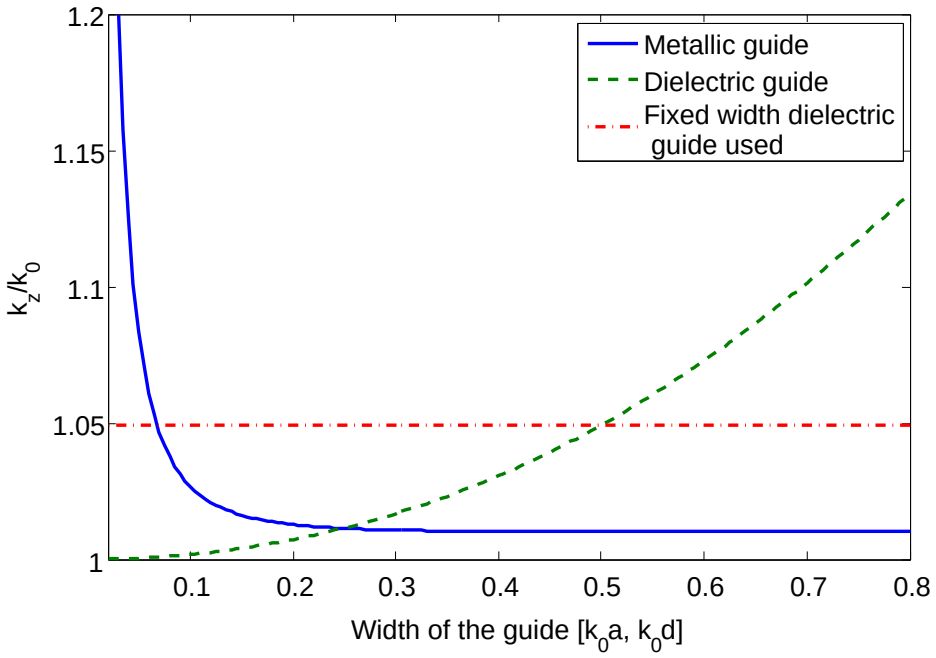

Figure 2.2: Effective refractive index for a dielectric waveguide of dielectric constant $\epsilon = 2.5$ (dashed, green) and a silver plasmonic waveguide (full line, blue) as a function of the waveguides widths. Dash-dot line indicates the dielectric waveguide chosen in the calculation of the adiabatic coupler in Sec. (2.5).

the dispersion curves, corresponding to the confinement of the fields in the plasmonic slab versus the extension of the dielectric waveguide as the half width is reduced, generate a crossing of the propagation constants for appropriately chosen widths of the two guides. It is this crossing we exploit in this chapter. Placing the two guides next to each other, the overlap of the guides with the evanescent fields of the other guide, will generate interaction. The new modes of the hybridized system will display an avoided crossing - meaning their dispersion curves will display a gap rather than cross, corresponding to a "flip" between the plasmonic and the dielectric waveguide isolated modes. In what follows we explore the conditions of slow variation in this coupled guides configuration under which an excitation of the plasmonic guide will adiabatically follow the hybridized mode, leading an energy transfer into the dielectric waveguide.

2.3 Mapping the EM Maxwell equations on the Schrödinger equations

To consider the propagation of an excitation along a slowly varying waveguide we use techniques of adiabatic evolution and perturbation theory in their quantum mechanical formulation. Quantum-classical analogies are very useful for increasing the understanding of both fields, and have

been already used in a number of seemingly unrelated fields, from Anderson localization[Schwartz07] to quantum chaos[Agam92] and Bloch oscillations[Morandotti99, Pertsch99]. Commonly, the optical analogs are used to investigate these effectively quantum effects. In this work, we shall make the opposite route. We will introduce a quantum description of the classical Maxwell equation in order to use the formalism of adiabatic changes.

The concept of perturbation is very well understood both in classical and quantum mechanics. The aim of the theory presented here is to project the problem at hand in terms of a z-dependent Schrödinger like equation of motion, defining an inner product and applying such a perturbative scheme.

The projection of the Maxwell equations into the form of a scalar Scödinger equation is usually done within the weak guidance limit. Using the scalar wave equation for any of the field components, say E_z,

$$\nabla^2 E_z + k^2 \epsilon E_z = 0 \tag{2.9}$$

Within of the paraxial approximation [Born99] this can be written as

$$E_z = \psi(x,z) e^{i\sqrt{\epsilon_2} kz}, \tag{2.10}$$

with ψ being a slowly varying function, ϵ_1 is the cladding dielectric constant and ϵ_2 is the core dielectric constant. In combination with the assumption that $(\sqrt{\epsilon_2} + \sqrt{\epsilon_1})/2\sqrt{\epsilon_2} \sim 1$ allows to neglect the second derivative in the propagation direction, resulting in the propagation equation

$$\frac{\partial^2}{\partial x^2}\psi + 2i\sqrt{\epsilon_2} k \frac{\partial}{\partial z}\psi - 2\sqrt{\epsilon_2} k^2 \left(\bar{u}(x) + \Delta_n\right)\psi = 0, \tag{2.11}$$

here $\bar{u}$ is a square potential well on the boundaries of the waveguide, of height $\sqrt{\epsilon_2} - \sqrt{\epsilon_1}$ and Δ_n are a perturbation in the index of refraction, assumed much smaller than the core index of refraction.

As we wish to consider surface plasmons, however, the assumption of weak guidance is not suitable for our needs. the dielectric constants of the metal and the surroundings vary significantly from each other, both in the sign and absolute magnitude. For this reason, the mapping will be of the vectorial Maxwell equations, and we shall make no assumptions on dielectric constants ratios.

2.3.1 Perturbation and Mode orthogonality

For a given frequency ω the propagation is governed by Maxwell's equations

$$\nabla \cdot D = 0, \qquad \nabla \times \mathbf{H} = -i\frac{\omega}{c}\mathbf{D} \tag{2.12}$$

$$\nabla \cdot B = 0, \qquad \nabla \times \mathbf{E} = +i\frac{\omega}{c}\mathbf{B}. \tag{2.13}$$

We assume that the waveguide is described by a permittivity $\epsilon(x,z)$, which is a function of x and z, while the relative magnetic permeability is one. Thus the material equations are given by

$$\mathbf{D} = \epsilon(x,z)\mathbf{E}, \qquad \mathbf{B} = \mu\mathbf{H}. \tag{2.14}$$

As a guiding example throughout we use the systems considered in Sec. (2.2) with a guided mode which is guided by a thin film with infinite extension in the y-direction and travels into the z-direction. This reduces the problem to a two dimensional problem, with a one dimensional cross section, making the equations easier to follow. However the formalism provided here is general.

Assuming an infinite extension into the y-direction, we have $\partial_y = 0$. Furthermore one can show that plasmon modes on the thin films are TM modes such that $E_y = H_x = H_z = 0$ (see, e.g., [Pitarke07]). Maxwell's equations for the field $\mathbf{E}$ and $\mathbf{H}$ thus reduce to the four equations

$$\frac{\partial H_y}{\partial z} = i\frac{\omega}{c}\epsilon E_x \tag{2.15}$$

$$E_z = \frac{ic}{\omega\epsilon}\frac{\partial H_y}{\partial x} \tag{2.16}$$

$$\frac{\partial E_x}{\partial z} = \frac{\partial E_z}{\partial x} + i\frac{\omega}{c}\mu H_y \tag{2.17}$$

$$\frac{\partial E_z}{\partial z} = -\frac{\partial E_x}{\partial x} - \frac{1}{\epsilon}\frac{\partial \epsilon}{\partial x}E_x - \frac{1}{\epsilon}\frac{\partial \epsilon}{\partial z}E_z. \tag{2.18}$$

From Eqn. (2.16) we see that we only have to take into account two independent variables E_x and H_y. However, it is more convenient to keep all three components E_x, E_z and H_y. Nevertheless we note that Eqn. (2.16) is redundant - if we take the derivative with respect to z we reproduce Eqn. (2.18).

We now introduce the field vector

$$\psi = \begin{pmatrix} E_x \\ E_z \\ H_y \end{pmatrix}. \tag{2.19}$$

We can recast the propagation equations Eqns. (2.15), (2.17) and (2.18) into the form

$$i\frac{\partial \psi}{\partial z} = (M_0 + M_1)\,\psi. \tag{2.20}$$

Here, the dynamics is governed by the operators

$$M_0 = \begin{pmatrix} 0 & i\partial_x & -\omega/c \\ -i\partial_x - i(\partial_x\epsilon)/\epsilon & 0 & 0 \\ -\omega\epsilon/c & 0 & 0 \end{pmatrix} \tag{2.21}$$

$$M_1 = \begin{pmatrix} 0 & 0 & 0 \\ 0 & -i(\partial_z\epsilon)/\epsilon & 0 \\ 0 & 0 & 0 \end{pmatrix}. \tag{2.22}$$

Note that Eq. (2.20) has the form similar to the Schrödinger with M_0 as the unperturbed Hamiltonian H_0 and M_1 being the the small perturbation V. Furthermore, if $\partial_z\epsilon = 0$, the propagation equation can be solved by diagonalizing M_0 using the waveguide modes, equivalent to the quantum mechanical stationary modes. In the following we will start from M_0 and view M_1 as a small perturbation. We then expand the solution using the stationary modes of the translationally invariant waveguide, and examine the conditions under which the slowly varying wire mode will follow the local stationary modes (adiabatic following).

2.3.2 definition of the inner product for the guided modes

In order to apply the well understood techniques of quantum mechanics, a key feature of the system should be the Hermiticity of the Hamiltonian. This ensures real eigenvalues, and a complete orthonormal set of eigenfunctions. Unfortunately, M_0 is not hermitian with respect to the standard scalar product

$$\langle \psi | \phi \rangle = \int dx \sum_j \psi_j(x)^* \phi_j(x). \tag{2.23}$$

However, the operator M_0 is pseudo-hermitian as it satisfies the relation

$$\eta \, M_0^\dagger \, \eta^{-1} = M_0, \tag{2.24}$$

where the dagger symbol (†) denotes the common hermitian conjugate and η is a dielectric parity matrix defined by

$$\eta = \mathrm{diag}(\epsilon, -\epsilon, 1). \tag{2.25}$$

A pseudo-hermitian operator has some nice properties which makes it just as useful as a hermitian one. First of all, all eigenvalues are either real or come in complex conjugated pairs [Bender98], corresponding to propagating and damped electromagnetic modes, respectively. Second, the eigenmodes form a complete orthonormal set [Weigert03]. Another significant general feature is that with M_0 independent of z, the z-evolution conserves an inner product given by [Mostafazadeh02]

$$\langle\langle \psi | \phi \rangle\rangle = \langle \psi | \eta \phi \rangle \tag{2.26}$$

$$= \int dx \sum_{jk} \psi_j(x)^* \eta_{jk} \phi_k(x). \tag{2.27}$$

However this is not the case here, as the the metric η is z-dependent. The implication of this is considered in 2.3.4.

2.3.3 Relation to momentum density transfer of the guided mode

To understand the physical meaning of the inner product described here, we examine the expression in the dielectric. In the dielectric, this quantity is proportional to the (z, z) component of the Maxwell stress tensor,

$$T_{\alpha,\beta} = \frac{1}{4\pi} \left[E_\alpha D_\beta + H_\alpha B_\beta - \frac{1}{2} \left(\mathbf{E} \cdot \mathbf{D} + \mathbf{B} \cdot \mathbf{H} \right) \delta_{\alpha,\beta} \right] \tag{2.28}$$

representing the flow of combined material and field momenta through the wave guide cross section. It is interesting to note the natural emergence of the Minkowski form of the material stress tensor, though it has been disputed [Peierls76]. Here it arises because the M_0 Hamiltonian represents the translational invariant propagation (a wire with a constant cross section). This naturally leads to momentum conservation along the wire, and the momentum density can serve as an inner product. We emphasis that the ability to extend this symmetry into the metallic part

is due to neglecting the dispersion in the metal. The above form of the stress tensor is derived assuming linear medium. In considering real metals, a more careful treatment of the dependence of the temperature and pressure on the dielectric constant will be required.

2.3.4 Equation of motion for longitudinal changes

We now turn to treating longitudinal changes in the wire, using the Schödinger type equation (2.20). We first ignore the M_1 term and will include it later. We will formulate the problem as follows. We know the eigenmodes for each stationary Hamiltonian for the transitionally invariant problem ($\frac{\partial \epsilon}{\partial z} = 0$) of the form

$$-k_m(Z)\,\psi_m(Z) = M_0\left(\epsilon(\mathbf{r}_\perp; Z)\right)\psi_m(Z), \tag{2.29}$$

form a complete set of orthonormal eigenfunctions. We therefore write the solution in the following way

$$\Phi(z) = \sum_m C_m(z) \exp\left(i\int_{-\infty}^{z} k_m(\xi)d\xi\right)\psi_m. \tag{2.30}$$

Substituting into (2.20), multiplying by $\langle\langle\psi_n|$ on the left and integrating over the transverse coordinates, we get

$$\begin{aligned} &i\sum_m \frac{\partial C_m(z)}{\partial z}\exp\left(i\int_{-\infty}^{z} k_m(\xi)d\xi\right)\langle\langle\psi_n|\psi_m\rangle\rangle + \\ &+ i\sum_m C_m(z)\exp\left(i\int_{-\infty}^{z} k_m(\xi)d\xi\right)\langle\langle\psi_n|\frac{\partial}{\partial z}\psi_m\rangle\rangle = 0. \end{aligned} \tag{2.31}$$

The orthogonality of the eigenfunctions can be used for the first term. An expression for the second term is obtained by deriving equation (2.29) with respect to the parameter Z, and multiplying by $\langle\langle\psi_n|$ on the left, with $n \neq m$

$$\langle\langle\psi_n|\frac{\partial}{\partial z}|\psi_m\rangle\rangle = \frac{\langle\langle\psi_n|\frac{\partial M_0}{\partial z}|\psi_m\rangle\rangle}{k_n - k_m}. \tag{2.32}$$

The equation of motion for the coefficients $C_m(z)$ can thus be written

$$\begin{aligned} i\frac{\partial C_n(z)}{\partial z} &= \sum_{m\neq n} C_m(z)\exp\left(i\int_{-\infty}^{z}\left(k_n(\xi) - k_m(\xi)\right)d\xi\right)\times \\ &\times\left(-i\frac{\langle\langle\psi_n|\frac{\partial M_0}{\partial z}|\psi_m\rangle\rangle}{k_n - k_m}\right) + \langle\langle\psi_n|\frac{\partial}{\partial z}|\psi_n\rangle\rangle \end{aligned} \tag{2.33}$$

Phase evolution along z

For Eq.(2.33) to be a consistent description of the evolution of the wave along the z axis, the term $\langle\langle\psi_n|\frac{\partial}{\partial z}\psi_n\rangle\rangle$ with the same index n on both sides of the inner product must also be accounted for. In quantum mechanics, the normalization condition ensures the contribution from this term is purely imaginary. Fixing $\langle\langle\psi_n|\psi_n\rangle\rangle$ here, the differentiation of the the normalization condition yields

$$\frac{d}{dz}\langle\langle\psi_n|\psi_n\rangle\rangle = 2\Re\left\{\langle\langle\psi_n|\frac{\partial}{\partial z}\psi_n\rangle\rangle\right\} + \langle\psi_n|\frac{\partial\eta}{\partial z}|\psi_n\rangle \tag{2.34}$$

where the single $\langle\ \rangle$ bracket is to be understood in the common L^2 inner product used in quantum mechanics. This means the diagonal term will have a real part as well due to the change in the inner product discussed above. The term $-\frac{1}{2}\langle\psi_n|\frac{\partial\eta}{\partial z}|\psi_n\rangle$ should thus be added to the propagation equation to account for the change of amplitude of the mode along the propagation direction.

An additional contribution of the diagonal term is due to the imaginary part and causes phase changes. However this contribution can be set to zero using the freedom of choice of the phases of the eigenmodes in the different slices. As the functions at each slice are only determined up to a phase, we can add a phase $e^{i\alpha(z)}$ such that

$$\langle\langle\tilde{\psi}_n|\frac{\partial}{\partial z}\tilde{\psi}_n\rangle\rangle = \langle\langle e^{-i\alpha(z)}\psi_n|\frac{\partial}{\partial z}e^{i\alpha(z)}\psi_n\rangle\rangle = \Im\left\{\langle\langle\psi_n|\frac{\partial}{\partial z}\psi_n\rangle\rangle\right\} + i\frac{d\alpha}{dz}. \quad (2.35)$$

Therefore, if the relative phases are set such that

$$\alpha = -\int^z \Im\left\{\langle\langle\psi_n|\frac{\partial}{\partial z}\psi_n\rangle\rangle\right\} dz, \quad (2.36)$$

the phase contribution of the diagonal term vanishes. In the examples we discuss here, the relative phase between the slices was fixed directly, without an explicit calculation of the derivative. By fixing the transverse fields to be real, and have a continuous sign convention between the slices we set the phase evolution of the norm to zero ($\alpha = 0$).

Step boundary conditions

The equation of motion derived above uses the partial derivative of the Maxwell equation Hamiltonian, $\frac{\partial M_0}{\partial z}$, which, when applied to Eq.(2.21) yields

$$\partial_z M_0 = \begin{pmatrix} 0 & 0 & 0 \\ -i\frac{1}{\epsilon}\partial_z\partial_x\epsilon + i\frac{1}{\epsilon^2}(\partial_x\epsilon)(\partial_z\epsilon) & 0 & 0 \\ -k\partial_z\epsilon & 0 & 0 \end{pmatrix}. \quad (2.37)$$

$$(2.38)$$

We shall focus our attention on waveguides with a step profile in the x-direction (radial direction in the general three dimensional case) and a uniformly expanding cross section

$$\epsilon = \epsilon_2 + (\epsilon_1 - \epsilon_2)\,\Theta(z - f(x,y)). \quad (2.39)$$

and therefore both $\partial_x\epsilon, \partial_z\epsilon$ will be Dirac delta functions, and $\partial_x\partial_z\epsilon$ will be highly singular. This however can be overcome in the following way; Examine the expression $(\partial_z M_0)_{2,1} = -i\frac{1}{\epsilon}\partial_z\partial_x\epsilon + i\frac{1}{\epsilon^2}(\partial_x\epsilon)(\partial_z\epsilon)$. When appearing in the inner product between $\langle\langle k_n|$ and $|k_m\rangle\rangle$ the integral over the crosse section will read

$$\int \mathrm{d}\mathbf{r}_\perp\, E_z^*\epsilon\left[-i\frac{1}{\epsilon}\partial_z\partial_x\epsilon + i\frac{1}{\epsilon^2}(\partial_x\epsilon)(\partial_z\epsilon)\right] E_x \quad (2.40)$$

We first notice that

$$(\partial_x \partial_z \epsilon) E_x = \partial_x \left((\partial_z \epsilon) E_x \right) - (\partial_z \epsilon) \partial_x E_x \tag{2.41}$$

This can now be plugged back in to (2.40) together with a partial integeration to to yield

$$i \int d\mathbf{r}_\perp \, (\partial_x E_z^*) \epsilon \frac{(\partial_z \epsilon)}{\epsilon} E_x + \int E_z^* (\partial_z \epsilon) \left[i \partial_x + \frac{i}{\epsilon} (\partial_x \epsilon) \right] E_x \tag{2.42}$$

identifying

$$\int d\mathbf{r}_\perp \, \left[(M_0^\dagger)_{2,1} E_z^* \right] (\partial_z \epsilon) E_x + \int d\mathbf{r}_\perp \, E_z^* (\partial_z \epsilon) \left[(M_0)_{2,1} E_x \right] \tag{2.43}$$

adding the other nonvanishing term in (2.37),

$$\int d\mathbf{r}_\perp \, H_y^* \, \epsilon (-k (\partial_z \epsilon)) E_x = \int d\mathbf{r}_\perp \, \left[(M_0^\dagger)_{2,1} \, H_y^* \right] (\partial_z \epsilon) E_x \tag{2.44}$$

We finally get,

$$\langle\langle \psi_n | \frac{\partial M_0}{\partial z} | \psi_m \rangle\rangle = \int d\mathbf{r}_\perp \, \partial_z \epsilon \left(k_n E_{n,x}^* E_{m,x} + k_m E_{n,z}^* E_{m,z} \right) \tag{2.45}$$

This kind of manipulation is not limited to the two dimensional TM and can be generalized to the full $3D$ Maxwell equations. This term still carries with it a problem for the step profile waveguide, as E_x is discontinuous across the interface. This can be dealt with in a similar manner to coupled mode theory [Snyder83] using the continuity of the displacement field $D = \epsilon E$ and by

$$\partial_z \epsilon = (\epsilon_1 - \epsilon_2) \, \delta(f(x,y)) \tag{2.46}$$

$$\partial_z \frac{1}{\epsilon} = \left(\frac{1}{\epsilon_1} - \frac{1}{\epsilon_2} \right) \delta(f(x,y)) \tag{2.47}$$

This gives

$$\int d\mathbf{r}_\perp \, (\partial_z \frac{1}{\epsilon}) \left(k_n E_{n,x}^* E_{m,x} + k_m E_{n,z}^* E_{m,z} \right) dA = \tag{2.48}$$

$$= (\epsilon_1 - \epsilon_2) \left(\frac{1}{\epsilon_1 \epsilon_2} k_n D_{n,x}^* D_{m,x} + k_m E_{n,z}^* E_{m,z} \right) \Big|_{boundary} \tag{2.49}$$

which is well defined on the boundary.

2.3.5 Treating M_1

The last expression obtained (2.49) for the matrix elements of M_0 also facilitates the handling of the M_1 term ignored so far. We are assuming it to be small, and thus keep the decomposition in the eigenstates of the M_0 Hamiltonian. The correction to the equation of propagation (2.33) can be accounted for by adding M_1 to the equation of motion

$$i \frac{\partial C_n(z)}{\partial z} = \sum_{m \neq n} C_m(z) \exp \left(i \int_{-\infty}^{z} \left(k_n(\xi) - k_m(\xi) \right) d\xi \right) \times$$

$$\left[-i \frac{\langle\langle \psi_n | \frac{\partial M_0}{\partial z} | \psi_m \rangle\rangle}{k_n - k_m} + \langle\langle \psi_n | M_1 | \psi_m \rangle\rangle \right] + C_n \langle\langle \psi_n | M_1 | \psi_n \rangle\rangle, \tag{2.50}$$

The additional term in the equation can be calculated in a similar manner to (2.49), giving

$$\langle\langle \psi_n | M_1 | \psi_m \rangle\rangle = \int \mathrm{d}\mathbf{r}_\perp \left(\partial_z \epsilon\right) \left(E^*_{n,z} E_{m,z}\right) = \\ = \left(\epsilon_1 - \epsilon_2\right) \left(E^*_{n,z} E_{m,z}\right)\big|_{boundary}. \quad (2.51)$$

2.3.6 Absorbtion in the metal

For the Hamiltonian like description of Sec. (2.3.1) to be pseudo Hermitian, the parity operator is to be a linear and Hermitian. As it is proportional to the dielectric constant, this limits the formalism above to discussing the ideal metal $\Im\{\epsilon\} = 0$. However, for plasmonic applications, especially in the tapered focus case, dissipation in the metal is crucial for the estimation of the efficiency of the energy transfer. To consider the absorbtion in the metal, we include the exact complex wave number derived from the complex dielectric constant in the phase factor appearing in Eq. (2.33) but keep the mode functions and the inner product the same. This is equivalent to a stepwise operation of the dissipation between two propagation steps. We also recall that losses in each mode are proportional to the propagation constant, and therefore in the vicinity of mode matching condition, will only influence the total energy in the system.

2.3.7 Adiabatic processes

The description of the z-propagation as a Schrödinger equation leads naturally to the use of the adiabatic theorem. We shall consider an initial condition in which the state of the system is described by one of the normal modes of the Hamiltonian 2.3.1 and look for the condition under which the excitation will adiabatically follow this state.

Examining Eq.(2.3.1), assuming the system is in the initial state l, we can use $C_m = \delta_{m,l}$ to obtain

$$\frac{\partial C_m}{\partial z} = -C_l \frac{\langle\langle m | \frac{\partial M_0}{\partial z} | l \rangle\rangle}{k_l - k_m} \exp\left(i \int_{R_0}^{z} \left(k_m(\xi) - k_l(\xi)\right) d\xi\right) \qquad m \neq l \quad (2.52)$$

If the variation of k_l, k_m and $\partial_z M_0$ are slow in z, we can estimate the change in the occupancy of the other states by assuming them constant, and the resulting amplitude of the state m can be written as

$$C_m(z) \approx i \frac{\langle\langle m | \frac{\partial M_0}{\partial z} | l \rangle\rangle}{\left(k_l - k_m\right)^2} \left(\exp\left(i \int_{R_0}^{z} \left(k_m(\xi) - k_l(\xi)\right) d\xi\right) - 1\right) \qquad m \neq l. \quad (2.53)$$

This amplitude oscillates in time, and has no steady change over a long distance, making the jump unlikely. This expression also gives us the criteria for making an adiabatic passage. For the estimation to be valid, we require that the change of the Hamiltonian $\partial_z M_0$ over one period of the Rabi frequency between the states to be much smaller than the energy difference between the levels:

$$\left| \frac{\langle\langle m | \frac{\partial M_0}{\partial z} | l \rangle\rangle}{\left(k_l - k_m\right)^2} \right| \ll 1. \quad (2.54)$$

In addition, the coupling region in which the coupling of the mode is different than zero should be larger than the Rabi flipping length $L_{ex} = |(k_l - k_m)|^{-1}$ allowing for the exponential to average out. This criterion will be used later to identify the adiabatic regime, as we expect the coupling coefficients to fluctuate rapidly. This is the equivalent to the laser pulse area generating the Rabi oscillations in atomic systems being much larger than 1, setting the minimum time for an adiabatic process $\tau \sim 1/\Omega$.

2.3.8 Summary of theoretical scheme

To conclude, in this section we have devised a perturbative scheme to describe the evolution of a guided mode propagating along a varying waveguide, by mapping it onto a Schrödinger like equation. Knowing the eigenmodes of the translationally invariant wire for each cross section of the wire we write the varying waveguides fields as

$$\Phi(z) = \sum_m C_m(z) \exp\left(i \int_{-\infty}^{z} k_m(\xi) d\xi\right) \psi_m, \tag{2.55}$$

with ψ_m being the fields vector of the local mode. The coefficients C_m evolve according to

$$\begin{aligned} i\frac{\partial C_n(z)}{\partial z} = & \sum_{m \neq n} C_m(z) \exp\left(i \int_{-\infty}^{z} \Re\left\{k_n(\xi) - k_m(\xi)\right\} d\xi\right) \times \\ & \times \exp\left(i \int_{-\infty}^{z} \Im\left\{k_n(\xi) - k_m(\xi)\right\} d\xi\right) \times \\ & \times \left[-i\frac{\langle\langle \psi_n | \frac{\partial M_0}{\partial z} | \psi_m \rangle\rangle}{\Re\{k_n - k_m\}} + \langle\langle \psi_n | M_1 | \psi_m \rangle\rangle\right] - \frac{1}{2} C_n(z) \langle \psi_n | \frac{\partial \eta}{\partial z} | \psi_n \rangle. \end{aligned} \tag{2.56}$$

along with the phase condition in equation (2.36). We note again that this scheme is completely general, and that no assumptions were made regarding the two-dimensionality of the guide. It is thus applicable to arbitrary, three dimensional cross sectioned guide.

2.4 Tapering and mode transformation of a single plasmonic waveguide

We first demonstrate the suggested technique on a simple cases, namely the symmetrically expanding plasmonic slab depicted in Fig. (2.3). The idea behind this is both to test the numerical technique and gain intuition about how fast we can vary the width of the plasmonic guide while maintaining adiabaticity. The single symmetrically tapered slab equations simplify to the forward and backward propagating modes, as the symmetry of the problem makes the coupling between the long and short range plasmons zero. The equations of motion in this case are

$$\partial_z \begin{pmatrix} C_+ \\ C_- \end{pmatrix} = \left[\frac{\epsilon_1 - \epsilon_2}{2k_+} \begin{pmatrix} 0 & K_{+,-} \\ K^*_{+,-} & 0 \end{pmatrix} + \begin{pmatrix} \mathcal{T}_+ & \mathcal{T}_{+,-} \\ \mathcal{T}^*_{+,-} & \mathcal{T}_- \end{pmatrix}\right] \begin{pmatrix} C_+ \\ C_- \end{pmatrix} \tag{2.57}$$

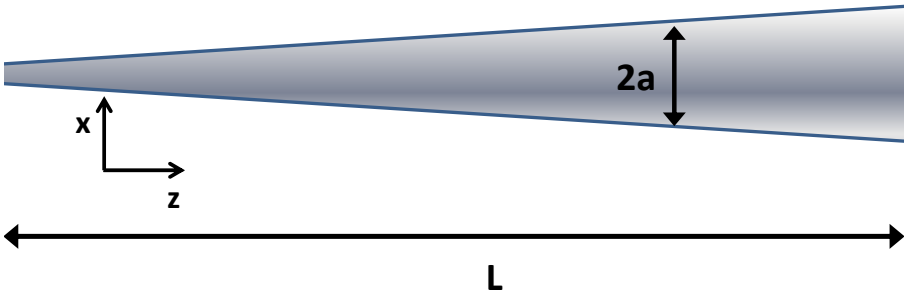

Figure 2.3: Geometry of the tapered plasmon waveguides considered in sec. 2.4. The initial excitation is propagating from the right towards the broader region.

with

$$K_{+,-} = e^{i\int_{R_0}^{z} 2k_+(\xi)d\xi}\left(\frac{k_+}{\epsilon_1\epsilon_2}|D_{+,x}|^2 + k_+|E_{+,z}|^2\right) = K^*_{-,+}$$
$$\mathcal{T}_+ = \frac{1}{2}e^{i\int_{R_0}^{z} 2k_+(\xi)d\xi}\left(\frac{1}{\epsilon_1\epsilon_2}|D_{+,x}|^2 + |E_{+,z}|^2\right) = \mathcal{T}^*_-$$
$$\mathcal{T}_{+,-} = \frac{1}{2}e^{i\int_{R_0}^{z} 2k_+(\xi)d\xi}\left(|E_{+,z}|^2\right)$$

and where we have used $k_+ = -k_-$, $D_{-,x} = D_{+,x}$ and $E^*_{-,z} = E_{+,z}$. In he last two relations we have adopted the conventions

$$\mathbf{E}_{-k} = \mathbf{E}_{\perp,+k} - E_{z,+k}\hat{\mathbf{z}}$$
$$\mathbf{E}_\perp, \mathbf{H}_\perp \textit{ are real}, \qquad E_z \textit{ is pure imaginary.}$$

Note, that the local coupled mode [Snyder65] equations are identical to those appearing in coupled mode theory, apart from a factor of k_+ appearing in the coupling matrix. This is due to the fact that the eigenmodes of the unperturbed propagation equation (2.29) are common to both methods. The key difference is in the inner product definition, and therefore in the normalization of the modes. For example, let us examine the normalization of the short range slab plasmon of Eq. (2.5): using coupled mode equations, where the normalization is based on the z-direction flux across the cross section of the wire $\int_A (E \times H^*)\cdot\hat{z}$ the normalization factor is (starting at the non normalized coefficients of Eq. (2.6))

$$N^2_{c.m.} = \frac{4k_n}{k_0}\left[\frac{1}{\epsilon_1\kappa_1} + \frac{e^{-2\kappa_2 a}}{\kappa_2\epsilon_2}\left(1 - \frac{\kappa_1\epsilon_2}{\kappa_2\epsilon_1}\right)^2\left(\frac{1}{2}\sinh(2\kappa_2 a) - \kappa_2 a\right)\right], \quad (2.58)$$

while, using the inner product suggest here,

$$N^2_{our} = 8\left[\frac{1}{\kappa_1} + \frac{e^{-2\kappa_2 a}}{\kappa_2}\left(1 - \frac{\kappa_1\epsilon_2}{\kappa_2\epsilon_1}\right)^2\left(\frac{1}{2}\sinh(2\kappa_2 a) - \kappa_2 a\right)\right], \quad (2.59)$$

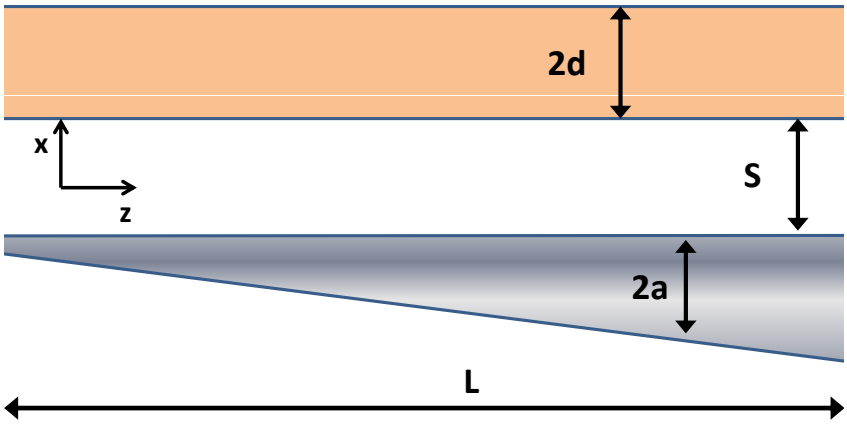

Figure 2.4: Geometry for the plasmon waveguide-dielectric waveguide tapered coupler considered here. the initial excitation is propagating in the lower, metallic waveguide, from the left along the expanding waveguide.

and the $\propto \sqrt{k_n}$ is again appearing. This result is useful in translating the results obtained here to flux. In the coupled mode theory, the amplitudes are directly related to the flux in a specific mode by the definition of of the inner product.

Performing the calculations, however, shows no energy transfer to either the back propagating or the long range plasmon. The energy of the surface plasmon remains in the forward propagating mode, though the amplitude of the fields increase. This result agrees well with several previous works [Babadjanyan00, Stockman04, Gramotnev05]. To understand this, we refer to Fig. (**??**) showing the dispersion curves. Assuming the Drude model and the diverging wave number, the group velocity of the plasmon decreases as it approaches the tip. The slowing down of the plasmon allows for dissipation into the metal, thus avoiding accumulation at the tip[Stockman04], this property was used by Stockman and others to show that a short range surface plasmon can be focused by focusing it towards the tip of a cone. In our calculations the reversed process occurs, yet the idea is the same. The slowly varying mode does not experiences back reflection when propagating along the expanding wire.

2.5 Adiabatic transfer into an adjacent dielectric waveguide

The main result of this chapter is to show that one can have an efficient transformation of energy between a tapered metallic slab and an adjacent dielectric waveguide. The structure consists of a thin silver nano slab of half width $a(z)$ and a glass waveguide of half width d, separated by a distance S surrounded by vacuum, as plotted in Fig. (2.4). As was the case for the single tapered slab, the dielectric constant of the silver

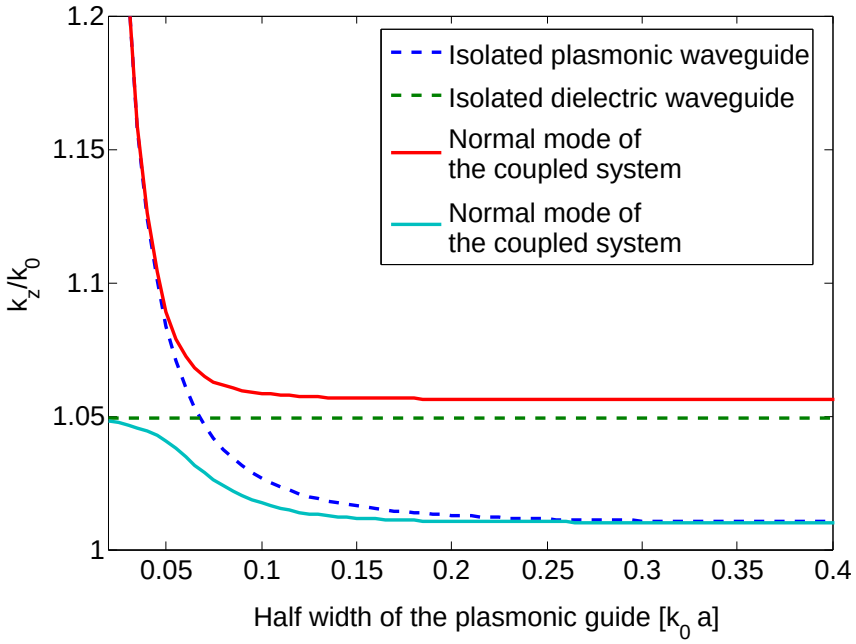

Figure 2.5: Avoided crossing used for adiabatic transfer. The plot shows the dispersion curves for an isolated Ag plasmonic slab waveguide (dashed, blue) as a function of the slab half width, for a glass dielectric waveguide (dashed,green) of fixed half width $d = 0.5/k_0$ and for the resulting two normal modes when the two guides are brought to a proximity of $s = 5/k_0$ (full lines). The avoided level crossing generates modes which transfer the energy from the dielectric to the metallic waveguide as the slab width is increased, and vise versa.

is corresponding to the vacuum wavelength $\lambda = 1\mu m$ [Johnson72], $\epsilon_m = -50 + 0.6i$ and the dielectric constant $\epsilon_d = 2.5$ typical for glass waveguide.

2.5.1 Avoided crossing with a waveguide

As the waveguide and the plasmonic slab are brought together, the overlap of the extended fields outside the guides ca uses the modes to hybridize, corresponding to off diagonal term in the Hamiltonian (2.21). This leads to an avoided crossing of the normal modes of the new Hamiltonian, depicted in Fig. (2.5). The gap between the two levels at the crossing point is plotted in Fig. (2.12) as a function of the distance between the slab and the waveguide, displaying an increase as the distance between the waveguides is reduced. As discussed above in Sec. (2.3.7) this gap also gives the length order on which adiabatic processes occur. We shall return to this below. It is important to note the shift of the waveguide mode due to the presence of the metallic slab, persisting far of resonance from the plasmonic mode. This is due to the extension of the fields of the guided mode, as can clearly be seen from the modes plotted in Fig.(2.10). This also means that care should be taken as to the the way the slab coupler ends, as the this will change the waveguide mode. This effect is not expected to cause energy transfer back to the plasmonic wire, as the two modes are far detuned at the end of the coupler, however

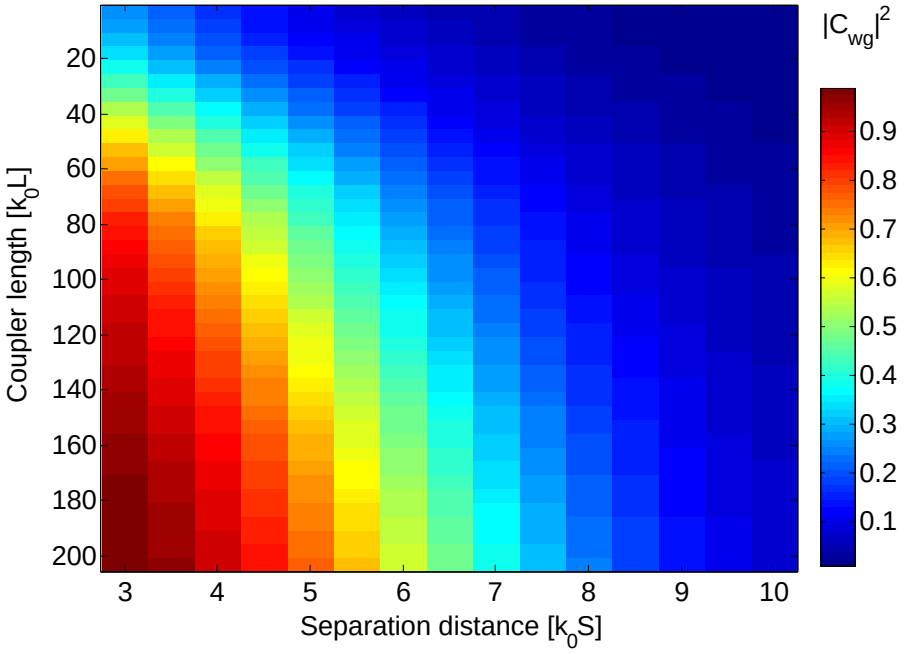

Figure 2.6: Fraction of the excitation transferred to the dielectric waveguide at the full length of the coupler L, as a function of the coupler length and the separation between the waveguides, when the dissipation in the metal is neglected (i.e., $\Im\{\epsilon\} = 0$).

abrupt ending can result in radiation out of the guide. The treatment of free propagating radiation modes is currently beyond the scope of this formalism due to the divergence of the inner product, and we therefore do not treat this problem here.

2.5.2 Adiabatic transfer of the energy from the plasmonic nano wire

In the calculation presented here we have chosen the dielectric waveguide half width $d = 0.5/k_0$ corresponding to a guided single mode of $k_z = 1.05k_0$. This k value is obtained in the plasmonic slab for a half width of $a = 0.06/k_0$. Throughout, the initial radius of the nanometallic slab is $a_i = 0.02/k_0$, the avoiding the reflections at the tip of the nanoslab [Stockman04] and the final width is $a_f = 0.2/k_0$. in both regimes the detuning of the two mode is far such the hybridized mode is identical to the isolated plasmonic mode (see Fig.(2.5)). We vary the length of the tapering and the separation between the wires. In the following, we compare the results with and without losses. In all calculations, four modes were considered, namely the forward and backward propagating short rang surface plasmon, and the waveguide modes. In principle all modes are to be taken into account but we restrict ourselves to four to facilitate faster calculations. To follow the description proposed above,

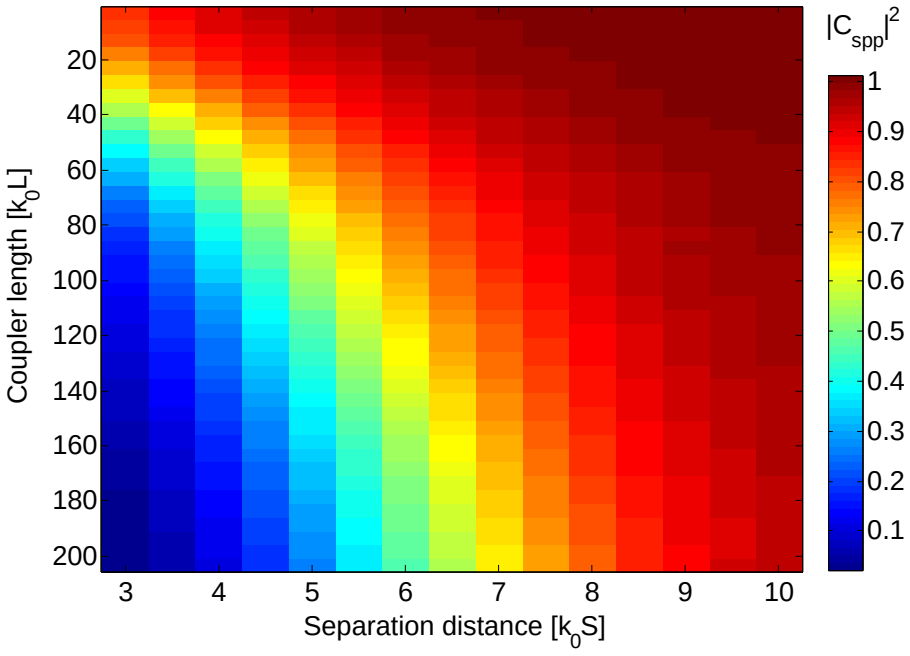

Figure 2.7: Fraction of the excitation remaining in the plasmon mode after the avoided crossing for as a function of the coupler length and the distance between the two waveguides, when the dissipation in the metal is neglected (i.e., $\Im\{\epsilon\} = 0$).

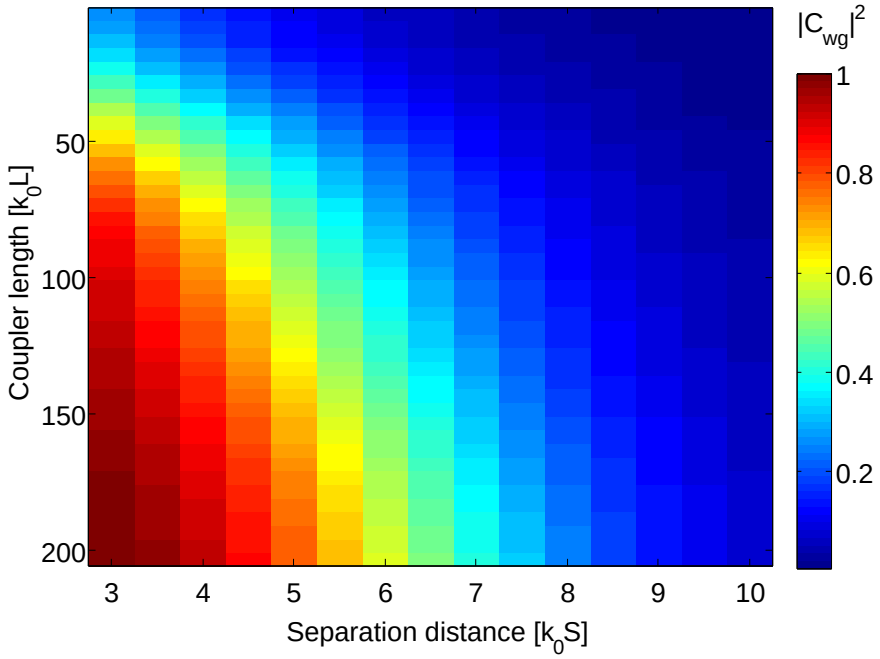

Figure 2.8: Fraction of the excitation transferred to the dielectric waveguide at the full length of the coupler L, as a function of the coupler length and the separation between the waveguides when dissipation in the metal is taken into account.

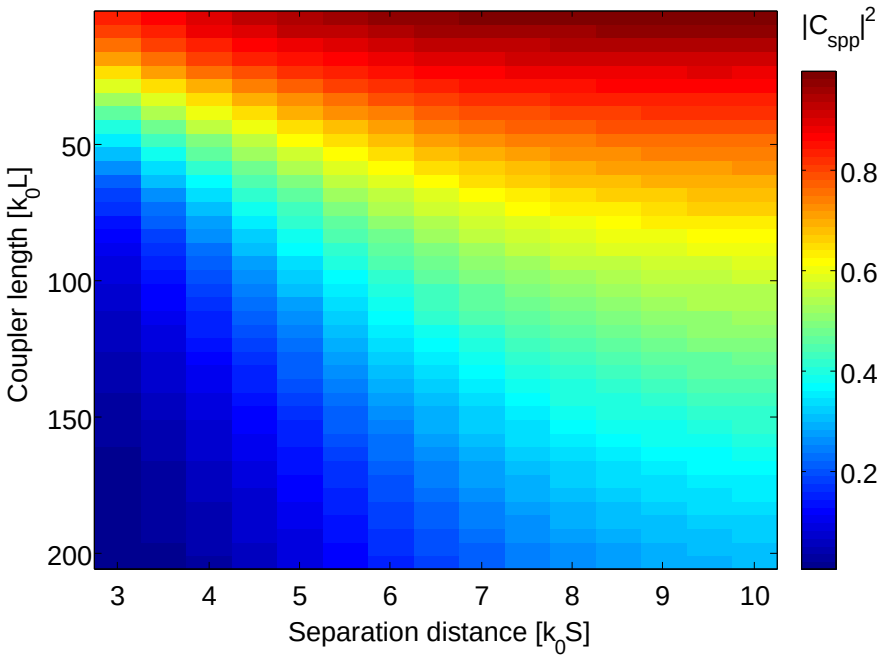

Figure 2.9: Fraction of the excitation remaining in the plasmon mode after the avoided crossing for as a function of the coupler length and the distance between the two waveguides.

we here use the normal modes, which can in general be calculated by two dimensional codes available, for arbitrary cross section.

In Figs. (2.6) and (2.7) we plot the efficiency of the adiabatic transformation, measured as a the fraction of the energy in the the upper and lower dressed states of Fig. (2.5) at the end of the structure. The transmission is calculated without dissipation in the metal (expressed by the imaginary part of the dielectric constant being set to zero). In Figs. (2.8) and (2.9) the same results are shown including the losses in the metallic slab. As the plasmon decay length induced by the addition of the imaginary part of the dielectric constant $L_{spp} = \frac{1}{2|\Im\{k\}|} \sim 120/k_0$ is larger than the transition length of the adiabatic taper, the results are shown to be largely unchanged, though the sum of fractions does no longer sum to one. It is shown that even with the introduction of dissipation, a 100% efficiency can be achieved, choosing slabs separation of $S = 2.5/k_0$ and a coupler length of $L \sim 200/k_0$.

In Fig. (2.11) we further verify the adiabatic character of the passage. As discussed above, the adiabatic regime is achieved when the Rabi oscillations between the modes are become rapid between adjacent slices of the tapering. The phase appearing in the integral of Eq. (2.33) should vary on the scale of 2π. This corresponds to the large phase factor in equation of motion of the mode. Comparing the phase coupling coefficients in the two limits, $L = 10/k_0$ and $L = 200/k_0$, shows the strong oscillation typical of the adiabatic regime for the longer coupler.

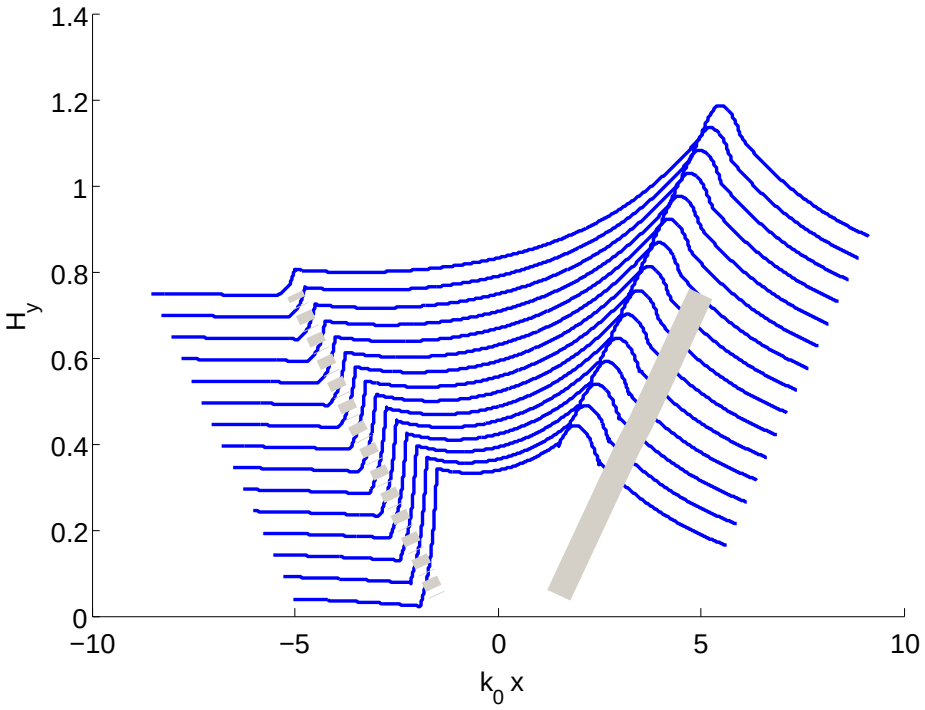

Figure 2.10: Magnetic field of the waveguide dressed state of the coupler for different separations between the metallic slab and the dielectric wave guide at the end of the coupler. Note that the waveguide mode is still change relative to the isolated waveguide, due to the extension of the fields outside the waveguide. The waveguide location is indicated by the gray line, while the metallic slab is dashed gray. The curves are shifted for readability.

Coupling length and comparison to evanescent couplers

Several authors have previously suggested coupling surface plasmons via evanescent coupling of two adjacent plasmonic waveguides [Gramotnev08] or wave number matched plasmonic and dielectric waveguides [Chang07a], and suggestions were made to prevent such coupling in future all plasmonic circuits [Veronis08]. In all such couplers the wave number matching results in Rabi-like oscillations of the energy between the two guides, induced by the evanescent fields coupling. Chang *et al.* [Chang07b] suggested that this can be used for coupling the surface plasmon out of an emitter-plasmon quantum optics setup. It is therefore worthwhile to examine the difference between the two mechanisms.

The coupling length for a complete transfer of the energy in the wavenumber mode matched situation is half a Rabi wavelength, defined by

$$L_c \equiv \frac{\pi}{|q_{sym} - q_{asym}|} \tag{2.60}$$

where the symmetric (q_{sym}) and anti-symmetric (q_{sym}) modes are the dressed modes of the combined system, shifted by the interaction between the guides. This coupling length does not change upon the intro-

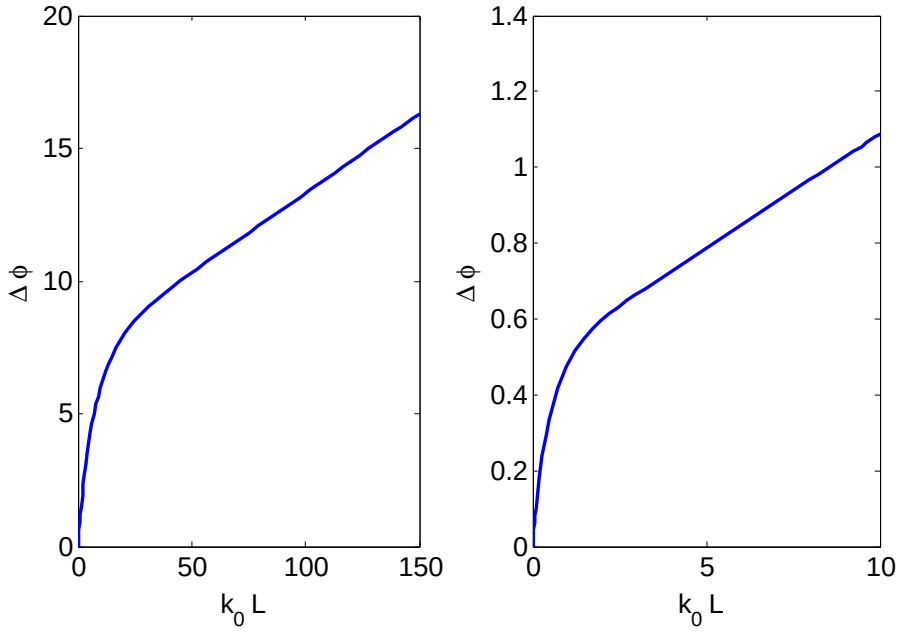

Figure 2.11: The accumulated phase factor in the equation of propagation. large phase change indicate rapid oscillations typical of the adiabatic regime.

duction of dissipation in the metal. The introduced decay length of the oscillations, defined as $L_p = 2/(\Im\{q_{sym}\} + \Im\{q_{asym}\})$, and the total total transferred energy is reduced according to [Veronis08]

$$P_{max} \sim \frac{e^{-2x \arctan x^{-1}}}{1+x^2}, \qquad x = \frac{2L_c}{\pi L_p}. \tag{2.61}$$

The resulting coupling length is plotted in Fig. (2.12), along with the dressed states gap. Complete transfer of the energy for the parameters explored above occurs for $L \sim 100/k_0$. For the adiabatic process however, this length scale is set by the length on which we can expect adiabaticity to appear. As was discussed, this can be explained by the length needed to avoid change in the amplitude of the initially unexcited modes:

$$\left| \frac{\langle\langle \partial_z M_0 \rangle\rangle}{(q_m - q_0)^2} \right|, \tag{2.62}$$

which here amounts to $L \sim 200/k_0 \sim 25\lambda_0$.

Though the lengths over are larger than those suggested for evanescent coupling based on the Rabi flipping, the length is only longer by a factor of two. This increases the losses, but on the other hand there are several advantages to the present method. In particular the suggested coupling is insensitive to small variations in the coupler length or the exact positioning of the wires (controlling the initial phase between the two oscillating modes) and the coupling region is controllable.

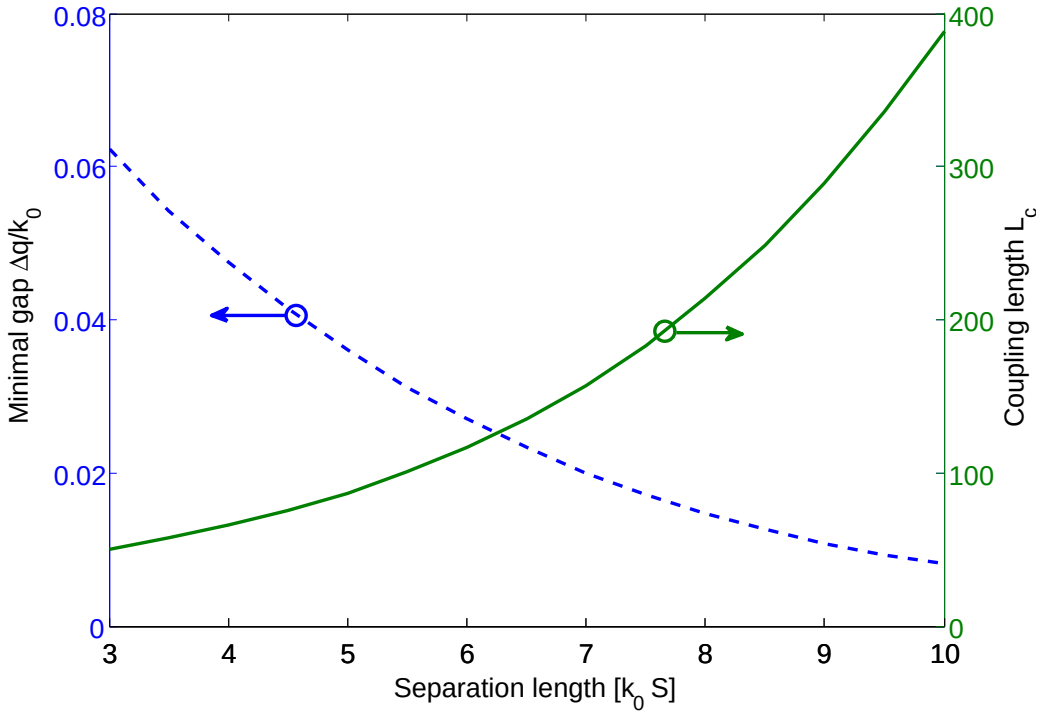

Figure 2.12: Blue curve (left axis), the gap in propagation constants Δq of the two normal modes appearing in Fig. (2.5) at the position of the avoided crossing, as a function of the separation between the two guides. In green (right axis) the coupling length $L_c \sim 1/\delta q$ for a Rabi flipping schemes (see text for details).

2.6 Conclusions

In this chapter we have demonstrated the possibility of adiabatic coupling of a surface plasmon propagating on a tapered matallic slab to an adjacent dielectric waveguide. We have shown that even with realistic metallic losses expected in silver slabs the expected efficiency is close to 100% of the incoming plasmonic energy. Though the slab configuration is not favorable experimentally due to one dimensional confinement only, the calculational technique developed here should be useful for arbitrary slow varying plasmonic guides. We have introduced and demonstrated the use of a general mapping of the Maxwell equation on a z-propagation Schrödinger like set of equations allowing the use of the full range of techniques available and understood in quantum mechanics. The key step in this is the use of the pseudo-Hermiticity reached by changing the inner product of states to include the local dielectric constant. This enables the full use of both orthogonality, completeness and evolution equation familiar from Hamiltonian quantum mechanics. Though unitarity is not preserved, we demonstrate a way to overcome this difficulty by correcting the equations of motion for the amplitudes of the normal modes decomposition. Thus, we provide a useful tool for the advancement of quantum optics application, avoiding the cumbersome three dimensional calculations otherwise required to evaluate these structure.

Chapter 3

Solid state plasmonic Lens structure

3.1 Introduction

A key idea to the strong coupling between quantum emitters and surface plasmons is that strong transverse confinement is a result of the large wavenumber of the surface plasmon in the direction of propagation. The decay length of the plasmon fields into the dielectric is determined by the difference between the wave number of the plasmon and that of a free propagting plasmon in the bulk $\kappa_d = \sqrt{k_{spp}^2 - \epsilon_d k_0^2}$. This naturally leads to consideration of strongly guiding structures, maximizing k_{spp} such as the ones considered in [Chang06, Gonzalez-Tudela12, Gramotnev07, Stockman04]. Such structures however suffer from propagation losses and require rapid coupling out as the one suggested in chapter (2).

A different approach to generating strong confinement can be taken using the interference of several sources of propagating surface plasmons. This idea has received much attention in recent years in the emerging field of Extra Ordinary Transmission (EOT) through thin metallic films (for a review see [Garcia-Vidal10a]). In the original experiment of Ebbesen *et al.* [Lezec02] strong, directional transmission through a subwavelength hole in an optically thick silver was observed when corrugations were added to both sides of the metallic film. Later investigation have shown the mechanism leading to this phenomena to be the excitation of plasmonic modes on the surface of the film on the side facing the light source, which then propagate through the hole and scatter out by the grating on the other side ([Carretero-Palacios11, Garcia-Vidal10a] and references therein). Since then multiple subwavelength holes and different geometries of the corrugations were investigated, both numerically and experimentally [Lerman09, Yanai09, Bulu11, Jun11, Aouani11b, Aouani11a]. In this chapter we suggest

In this chapter we examine an emitter placed above a structured metallic surface. The structure consists of concentric grooves, optimized to generate a coupling grating between light propagating perpendicular to the sample and radially propagating surface plasmons. These groove also generate a lossy cavity effect, as a fraction of the out-going plasmons are

reflect back towards the emitter. This results in significant increase of the emitter's decay rate. In addition, solid state quantum dots in layered semiconductor structures have their dipole moment aligned parallel to the plane of the lens, reducing the coupling efficiency to surface plasmon. To overcome this, we add a central groove to the metallic structure and show this results in improved coupling and higher decay rates.

The chapter is build as follows. We begin by a short review of the properties of plasmon propagating on the flat interface between a dielectric and a metal. We then describe the suggested structure to be used and go on to investigate the coupling grating and the central hole rules in enhancing the decay rate and collection efficiency in the radiated energy, and finally conclude our results.

3.2 Analysis of dipole decay in proximity of a metallic mirror

The decay rate of emitters can be change dramatically in the vicinity of metallic and dielectric boundaries, as this allows for large changes in the density of states at the emitter location. In this section we review the decay rate analysis of a dipole in the vicinity of an infinite, flat boundary. The advantage of this analysis is the availability of an analytic solution which will allow the separation into different channels of the decay. This analysis will become useful later, when the more elaborated structures are introduced, and the results to follow will serve as a basis for the comparison. We follow here the analysis of Sipe [Sipe81] using the plane wave decomposition of the fields. In this description, the dipole electric field can be written as

$$\mathbf{E}(\mathbf{r}) = F(r - r_0) \cdot \boldsymbol{\mu} \tag{3.1}$$

$\boldsymbol{\mu}$ being the dipole moment located at r_0. The tensor F can be decomposed into

$$F(r - r_0) = \int \frac{d\boldsymbol{\kappa}}{(2\pi)^2} F(\boldsymbol{\kappa}; z - z_0) e^{i\boldsymbol{\kappa}\cdot(\rho-\rho_0)} \tag{3.2}$$

where ρ (ρ_0) is the projection of the position vector $\mathbf{r}$ ($\mathbf{r}_0$ on the plane of the mirror, the $x - y$ plane. The decomposition into plane waves of component κ along the surface can to be understood as plane waves propagating from or to the interface from both sides, with the wave vector:

$$\boldsymbol{\nu}_{i\pm} = \kappa\hat{\kappa} \pm k_z\hat{z} \tag{3.3}$$

where the size of wave vector, $\nu_i = \sqrt{\epsilon_i}k_0$ is the wave vector for propagation in medium i, and $k_0 = \omega/c$. Note that the integral in Eq.(3.2) as well as the momenta decompositions to follow, is calculated over all $\boldsymbol{\kappa}$, including both propagating and evanescent waves ($\kappa > \nu$). The polarizations for the waves depicted in Fig.(3.1), with

$$\hat{p}_{i,\pm} = \nu_i^{-1} \left(\kappa\hat{z} \mp k_z\kappa\right)$$

for p-polarized waves and

$$\hat{s} = \hat{\kappa} \times \hat{z}$$

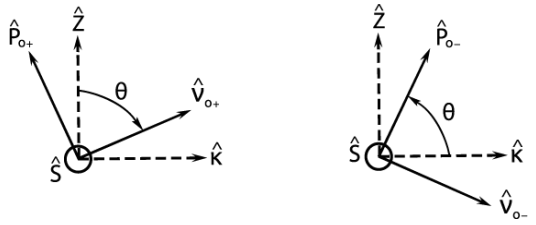

Figure 3.1: The polarization used for the fields decomposition

for s-polarized waves.

The calculation of the total fields can now be solved using the transfer matrix technique by writing

$$\begin{aligned}\mathbf{E}_0(\mathbf{r}) &= E_{0+}e^{i\nu_{0+}\cdot\mathbf{r}} + E_{0-}e^{i\nu_{0-}\cdot\mathbf{r}} \\ \mathbf{E}_1(\mathbf{r}) &= E_{1+}e^{i\nu_{1+}\cdot\mathbf{r}} + E_{1-}e^{i\nu_{1-}\cdot\mathbf{r}}\end{aligned} \tag{3.4}$$

above and below the interface, respectively, and requiring the amplitudes to be related via a transfer matrix M

$$M = \frac{1}{T_{01}^{s,p}}\begin{pmatrix} 1 & R_{01}^{s,p} \\ R_{01}^{s,p} & 1 \end{pmatrix},$$

with $R_{01}^{s,p}$ ($T_{01}^{s,p}$) being the reflection (transmission) Fresnel coefficient from the dielectric to the metal, defined according to the polarization of the impinging wave.

The dipole problem can now be solved as follows. Above the dipole position $\mathbf{r}_0 = d\,\hat{z}$, the electric field is the field emitted by the dipole plus the surface response. The surface response to the dipole field is obtained by inserting the dipole source decomposition (3.2) into the transfer matrix equations 3.4, and using the Fresnel coefficients for the reflection and transmission through the surface. The resulting outgoing field in the positive z direction, above the dipole location is given by

$$\mathbf{E}_0 = \int \frac{id\boldsymbol{\kappa}}{2\pi k_z}\mathbf{e}_0(\kappa)e^{i\nu_{0+}\cdot\mathbf{r}} \tag{3.5}$$

where the field amplitude $\mathbf{e}_0(\kappa)$ are the coherent sum of the direct field emitted by the dipole, and the reflected radiation from the surface;

$$\begin{aligned}\mathbf{e}_0(\kappa) &= \nu_0^2\left[\hat{s}\mu_{s0} + \hat{p}_{0+}\mu_{p0}\right] \\ \mu_{s0} &= \hat{s}\cdot\mu\left[e^{-ik_{z,0}d} + R_{01}^{s}e^{ik_{z,0}d}\right] \qquad (3.6) \\ \mu_{p0} &= \hat{p}_{0+}\cdot\mu e^{-ik_{z,0}d} + \hat{p}_{0-}\cdot\mu R_{01}^{p}e^{ik_{z,0}d}. \qquad (3.7)\end{aligned}$$

The corresponding magnetic field can be derived from Maxwell equations using the electric field. It has same functional form as the electric field with

$$\mathbf{b}_0(\kappa) = \hat{v}_0 \times \mathbf{e}_0(\kappa)$$

This allows the calculation of emitted power as the sum of the in-plane component κ contributions

$$W_0 = \int_{interface}\mathbf{S}(\mathbf{r})\cdot\hat{z}d^2\rho = \frac{c\nu_0^3}{8\pi}\int_{\kappa<\nu_0}\frac{d^2\kappa}{k_z}\left[|\mu_{p0}|^2 + |\mu_{s0}|^2\right]. \tag{3.8}$$

The decay rate can also be calculated from the reaction of the mirror on the dipole. Recalling that the dipole decay rate is determined by the reflected field at the dipole position:

$$\Gamma = \frac{1}{2}\omega\Im(\boldsymbol{\mu}^* \cdot \mathbf{E}(\mathbf{r}_\mu) \tag{3.9}$$

The decay rate is thus the limit of the above calculated fields at the position of the dipole:

$$\begin{aligned}\frac{\Gamma}{\Gamma_0} = \mu_{||}^2 \left[1 + \frac{3}{4\nu_0}\Re\int_0^\infty \frac{\kappa d\kappa}{k_z}\left(R_{01}^s - \frac{k_z^2}{\nu_0^2}R_{01}^p\right)e^{2ik_z d}\right] + \\ + \mu_z^2\left[1 + \Re\frac{3}{2\nu_0}\int_0^\infty \frac{\kappa d\kappa}{k_z}\left(\frac{\kappa^2}{\nu_0^2}R_{01}^p\right)e^{2ik_z d}\right],\end{aligned} \tag{3.10}$$

where $\Gamma_0 = \frac{1}{3}\omega k_0^3 |\mu|^2$is the dipole decay rate in free space, and $\mu_z = |\boldsymbol{\mu}\cdot\hat{z}|$ and $\mu_z = |\boldsymbol{\mu} - (\boldsymbol{\mu}\cdot\hat{z})\cdot\hat{z}|$ are the dipole's projections out-of and in plane respectively. We again emphasis that the integral in 3.10 contains momentum components $\kappa > \nu_0$ corresponding to evanescent, near field contribution. These are at the core of this work, as we shall explain below. In contrast, in the radiated energy (3.8) only propagating waves contribute, as noted in the integration. The total decay rate for different position of the dipole emitter above a silver mirror is plotted in blue in Fig. (3.2).

The analytic form of the decay rate is useful in distinguishing the different decay mechanisms for the emitter coupled to this system to decay into. Examining the integral in Eq. (3.10), we can separate it into two parts. For wave numbers below the medium's light wave number, the decay is in to a mode that can propagate out of the system, representing radiative decay process. This contribution is plotted in red Fig. (3.3). As expected, the decay rate due to radiative process remains constant at large distances from the mirror, oscillating about $\Gamma_{rad}/\Gamma_0 = 1$. Significantly, for a dipole orientation perpendicular to the mirror, there exist a "dark spot" where due to destructive interference between the emitted and reflected field no radiative coupling exist. In the following we distinguish the two other processes, i.e. the plasmonic modes and the non radiative losses. This distinction will become useful later on in analyzing the more elaborate structures. For this end, we plot in Fig.(3.3) the integrand of Eq. (3.10) for $\kappa > \nu_0$. The existence of a resonance in the response function is apparent. The decay rate appearing in equation (3.10) is the imaginary part of the response green function of the metallic surface at the position of the dipole. In the absence of metal losses ($\Im\epsilon = 0$) this Green's function will display poles, corresponding to resonances with the plasmon mode. Taking into account the medium absorption, i.e., a small but finite value of $\Im\epsilon \neq 0$ the plasmonic modes turn into resonances with a finite width. This means that in case of losses there is no longer a single, well-defined κ but continuously many κ values peaked around k_{pl} that contribute to the plasmon mode. This is clearly visible in Fig.(3.3). In the above analysis, it is easy to see that this resonance accurse at $\kappa = k_0\sqrt{\frac{\epsilon_m\epsilon_0}{\epsilon_0+\epsilon_m}}$ the flat interface plasmon dispersion relation discussed in the introduction.

A key motivation to the work presented here, is evident when examining Fig. (3.4). In this plot, the energy fraction decayed into the plasmon

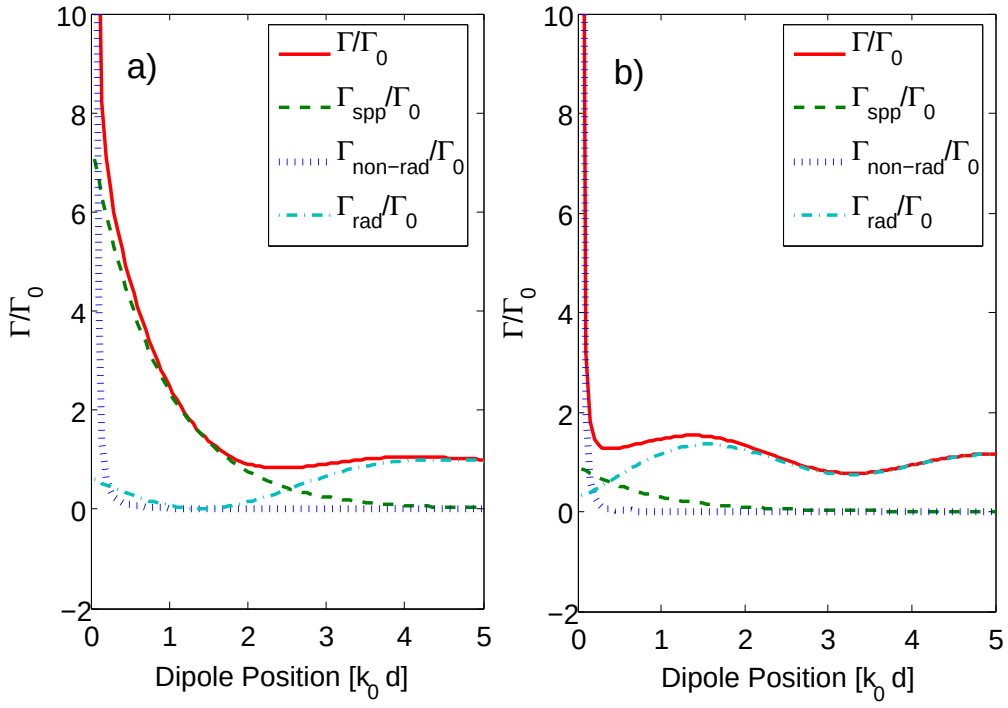

Figure 3.2: Different contributions to the decay rate for a dipole emitter above a flat mirror d. In a), the decay rate for a dipole moment perpendicular to the surface, where a "dark spot" for the radiation decay channel is noticeable. In b) the decay rate for a dipole moment parallel to the surface. Note the overall lower decay rate, and in particular the lower decay rate to the plasmon decay channel, indicating weaker coupling of the dipole to the plasmon.

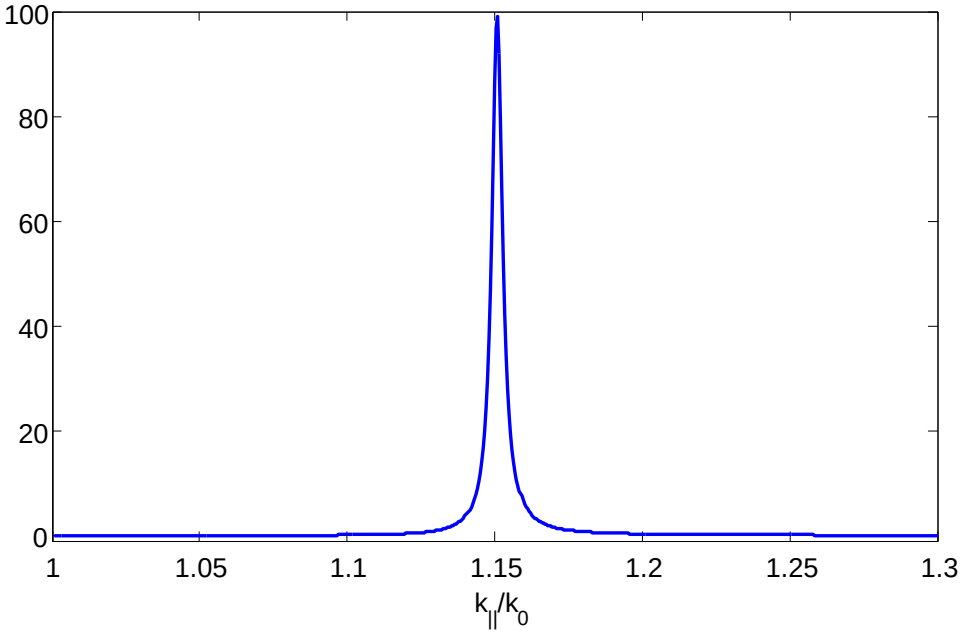

Figure 3.3: Evanescent part of the in plane momenta distribution for a flat mirror

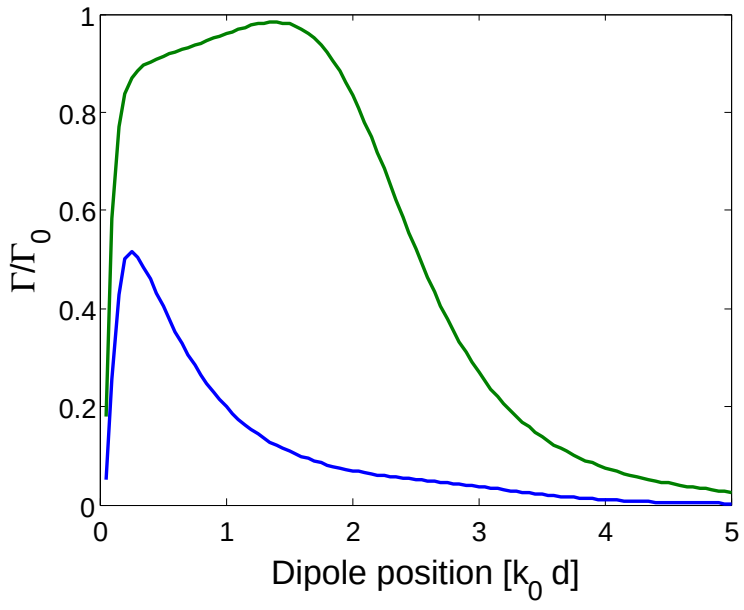

Figure 3.4: Energy fraction decayed into the plasmon channel for both configuration of the dipole above the surface. Note that for the dipole in the parallel configuration only a little above half the energy can be coupled to the plasmonic channel

channel is plotted as a function of the dipole position above the mirror, for the two orientations of the dipole appearing in Eq. (3.10). For the dipole oriented perpendicular to the surface, up to 99.5% of the energy can decay into exciting SPPs. It is for this reason that most quantum information applications utilizing the plasmon confinement focused on this configuration [Chang06]. In the solid state systems we wish to consider here however, the dipole orientation in the system is determined by the layered structure growth, and is oriented in the mirror's plane. For this configuration, the maximal coupling efficiency obtained is 52% of the dipole emission, as can be seen in Fig. (3.4). Another feature which can be extracted from the simple model of the infinite mirror are the field and energy distributions on the surface of the mirror and in the far field. These will become useful when comparing the distributions of the more elaborate structures presented in this work.

As we will be interested in structures preserving the axial symmetry, it is useful to develop the fields in cylindrical coordinates. We will require both the fields at the surface of the device, and in the far field. Above, the expression for the fields was developed for an observation point above the dipole position.In the volume between the dipole and the mirror, equation (3.7) is slightly altered, by changing the propagation vector and polarization of the direct radiation fields from dipole $\nu_{0,+} \rightarrow \nu_{0,-}$, $\hat{p}_{0,+} \rightarrow p,\hat{}-$:

$$\mathbf{e}_0(\kappa) = \nu_0^2 \left[\hat{s}\mu_{s0} + \hat{p}_{0+}\mu_{p0}\right] \tag{3.11}$$

$$\mu_{s,0} = \hat{s} \cdot \boldsymbol{\mu} \left[e^{-ik_{z,0}d} + R_{01}^{s} e^{ik_{z,0}d}\right] \tag{3.12}$$

$$\mu_{p,0} = \hat{p}_{0,-} \cdot \boldsymbol{\mu} e^{-ik_{z,0}d} + \hat{p}_{0-} \cdot \boldsymbol{\mu} R_{01}^{p} e^{ik_{z,0}d}.. \tag{3.13}$$

Using the expansion of the exponential into spherical coordinates (here, $\mathbf{r} = (\rho_R, \phi_R, z_R)$

$$e^{i\nu_{0,\pm}\cdot\mathbf{r}} = e^{\pm i\frac{k_z}{\nu_0}z_R}\left(\sum_{n=-\infty}^{\infty} i^n J_n(\frac{\kappa}{\nu_0}\rho_R)e^{in(\phi_R-\phi_\kappa)}\right), \tag{3.14}$$

and

$$\hat{s}\cdot\boldsymbol{\mu} = \mu_{||}\sin(\phi_\kappa) \tag{3.15}$$

$$\hat{p}_{0,\pm}\cdot\boldsymbol{\mu} = \frac{1}{\nu_0}(\kappa\hat{z} \mp k_z\hat{\kappa})\cdot\boldsymbol{\mu} = \frac{\kappa}{\nu_0}\mu_z \mp \frac{k_z}{\nu_0}\boldsymbol{\mu}_{||}\cos(\phi_\kappa) \tag{3.16}$$

yielding, after some manipulation, the field in cylindrical coordinates:

$$\begin{aligned}
\mathbf{E}(\mathbf{r}) = \nu_0^2\int\frac{\kappa\,d\kappa}{k_z}e^{ik_z d}\Big\{&\mu_z\Big[(J_{-1}(\kappa R_{||})\hat{j}_+ - J_1(\kappa R_{||})\hat{j}_-)\times\\
&\times\left(e^{-i\frac{k_z}{\nu_0}z_R} - R_{01}^p e^{i\frac{k_z}{\nu_0}z_R}\right)\frac{\kappa k_z}{\nu_0^2} + iJ_0(\kappa R_{||})\left(e^{-i\frac{k_z}{\nu_0}z_R} - R_{01}^p e^{i\frac{k_z}{\nu_0}z_R}\right)\Big] +\\
+\frac{\mu_{||}}{2}\Big[&i\left(e^{-i\frac{k_z}{\nu_0}z_R} + R_{01}^s e^{i\frac{k_z}{\nu_0}z_R}\right)\left(J_0(\kappa R_{||})e^{i\phi_r} + J_{-2}(\kappa R_{||})e^{-i\phi_r}\right)\hat{j}_+ +\\
&+i\left(e^{-i\frac{k_z}{\nu_0}z_R} + R_{01}^p e^{i\frac{k_z}{\nu_0}z_R}\right)\left(J_0(\kappa R_{||})e^{i\phi_r} - J_{-2}(\kappa R_{||})e^{-i\phi_r}\right)\frac{k_z^2}{\nu_0^2}\hat{j}_+ +\\
&+i\left(e^{-i\frac{k_z}{\nu_0}z_R} + R_{01}^s e^{i\frac{k_z}{\nu_0}z_R}\right)\left(J_2(\kappa R_{||})e^{i\phi_r} + J_0(\kappa R_{||})e^{-i\phi_r}\right)\hat{j}_- +\\
&+i\left(e^{-i\frac{k_z}{\nu_0}z_R} + R_{01}^p e^{i\frac{k_z}{\nu_0}z_R}\right)\left(J_0(\kappa R_{||})e^{-i\phi_r} - J_2(\kappa R_{||})e^{i\phi_r}\right)\frac{k_z^2}{\nu_0^2}\hat{j}_- +\\
&\left(e^{-i\frac{k_z}{\nu_0}z_R} + R_{01}^p e^{i\frac{k_z}{\nu_0}z_R}\right)\left(J_{-1}(\kappa R_{||})e^{-i\phi_r} - J_1(\kappa R_{||})e^{i\phi_r}\right)\frac{\kappa k_z}{\nu_0^2}\hat{z}\Big]\Big\},
\end{aligned} \tag{3.17}$$

Where $\hat{j}_\pm = \frac{1}{2}(\hat{\rho} \pm i\hat{\phi})$, and J_m are the Bessel functions of order m.

The far field radiation intensity can be calculate simplifying Eq.(3.5). In this limit the integral can be replaced by the

$$\mathbf{E}_0 = \int\frac{idk}{2\pi k_z}\mathbf{e}_0(\kappa)e^{i\nu_{0+}\cdot\mathbf{r}}\,\mathbf{e}_0(\nu_0\sin(\theta))\frac{e^{i\nu_{0+}R}}{R}, \tag{3.18}$$

$R = |\mathbf{R}|$ is the distance to the observation point and θ the angle to the axis of symmetry. The intensity radiated to a solid angle $d\Omega$ in far field is defined as

$$\frac{dI}{d\Omega} = R^2\hat{R}\cdot\hat{S} = R^2\frac{c}{8\pi}\hat{R}\cdot\Re(\mathbf{E}\times\mathbf{H}^*). \tag{3.19}$$

The explicit expression for the radiation in the far field is thus,

$$\frac{dI}{d\Omega} = \frac{3}{8\pi}\left\{|\mu_z|^2(\sin(\theta))^2\left|1 + R_{01}^p e^{2ik_z d}\right|^2 + \right. \tag{3.20}$$

$$\left. + \frac{1}{2}|\mu_{||}|^2\left[\left|1 + R_{01}^s e^{2ik_z d}\right|^2 + \frac{k_z}{\nu_0}\left|1 - R_{01}^p e^{2ik_z d}\right|^2\right]\right\}. \tag{3.21}$$

The resulting radiation pattern is plotted for the parallel dipole orientation is plotted in Fig. (3.5), for different dipole positions d above the

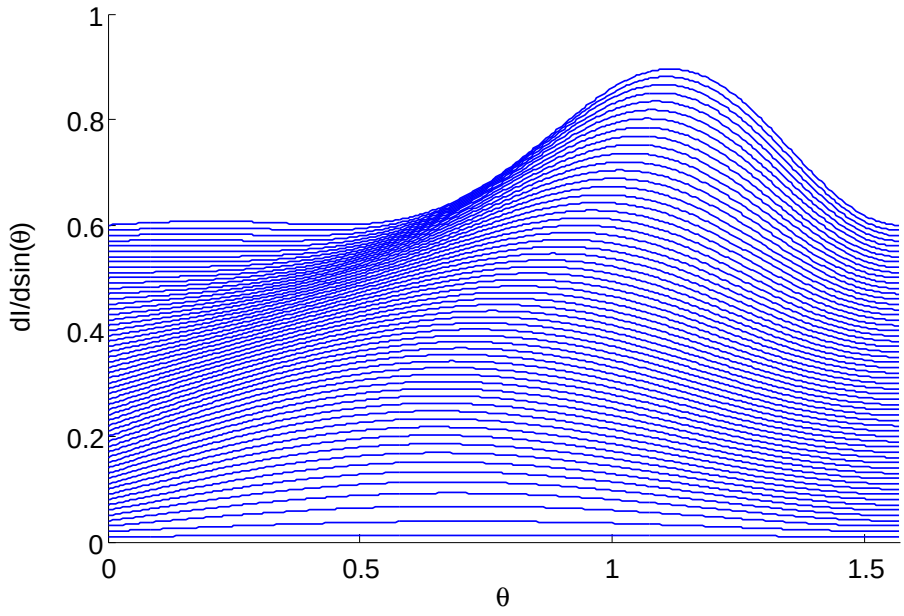

Figure 3.5: Radiation pattern from a flat mirror as a function of the position of the dipole above the mirror. Different position are shifted for visibility.

surface. Note that since the SPP and free propagating radiation are momentum mismatched, as mentioned in the introduction, strong coupling to the SPP modes results in reduced amount of far field radiated energy. Thus, though SPP modes allow for sub wavelength focusing of the electromagnetic fields, and so strong coupling to single emitters, the flat mirror configuration presents two difficulties: the coupling of the SPP mode to measurable radiation, and the limited coupling to the in-plane dipole orientation. In the following we address both problems.

3.3 Plasmonic lens structure considered

For plasmon propagating on a flat interface to become useful for coupling free propagating photons to single emitters in solid state, the two issues discussed in the previous section to be addressed. The propagating plasmon is to be efficiently coupled out into radiation, and the coupling efficiency between the dipole emitter parallel to the surface is to be increased.

In this work we investigated the coupling efficiency, directionality, and enhancement of the decay rate for a structure depicted in Fig. (3.6), The structure consists of a cylindrical central hole of depth h and radius a engraved in interface between a Ag layer and GaAs at which a quantum dot is embedded. Surrounded by cylindrical grooves The quantum dot is placed on the axis of symmetry of the structure, above and in the central hole. The central hole is designed to increase the coupling of the in plane dipole moment of the quantum dot to the surface plasmon propagating on the surface, while the concentric grooves serve as a grating coupler, beaming the energy into a directional radiation of a narrow cone. The

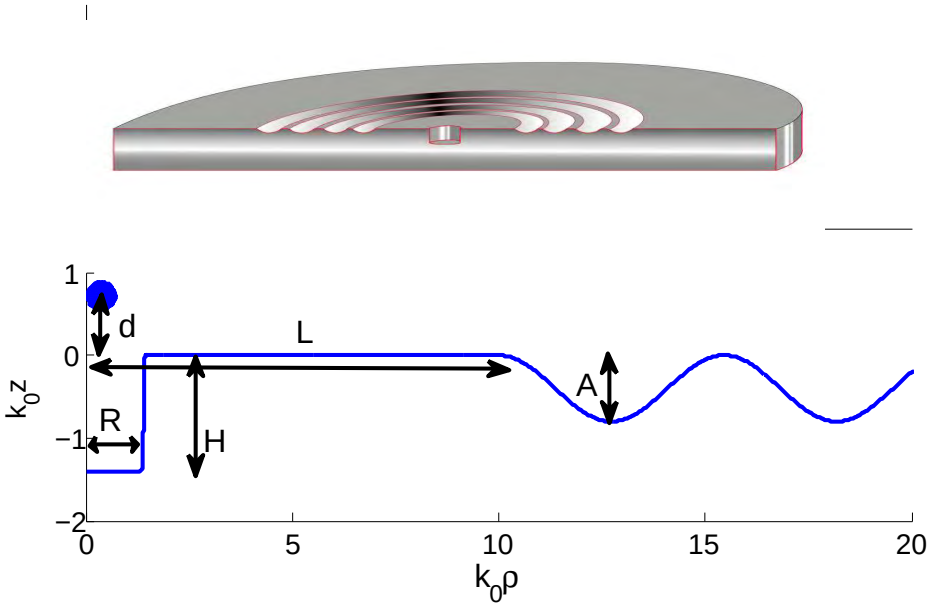

Figure 3.6: Radial cross section of the lens considered.

distance between the first groove and the central hole serves as a cavity, using the in plane scattering of the plasmon form the grating to further enhance the coupling to the surface plasmon. Although it was recently shown [Andersen10] that in the case of quantum dots coupled to surface plasmon size effects of the dot can be measured, in this work the quantum dot will be considered a point emitter, i.e. a point dipole. The permittivity values for both the Ag and the and the $GaAs$ were taken from [Johnson72].

3.4 Numerical method used to investigate the structure

The numerical investigations of the structure suggested here was done with an implementation of the boundary element method (BEM) for electromagnetic simulations presented in Ref.[García de Abajo02]. In this section we shall review the main concept of the method. The full details of the implementations appear in Appendix A due to their length. The calculation is preformed in the frequency domain. We assume that our system contains a set of known, time-harmonic source charges and currents $e^{-i\omega t}$ in the presence of some scattering dielectric body whose surface is denoted ∂V_i, with i denoting the side of the interface considered. The Maxwell equations in continuous media can be written as (in this work,

as in the referenced paper, cgs units are used)

$$\nabla \cdot \mathbf{D} = 4\pi\varrho \tag{3.22}$$
$$\nabla \cdot \mathbf{B} = 0 \tag{3.23}$$
$$\nabla \times \mathbf{H} + ik\mathbf{D} = \frac{4\pi}{c}\mathbf{j} \tag{3.24}$$
$$\nabla \times \mathbf{E} - ik\mathbf{B} = 0, \tag{3.25}$$

where harmonic time dependance $e^{-i\omega t}$ is assumed for all quantities, c is the speed of light and $k = \omega/c$ is the vacuum wave number. Further, I assume the constitutive relations $\mathbf{D} = \epsilon\mathbf{E}$ and $\mathbf{B} = \mu\mathbf{H}$. For the rest of this work, $\mu = 1$ is assumed.

If the dielectric constant ϵ is spatially varying as is the case for our structure, the fields cannot easily be rewritten in terms of the electric potential Φ and vector potential A without artificial source terms appearing in the equations corresponding to $\nabla\epsilon$. We can however, treat each part of space where the dielectric constant is spatially independent separately. Thus writing

$$\mathbf{E} = ik\mathbf{A} - \nabla\Phi \tag{3.26}$$
$$\mathbf{H} = \nabla \times \mathbf{A} \tag{3.27}$$

Because of the non trivial geometry of the problem, finding the Green's function for the entire space is a complicated task. However, given the boundary charges and currents on the interface allows the usage of the well known free space form of the Green's function for the Helmholtz equation:

$$G_i = \frac{e^{ik_i r}}{r}, \tag{3.28}$$

with $k_i = \sqrt{\epsilon_i}k$ the wave number in medium i. The vector potentials $\mathbf{A}_i(r)$ and $\Phi_i(r)$ in each region $\{\mathbf{r} \in V_i\}$ can then be written in the form

$$\mathbf{A}_i = \frac{1}{\epsilon_i}\int_{V_i} d\mathbf{r}' G_i\left(|\mathbf{r}' - \mathbf{r}|\right)\mathbf{j}(\mathbf{r}') + \int_{\partial V_i} d\mathbf{s} G_i\left(|\mathbf{s} - \mathbf{r}|\right)\mathbf{h}_i(\mathbf{s}) \tag{3.29}$$
$$\Phi_i = \frac{1}{c}\int_{V_i} d\mathbf{r}' G_i\left(|\mathbf{r}' - \mathbf{r}|\right)\rho(\mathbf{r}') + \int_{\partial V_i} d\mathbf{s} G_i\left(|\mathbf{s} - \mathbf{r}|\right)\sigma_i(\mathbf{s}), \tag{3.30}$$

With $\mathbf{j}, \rho$ the external charge and current distributions in the problem and $\mathbf{h}, \sigma$ the induced charges and currents on the interface between the media. A Lorenz-like gauge, i.e. $\nabla \cdot \mathbf{A} = ik\epsilon\Phi$, was used. In the BEM method, the charge and current on the on the boundary are replaced by two sets of distributions on both sides of the interface to satisfy the boundary conditions and justify the use of 3.28. In general, the resulting effective distributions do not have physical significance; they do not correspond to actual charges and currents, and the distributions in region V_1 and region V_2 may not necessarily be equal. The boundary conditions to be satisfied

are the continuity of the potential Φ,

$$\int d^2sG_1(\mathbf{s},\mathbf{s}')\,\sigma_1(\mathbf{s}') - \int d^2sG_2(\mathbf{s},\mathbf{s}')\,\sigma_2(\mathbf{s}') = \Phi_2^e - \Phi_1^e \tag{3.31}$$

$$\int d^2sG_1(\mathbf{s},\mathbf{s}')\,\mathbf{h}_1(\mathbf{s}') - \int d^2sG_2(\mathbf{s},\mathbf{s}')\,\mathbf{h}_2(\mathbf{s}') = \mathbf{A}_2^e - \mathbf{A}_1^e \tag{3.32}$$

$$\begin{aligned}&\int d^2s\,(\mathbf{n}_s\cdot\nabla)\,G_1(\mathbf{s},\mathbf{s}')\,\mathbf{h}_1(\mathbf{s}') - \int d^2s\,(\mathbf{n}_s\cdot\nabla)\,G_2(\mathbf{s},\mathbf{s}')\,\mathbf{h}_2(\mathbf{s}') -\\ &- ik\mathbf{n}_s\left(\epsilon_1\int d^2sG_1(\mathbf{s},\mathbf{s}')\,\sigma_1(\mathbf{s}') - \epsilon_2\int d^2sG_2(\mathbf{s},\mathbf{s}')\,\sigma_2(\mathbf{s}')\right) = \boldsymbol{\alpha}\end{aligned} \tag{3.33}$$

$$\begin{aligned}&\epsilon_1\int d^2s\,(\mathbf{n}_s\cdot\nabla)\,G_1(\mathbf{s},\mathbf{s}')\,\sigma_1(\mathbf{s}') - \epsilon_2\int d^2s\,(\mathbf{n}_s\cdot\nabla)\,G_2(\mathbf{s},\mathbf{s}')\,\sigma_2(\mathbf{s}') -\\ &- ik\mathbf{n}_s\left(\epsilon_1\int d^2sG_1(\mathbf{s},\mathbf{s}')\,\mathbf{h}_1(\mathbf{s}') - \epsilon_2\int d^2sG_2(\mathbf{s},\mathbf{s}')\,\mathbf{h}_2(\mathbf{s}')\right) = D,\end{aligned} \tag{3.34}$$

with the source terms

$$\Phi_i^e = \frac{1}{\epsilon_i}\int d^3rG_i(\mathbf{s},\mathbf{r})\,\rho_i(\mathbf{r}) \tag{3.35}$$

$$\mathbf{A}_i^e = \frac{1}{c}\int d^3rG_i(\mathbf{s},\mathbf{r})\,\mathbf{j}_i(\mathbf{r}) \tag{3.36}$$

$$\boldsymbol{\alpha} = (\mathbf{n}_s\cdot\nabla_s)\,(\mathbf{A}_2^e - \mathbf{A}_1^e) + ik\mathbf{n}_s\,(\epsilon_1\Phi_1^e - \epsilon_2\Phi_2^e) \tag{3.37}$$

$$D = \mathbf{n}_s\cdot[\epsilon_1\,(ik\mathbf{A}_1^e - \nabla_s\Phi_1^e) - \epsilon_2\,(ik\mathbf{A}_2^e - \nabla_s\Phi_2^e)] \tag{3.38}$$

which depend only on the external source terms and not the surface distributions. These equations represent the continuity of the parallel component of the vector potential A and the scalar potential Φ across the boundary. In this way this method is a form of extinction method [Toigo77, Mills75] and is exact.

In this work we discuss cylindrically symmetric structures. We therefore consider the Fourier transform of the set of equations **??** with respect to the azimuthal angel ϕ,

$$f(\mathbf{r}) = \sum_{m=0}^{\infty} f_m(\rho,z)e^{im\phi}. \tag{3.39}$$

Assuming a single valued function $z = \xi(\rho)$ describing the interface, as we will use here, the transform reduces the surface integrals to a discrete set of one dimensional integrals along the radius. This, combined with the dipole symmetry of the emitter ($m = 0, \pm 1$) simplifies the numerical problem.

To solve the coupled set of equations the interface is described by a grid, and the integral is then discretized according to

$$(f_m)_b = f_m(\rho_b, z(\rho_b)). \tag{3.40}$$

And the Green's operators are averaged around a area of the discretization to create a matrix formulation of the integrals:

$$(G_m)_{a,b} = 2\pi\int_{\delta S_b}\rho' d\rho'\sqrt{1+\left(\frac{dz}{d\rho}|_{\rho_b}\right)^2}\,G_m(\rho_a,\rho',|z_a-z'|) \tag{3.41}$$

where δS_b is a radius element around ρ_b. In this way the integral can be written as a matrix product

$$I_m(\rho_a) = (G_m)_{a,b} \cdot (f_m)_b. \tag{3.42}$$

Equations **??** are thus reduced to a set of linear equations

$$\begin{pmatrix} G_1 & -G_2 & 0 & 0 \\ 0 & 0 & G_1 & -G_2 \\ -ik\epsilon_1 \mathbf{n}_s G_1 & ik\epsilon_2 \mathbf{n}_s G_2 & H_1 & -H_2 \\ \epsilon_1 H_1 & -\epsilon_2 H_2 & -ik\epsilon_1 \mathbf{n}_s G_1 & ik\epsilon_2 \mathbf{n}_s G_2 \end{pmatrix} \begin{pmatrix} \sigma_1 \\ \sigma_2 \\ \mathbf{h}_1 \\ \mathbf{h}_2 \end{pmatrix} = \begin{pmatrix} \Phi^e \\ \mathbf{A}^e \\ \boldsymbol{\alpha} \\ D \end{pmatrix}, \tag{3.43}$$

where we define $H_i \equiv (\mathbf{n}_s \cdot \nabla) G_i$, $\Phi^e \equiv \Phi_2^e - \Phi_1^e$, $\mathbf{A}^e \equiv \mathbf{A}_2^e - \mathbf{A}_1^e$ and both G_i and H_i are to be understood as the discrete matrices of size $N \times N$ and $3N \times 3N$ respectively, with N the size of the grid.

A major restriction applies here. The surface element δS_b is small compared to the smallest length scale of the problem. In our case, this is the penetration depth in the metal, on the order of $20nm$ in silver at vacuum wavelength of $\lambda_0 = 1\mu m$. For a comparable size and above, the resulting calculation exhibits no plasmons, and reconstruct the results of the perfectly conducting conductor, as no correlations can evolve in the metal. This results in fine grids when calculating structures of comparable with the wavelength as we do here. This made the calculations slow, requiring parallel computation of the Green function matrices.

The solution for the surface charge and current distributions is obtained by inverting the Green's function matrix on the righthand side of Eq. (3.43). Note, that the Green's matrices contain the surface information, while the source terms vector (LHS in (3.43) contain the information on the dipole position. Thus, though the calculations of the Green's matrix is complicated, once obtained it can be used for multiple dipole position, speeding up the calculations.

3.5 Concentric Bragg grating for plasmon-radiation coupling

In this section we investigate the effectiveness with which the plasmon can be coupled out of the metallic surface, in a directional manner by a Bragg grating. We show that up to 70% of the energy coupled to the plasmon on a flat surface can be directed into a cone of angle 0.6 rad in the bulk, equivalent to a numerical aperture (NA) 0.6 perpendicular to the surface of the lens. Compared to previous suggestion for efficient collection of the emission of a quantum emitter [Lee11a], requiring cumbersome oil immersed lens to achieve NA of 1.6, this allows for simpler experimental setup. Furthermore, the introduction of the grating introduces a cavity effect, enhancing the Purcell factor of the plasmonic channel.

As previously mentioned, on a flat surface the momentum of the SPP is higher than that of propagating waves in the dielectric above the mirror.

However, the introduction of a periodic structure enables the bridging of this momentum gap[López-Tejeira07] by process of Bragg scattering. to understand this we recall that light is scatters from a periodical structure according to

$$k_{||}^{(out)} = k_{||}^{(in)} \pm mG, \tag{3.44}$$

where $k_{||}^{in}, k_{||}^{out}$ are the in plane momenta components of the incoming and outgoing light, respectively. Here, $G = 2\pi/a$ is the reciprocal lattice vector of the grating of periodicity a. Thus by choosing the periodicity of the grating to equal the plasmon wavelength $G = k_{spp}$ the momentum in plane of the scattered light will be $k_{\|} = 0$. This means the emitted light will be radiated perpendicular to the surface. We use this to achieve radiation into a narrow cone around the axis of symmetry of the structure.

The geometry considered here is plotted in Fig. (3.6). For the investigation of the effect of the Bragg grating on the coupling efficiency between the SPP and radiation, no central hole is introduced since we wish to focus on the effect of the grating. In comparison of grating fields and flux, the dipole source is positioned at $d = 0.25/k_0$ away from the mirror on its axis of symmetry. This position was shown in section 3.2 to induce the maximal coupling to the mirror $\Gamma_{spp}/\Gamma_{tot} = 0.52$ and will serve as a reference to the performance of the coupler grating. The parameters investigated are radius of the cavity to the first groove (L in Fig. (3.6)) and the grating height (A). Due to computational power available, dependence on the grating periodicity is not investigated and is fixed at $G = 2\pi/\lambda_{spp}$, for the reason mentioned above. Unless mentioned, the total lens size of all grating considered is $90/k_0$, equivalent to 15 grooves. For the dielectric constants of Ag and the $GaAs$ considered throughout this chapter, this the length of the lens is much smaller than propagation length of the plasmon. This means that in some simulations part of the generated plasmon may reach the sample edge, disturbing the results of the calculation. This effect of scattering from the sample edge is considered below.

In Fig 3.7 and 3.8, we plot the radiated power into a solid angle as a function of the angle from the axis of symmetry. The power plotted is normalized to the calculated total decay rate of the emitter. Compared to the flat mirror, the introduction of the grating induces a peak in the emitted flux around the the central axis. The energy radiated shows strong dependence on both grating height and start position.

3.5.1 Radiative beaming of plasmon- groove height dependence

In this section we investigate the influence of the grating height on the efficiency of collection and the directionality of the emitted beam from the lens. Examining Fig. (3.8), the waist of the radiated cone is seems to be roughly inversely proportional to the height of the grating. This can be understood to reflect the conversion efficiency of the grating. As the effective area radiating the lens becomes larger the focal beam waist becomes narrower. The focusing effect thus depend on the effective distance traveled by the plasmon before being converted to radiation. The

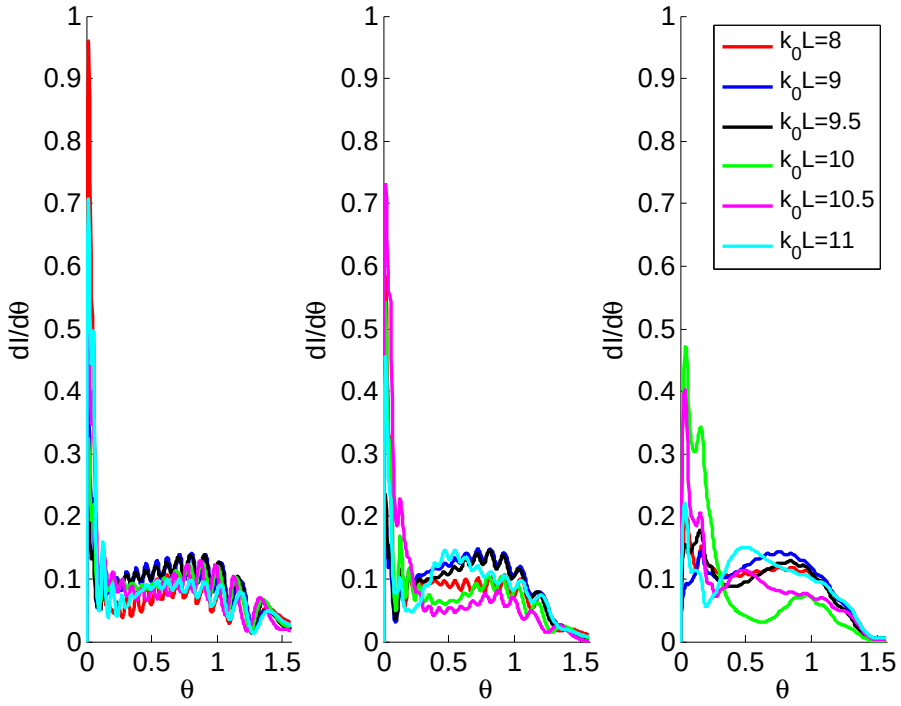

Figure 3.7: Fraction of the energy radiated into a solid angle about θ as a function of the angle for a parallel dipole positioned $h = 0.5/k_0$ from the Lens. Three different grating depths (a) $A = 0.4/k_0$, (a) $A = 0.8/k_0$, and (c) $A = 1.2/k_0$ are plotted. The radiation is normalized by the total decay rate. The different curves are for different starting positions of the grating L, as described in the text.

plasmon coupling to light can be seen as radiation damping increasing the imaginary part of the plasmon wavenumber.

To better understand this effects, we consider the electromagnetic fields on the surface of the lens. As was discussed for the flat mirror, the surface fields can be expanded in a polar Bessel-Fourier decomposition, similar to Eq.3.2. The Bessel Fourier decomposition of the z-component of the field, E_z, is presented in Fig 3.9. As expected from the radiation pattern discussed above, the directed emission appears as response around $k_{||} = 0$.

Also evident in Fig. (3.7) is that width of the plasmon peak is increased for increasing grating height. A zoom in on the broadening of the plasmon resonance compared to the flat mirror response function is plotted in Fig.(3.10). The broadening indicates an increase of the imaginary part of the plasmon wave number by a factor of ten. The variation between different grid starting points however prevents clearly distinguishing the effect of the grating heights on the width of the momentum distribution and we will evaluate the outcoupling strength using a different method below.

The introduction of the grating also changes the center of the plasmon resonance. As the wave number of the plasmon is changed, the plasmon wave number and the grating wave number are no longer exactly matched, which also contributes to the broadening of the radiated beam.

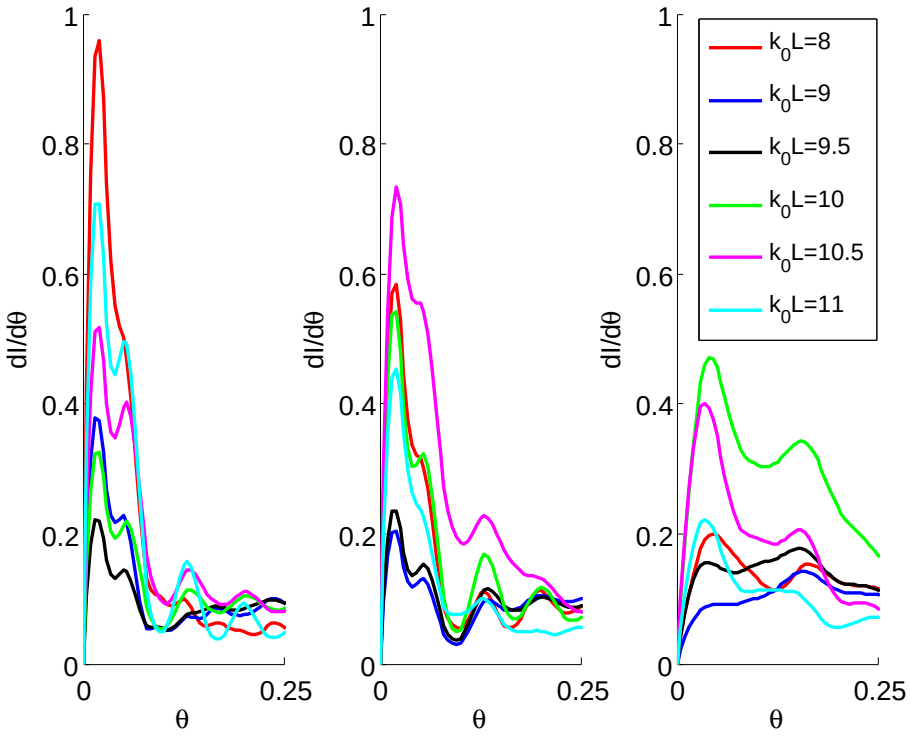

Figure 3.8: Same plot as Fig .3.7 around the axis of the lens. As the grating become shallow, the waist of the focused beam is reduced as the effective size of the lens increases.

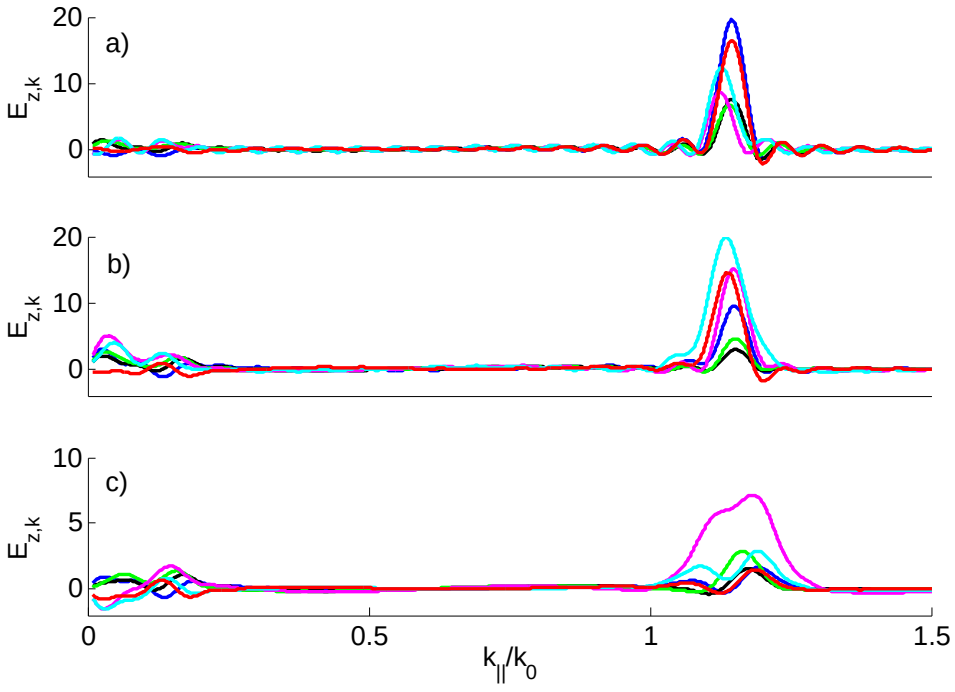

Figure 3.9: Bessel decomposition of the z component of the electric field on the surface. Both an increase in the k 0 components due to radiation and broadening of the plasmon resonance are visible.

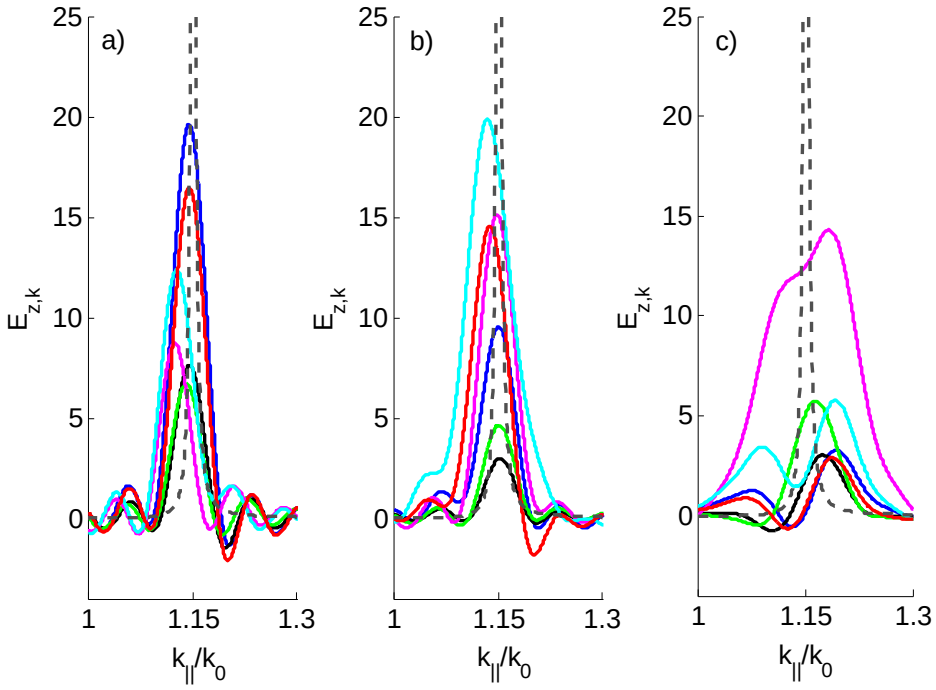

Figure 3.10: Same as 3.9 in the vicinity of the plasmon resonance. The black dashed line corresponds to the flat mirror case.

We have chosen $G = k_{spp}$ to isolate the k_{spp} component of the momentum transfer to the outcoupled directed beam. We are thus assuming that the grating is shallow enough so as not to shift the plasmon significantly from the flat surface wave number. From Fig. (3.10) we see that this assumption is justified for grating depth of $0.4/k_0$ and $0.8/k_0$. For deeper grating, as evident from the momentum distribution of grating depth $1.2/k_0$ further optimization of the grating frequency are to be made to improve the outcoupling efficiency.

To evaluate increase in the imaginary part of the plasmon wave number, we examine the in plane energy flux defined by the radial component of the Poynting vector

$$\mathbf{S} \cdot \hat{\rho} = \frac{c}{8\pi}(\mathbf{E} \times \mathbf{H}^*) \cdot \rho. \tag{3.45}$$

As we expect the plasmon to propagated outwards as a radial field, the flux is expected to be proportional to $S_\rho \propto \exp -i\tilde{k}/\rho$, with $\tilde{k}$ the effective propagation constant accounting also for the radiative losses. The flux is plotted in Fig. (3.11) on a logarithmic scale, after multiplying by the radius ρ. The modified decay lengths can be extracted and are $L_{0.4} = 220/k_0, L_{0.8} = 115/k_0$ and $L_{1.2} = 60/k_0$ for the grating height of $A = 0.4/k_0, A = 0.8/k_0$ and $A = 1.2/k_0$ respectively. The long propagation lengths also explain the features appearing in Fig(3.7) for the radiation patterns of the for the two shallower gratings, $A = 0.4/k_0$ and $A = 0.8/k_0$. As the length of the sample is smaller than the modified decay length (considering also that the relevant length is that of the grating, $\sim 80/k_0$), scattering from the sample edge results in diffraction fringes. A comparison with the expected $\propto J_0^2(k_0 R \sin\theta)$ behavior for Fraunhofer diffraction is shown to roughly match the observed behavior,

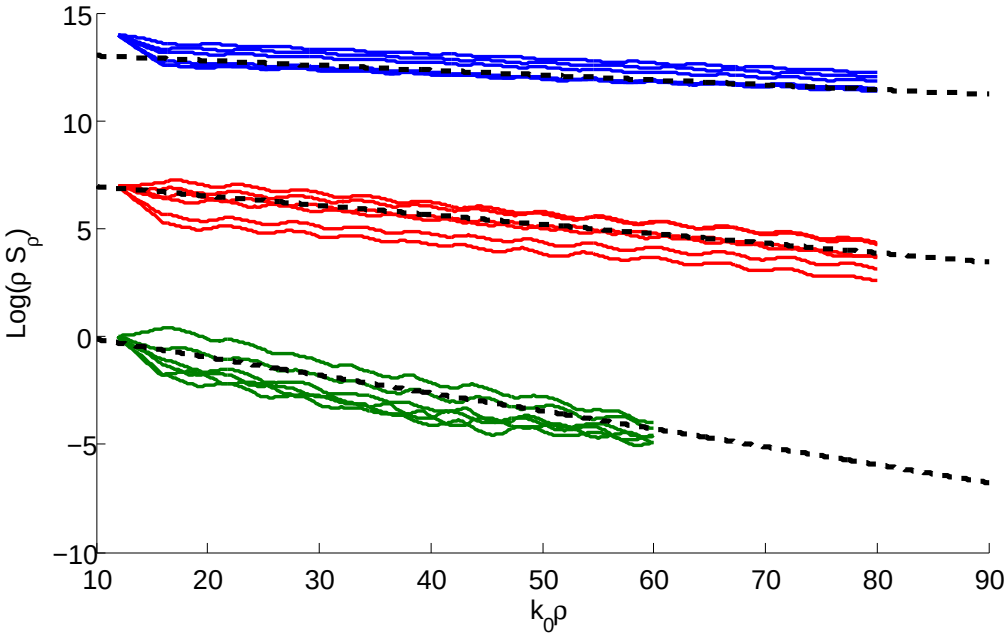

Figure 3.11: logarithm of the radial flux on the surface of the grating $A = 0.4/k_0, A = 0.8/k_0$ and $A = 1.2/k_0$. The depth of the grating determines the effective propagation constants by the efficiency of conversion.

see Fig.(3.12). To further validate this assumption, a calculation was done on a larger sample and the comparison is plotted in Fig.(3.12)

As we have seen, the depth of the grating is thus an important parameter in the design of these future device. The choice of the grid height is a compromise between the focusing of the beam and the size of the lens.

3.5.2 In plane scattering and plasmon cavity

Apart from the out of plane scattering, the introduction of the grating also generates backscattering on the surface from the boundary of the flat and grated surface. As the circular area around the dipole position is confined, the reflected plasmon can interfere with the outgoing plasmon to create a standing wave, significantly increasing the field amplitude at the origin [Liu05, Yanai09], and thereby also increases the decay into the plasmonic channel. The enhancing effect of in-plane scattering in focusing the plasmon to a single point was suggested by several authors [Zhang10, Steele06]. The theoretical analysis[Leskova85] of this is often quite cumbersome, and relys on technique such as impedance boundary conditions[Ong93] which are less suitable for the current solid state applications where the dielectric contrast between the metal and the dielectric is relatively low.Several experimental and simulative works have suggested strong field enhancement around the resonance condition [Yanai09, Carretero-Palacios11] $L = m\lambda_{spp}/2$ with m an integer number. Here we examine the decay rate into the plasmonic channel to give further evidence for the SPP source of the focusing.

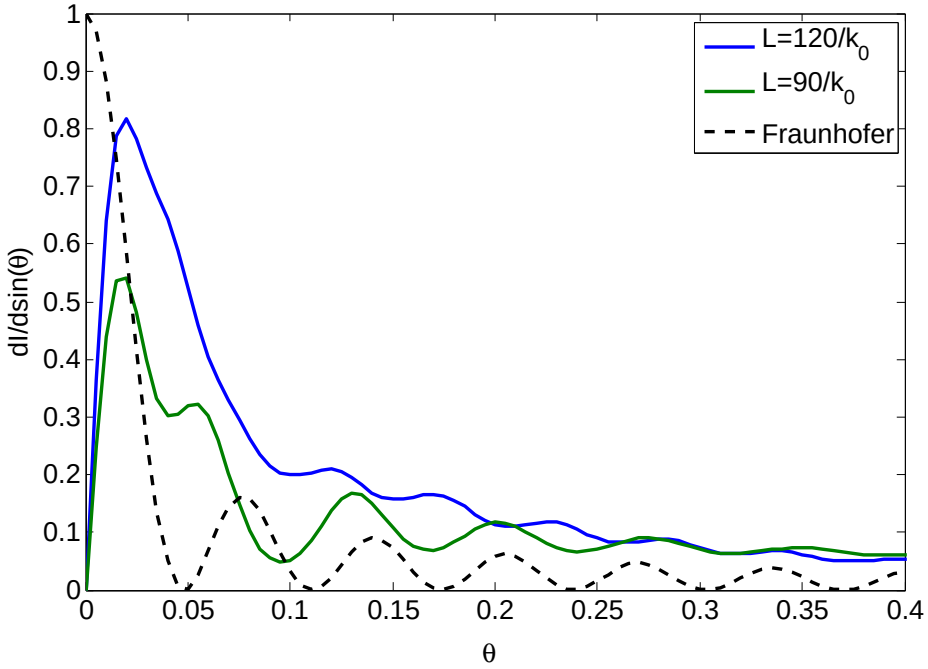

Figure 3.12: Comparison of Radiation patterns for $A = 0.8/k_0, L = 10/k_0$ plotted for two different sample size. As the decay length of the plasmon on the grating is longer than $90/k_0$, collection efficiency is not saturated for the shorter sample, and diffraction from the edges is evident.

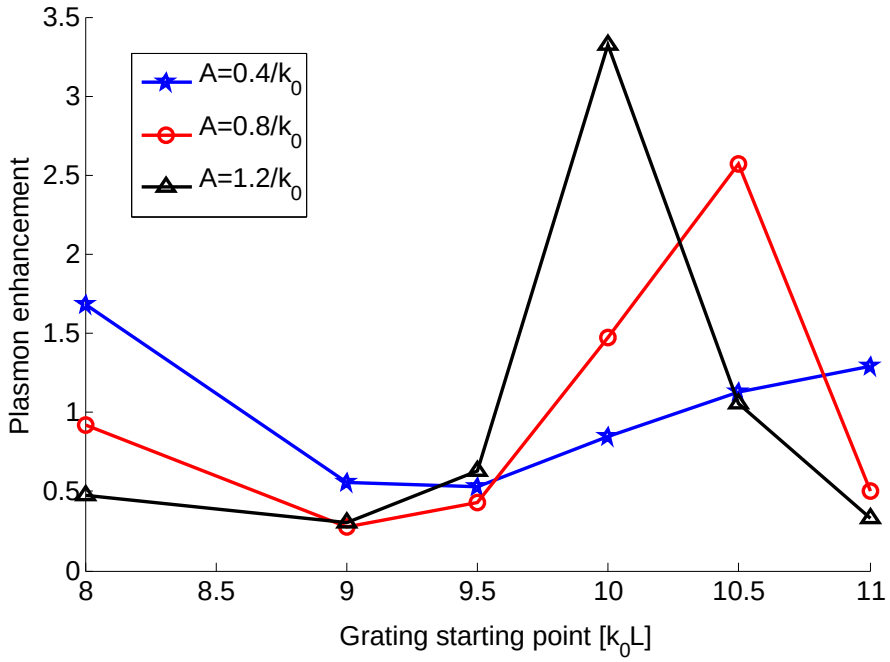

Figure 3.13: Enhancement of the plasmon decay rate as a function of the starting position of the grating L in 3.6.

The analysis of the plasmonic enhancement is enabled by the following assumptions. Since the non radiative decay rate is short range and the grating is engraved more than a plasmon wave length away, we assume this decay rate is not changed from the infinite mirror. This assumption can be supported be examining the decay rates above the mirror for $k_0 h < 0.1$ where the dominant decay channel is non radiative. Because of the distance of the grating starting point to the the dipole position, direct reflections from the mirror (the radiative part of the decay rate), should only differ for grazing angles, determined by $\tan(\theta) = d/L$, with d the dipole distance from the surface and L the initial radius of the grating. It thus has little influence on the on axes field and therefore on the field at the dipole position. This is also corroborated by examining the angular radiation pattern for larger d, where the plasmon excitation rate is small. For example, considering $k_0 d = 3$ the plasmonic energy fraction $\Gamma_{spp}/\Gamma_{total} = 0.037$ and both the radiation pattern and the decay rates agree for all grating parameters considered. As the analytical model of the infinite mirror allows isolation of the different contribution to the decay rate, these assumptions facilitate analyzing the enhancement of the plasmonic decay rate due to the cavity effect by subtracting the infinite mirror decay rates for the non radiative and radiative contributions, assuming that they are unaltered. The remaining decay rates show exponential behavior of the decay rate as a function of the dipole position, further justifying the assumptions made above.

The enhancement of the plasmon coupling due to the cavity effect as a function of the cavity size is plotted in Fig. (3.13), and the maximal fraction of energy directed into the plasmonic channel is plotted in Fig. (3.14). A significant increase of the decay rate occurs around $L = 2\lambda_{spp}$ though it is dependent on the grating depth suggesting a phase dependence of the reflection coefficient.

The addition of the grating thus improves both problem introduced in utilizing the flat surface plasmon for coupling to single emitters. The directional emission allows collection of the plasmon excitation by adding a lens of NA 0.6 above the surface, while the introduction of the cavity improves the Purcell factor of the plasmonic channel. The efficiency of collection into the cone of 0.2 radian above the mirror can now be calculated relative to the coupling to the plasmon, and is plotted in Fig. (3.15). We observed that the outcoupling efficiency is up to 70% of the plasmon energy.

3.6 Enhancing the coupling for an in plane dipole moment

Due to the limited coupling of the in-plane dipole, the structure considered above, with only a flat surface and gratings is not immediately suitable for implementation with quantum dot. In a conventionally fabricated layered structures quantum dot the dipole moment lies in the plane of the mirror. In this work, a central hole under the position of the quantum dot is suggested, allowing for the formation of a local cavity to form, increasing the coupling efficiency to the parallel dipole. The introduc-

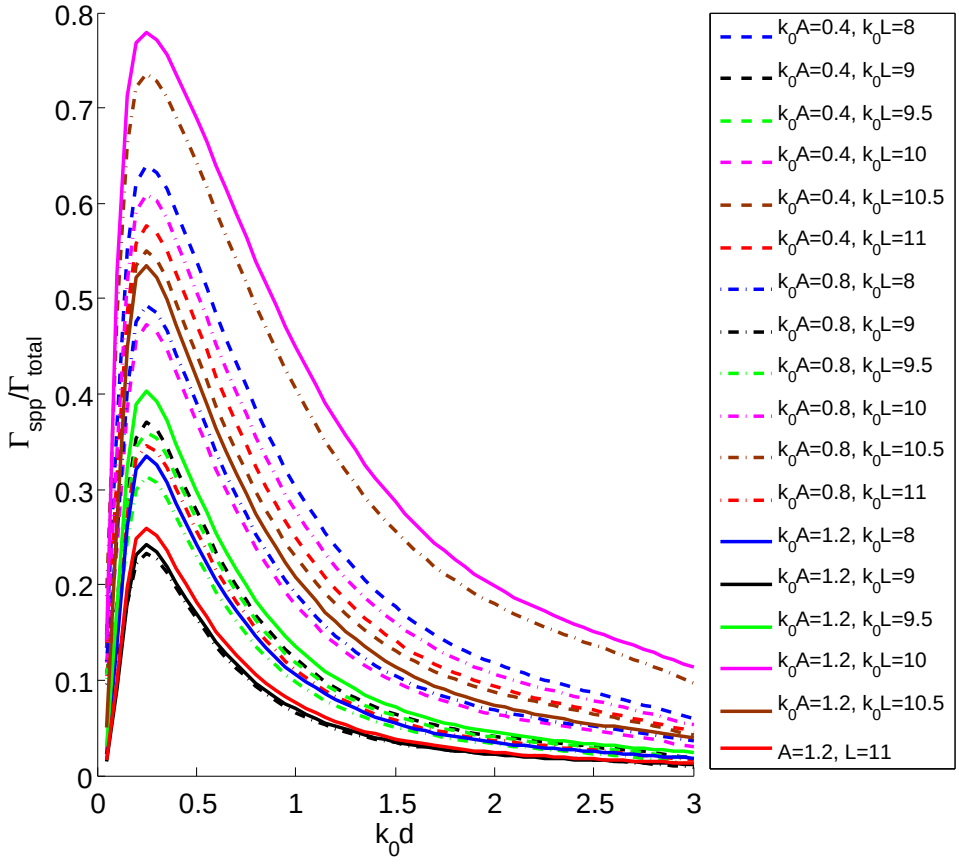

Figure 3.14: Fraction of the energy coupled to the plasmonic channel for different cavity lengths. Solid line -$A = 1.2/k_0$, dot-dashed-$A = 0.8/k_0$ and dashed $A = 0.4/k_0$.

tion of the hole is motivated by the appearance of a dipole charge and field distribution [Popov05] suggesting better matching with the dipole orientation.

The question of the fields arising at the opening of small slits and holes in metallic films was investigated seriously in the research of extra ordinary transmission (EOT) effect [Garcia-Vidal10b]. In this field, the excitation of surface plasmons by an incoming is partially responsible for the enhanced transmission through holes in metallic films. However, in these works relative weak coupling of the incoming light to SPPs have been observed, mostly through tunneling. Furthermore, rigorous analysis was preform mostly for one dimensional slits, where a guided plasmonic mode occurs for infinitely small gaps.

In this section the coupling of the single emitter to the central hole and the subsequent excitation of SPP along the surface of the lens is investigated. The decay rates, plotted in Fig.(3.16), show two distinct regimes of enhancement depending on the central hole parameters. We show an increase in the decay rate of a factor $\Gamma/\Gamma_0 = 25$ for narrow holes due to the increase in surface charge at the hole edges. For wide holes, coupling to the modes of the hole allows further increase in the decay rate up to

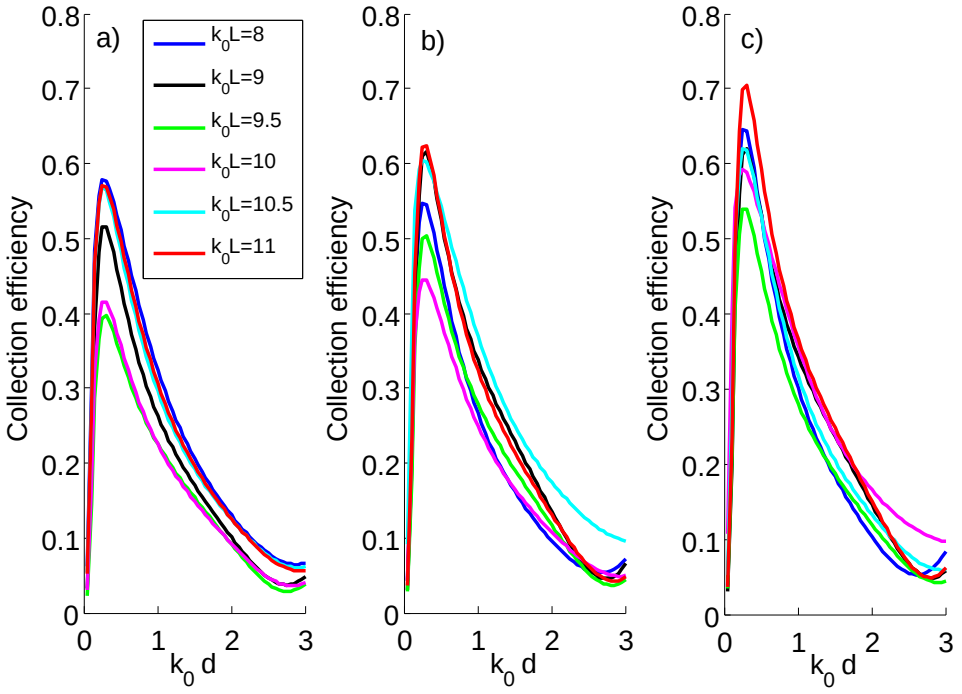

Figure 3.15: Fraction of the plasmon energy radiated into the $0.6NA$ cone above the lens for different grating depths.

$\Gamma/\Gamma_0 = 45$ for deeper holes as is shown in 3.6.2. The coupling between these modes and the SPP is discussed 3.6.3, where an inferred coupling to the plasmonic mode of about 70% of the emitted energy is found.

3.6.1 Optimization of Central Pit geometry

For the numerical simulations of the central hole, the groove is taken to be symmetric and the cylindrical groove is modeled

$$\zeta(\rho) = -\frac{H}{2}\left(\tanh(\frac{\Delta}{2}(\rho - R)) - 1\right). \tag{3.46}$$

Here, A is the hole's depth and w is the radius. The wall steepness $1/\Delta$ is taken to be on the order of the flat surface numerical step, and the resolution in ρ is taken to be such that the length element along the wall is at least the flat surface resolution. As there is no analytical expression for the decay rate as in the case of the flat mirror, the plasmon fraction cannot be investigated directly from the surface response in a simple way. Instead, the pit plasmonic efficiency investigation is done with the concentric Bragg grating discussed in 3.5, and the efficiency of plasmon collection is defined by the energy radiated into a solid angle equivalent to $0.6NA$. The two sets of results shown here are based on calculations with grating of depth $0.8k_0R$ and a starting position of $10k_0R$. The plasmonic coupling efficiency is then inferred from the coupling efficiencies of the grating. As discussed in the previous section, the starting position

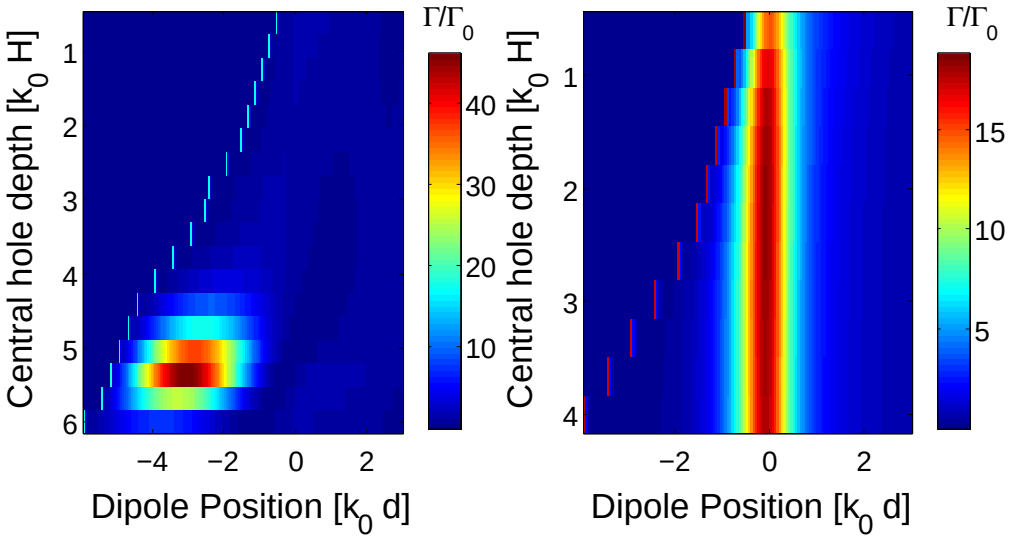

Figure 3.16: Decay rate of the dipole emitter as a function the central hole radius, dependent on the dipole position on the axis of symmetry of the lens. The two plots demonstrate the two different regimes discussed in the text. In $a)$ the central hole radius $w = 1.4/k_0$ allows for a cavity mode in the deep hole regime. For $w = 0.6/k_0$, plotted in $b)$ no such mode is excited, and the coupling to the mirror is through the electrostatic charge on the edge. See text for details.

3.6.2 Coupling of the emitter to the surface

To understand the enhancement observed, we investigate two mechanism allowing for an increase of coupling between the single emitter and the surface.

Shallow limit- shape resonants

In Fig. (3.17) the maximal decay rate normalized to the free space dipole decay rate is plotted as function of the hole parameters. The range of parameters plotted here roughly corresponds to the regime accessible in experiments [Lezec02], where R $(0.4 - 1.6/k_0)$ corresponds to $20 - 100nm$ in a $GaAs$ structure, for the vacuum wavelength of $\lambda_0 = 1\mu m$. The dipole decay rate is seen to be primarily dependent on the hole radius, and insensitive to the groove depth. In Fig. (3.18) we plot the decay rate as a function of the dipole position on the symmetry axis of the lens, noting that the maximal decay enhancement is obtained when the dipole is positioned close to the the groove edge, and reduces as the dipole is further inserted into the hole. Note also that the decay rate curves are also altered when the dipole is positioned outside the groove as compared to the dependence of the decay rate on the position for the flat mirror.

The origin of the enhanced decay rate exhibited in this regime of parameters can be understood as the result of the high electric charge induced on the edge of the hole, and is thus independent of the depth of the etched hole. To validate this assumption, we plot in Fig. (3.19a) the charge dis-

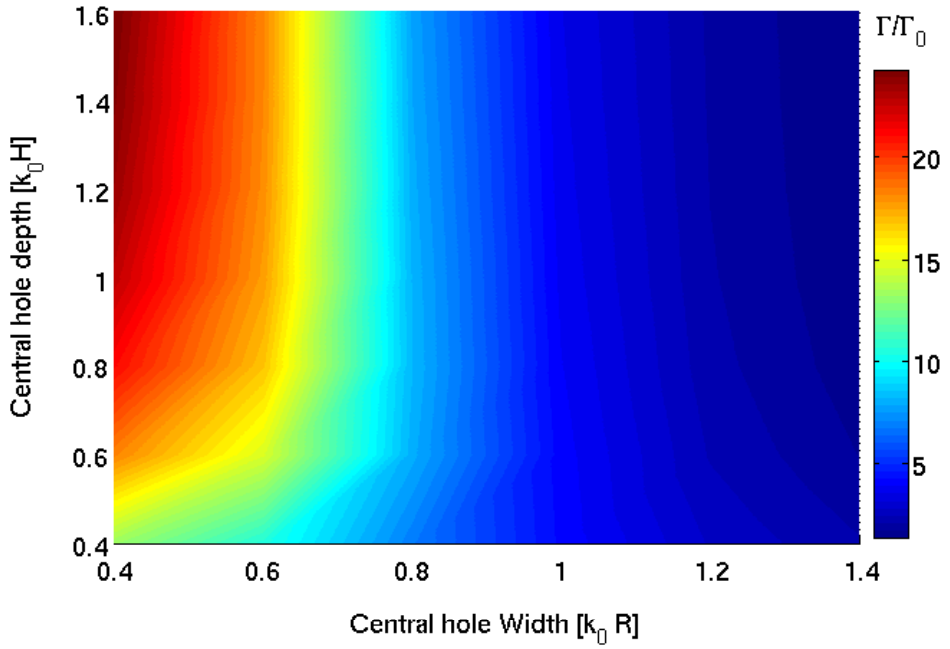

Figure 3.17: The maximal decay rates of an dipolar emitter placed on the lens axis as a function of the the central hole parameters for typical experimental parameters. As discussed in the text, in this shallow pit limit there is no excitation of the wave guide mode, and the decay rates are determined by the proximity to the hole edges.

tribution induced by the dipole on the surface of the lens for the different parameters appearing in Fig. (3.17). These can be seen to be almost unchanged as the hole is deepened.

Such bounded surface plasma excitations are called localized surface plasmons (LSP) [Boardman82]. LSP frequency can be determined in a non-retarded (electrostatic) approximation by solving the classical Dirichlet problem. One feature of such localized excitation is a polynomial decay of the charge distribution away from the localization area. This can be seen by considering for example a corner in a perfectly conducting metal. In the electrostatic limit, the problem reduces to the finding the electric potential solving the Laplace equation,

$$\frac{1}{\sin\theta}\frac{d}{d\theta}\left(\sin\theta\frac{dP}{d\theta}\right)+\left[l(l+1)-\frac{1}{\sin^2\theta}\right]P=0 \tag{3.47}$$

$$\frac{d^2}{d\rho^2}R-\frac{l(l+1)}{\rho^2}R=0, \tag{3.48}$$

where separation of variables $\Phi = R(\rho)P(\theta)e^{\pm im\phi}$ has been used and we have taken $m = \pm 1$ which is the relevant choice in our case given the source symmetry. We are interested in the functional behavior of the surface charges in the vicinity of the edge, on the outer part of the lens. To further simplify the analysis we consider only one corner and further reduce the problem to a tip of a cone of opening angle $\alpha = \pi/4$, to which the solution for the surface charge in proximity to the edge is proportional

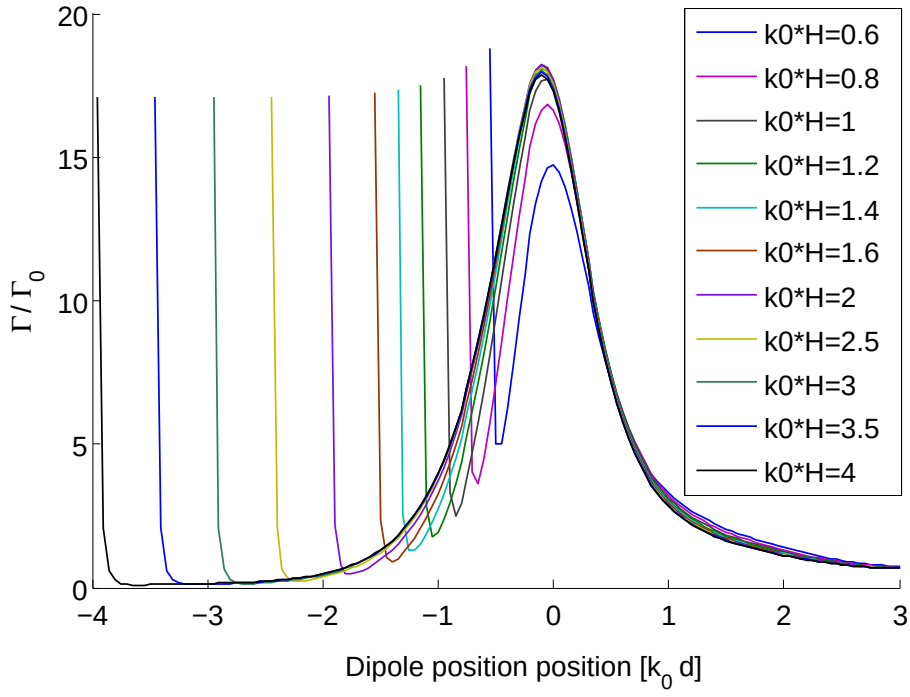

Figure 3.18: Decay rates as a function of the position of the dipole into the hole, for hole radius $w = 0.6/k_0$. Maximal rates are obtained in the same position on the edge of the hole, regardless of the geometry of the hole.

to

$$R \propto \rho^{\nu-1}, \tag{3.49}$$

where ν is determined by the boundary values such that

$$P_\nu\left(\cos(\pi/4)\right) = 0, \tag{3.50}$$

for a corner of $\pi/2$. This leads to a polynomial decay of the charge on the surface, where $\rho^{-0.7}$ expected for an corner of $\pi/2$.

In Fig. (3.19b) the log-log plot of the charge distribution is plotted as a function of the distance from the hole edge for the different depths of the hole. Though the power of the decay deviates from the estimated one, a clear polynomial decay of identical order is visible for all the central hole depth, indicating that the origin of the decay enhancement is that of a localized excitation at the central holes edge.

Deep pit limit - Wave guide mode

As the central hole depth is further increased, another coupling mechanism kicks in. In Fig. (3.16) the decay rate enhancement for deeper depth holes is plotted for two different radii, $R = 0.6/k_0$ and $R = 1.4/k_0$. As discussed in the previous section, for the small radius hole the dipole decay rate enhancement is primarily due to edge charges and is achieved in the vicinity of the hole edge with little dependence on the hole depth. For

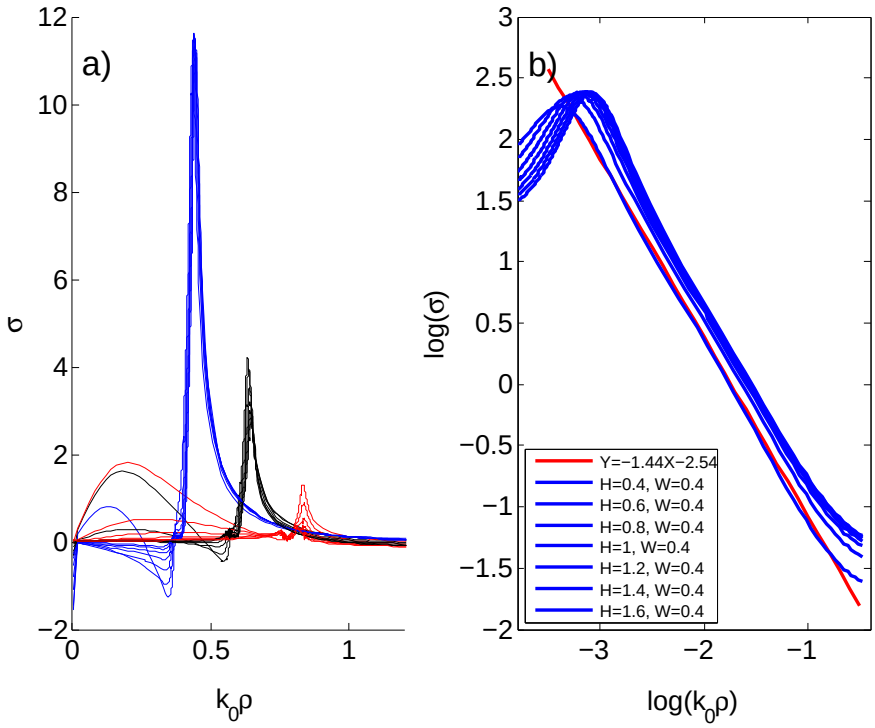

Figure 3.19: Charge distribution on the hole edge, with the dipole positioned at $k_0 h = -0.1$. Different hole radii are indicated by different colors. $W = 0.4/k_0$ are plotted in red, $W = 0.6/k_0$ in blue and $W = 0.8/k_0$ in black for central hole depth in the range appearing in Fig.3.17. In panel (b), the logarithm of the charge distribution is plotted as a function of the logarithm of distance to the hole edge for $W = 0.4/k_0$

$R = 1.4/k_0$ however we observe a strong enhancement of the decay rate appearing around $H = 5.2/k_0$. The enhancement observed, with a decay rate of about 45 times that of the free space decay rate, is significantly larger than the one generated by the electrostatic edge charges, and is maximized inside the hole.

To understand the appearance of this resonant coupling of the dipole to the central hole, let us first examine the infinitely long dielectric nanowire surrounded by metal. The dispersion relation of the infinite dielectric cylinder surrounded by metallic material of finite conductivity is determined by [Novotny94, Catrysse05]:

$$\left[\frac{k_1}{k_{\perp,1}}\frac{J'_m}{J_m} - \frac{k_2}{k_{\perp,2}}\frac{H'_m}{H_m}\right]\left[\frac{1}{k_{\perp,1}}\frac{J'_m}{J_m} - \frac{1}{k_{\perp,2}}\frac{H'_m}{H_m}\right] = \frac{m^2 k_\parallel}{R^2}\left(\frac{1}{k^2_{\perp,1}} - \frac{1}{k^2_{\perp,2}}\right)^2 \tag{3.51}$$

where J_m, H_m are the m-order Bessel and Hankel functions of the argument $k_{\perp,i}R$ with

$$k_{\perp,i} = \sqrt{k_0^2 \epsilon_i - k_\parallel^2}\,, \qquad i = 1,2 \tag{3.52}$$

Here prime denotes differentiation with respect to the the function argument. With the exception of the m=0 modes, modes of this waveguide

can not be separated into TM or TE mode and these modes are noted as HE (EH) if the the electric (magnetic) field is the dominant component in the direction of propagation. It was already noted [Novotny94] that the lowest mode of such waveguide in the finite conductivity case is the HE_{11} mode, which does not display a cutoff but rather has a smooth transition to an evanescent mode. As the radius of the core is decreased, the wave number in the propagation direction continuously decreases while the imaginary part of the wave number increases. As the radius is further reduced, the imaginary part of the transverse wave number is increased, indicating larger fraction of the energy deposited in the metal and thus higher losses. In Fig. (3.20), the dispersion curve around the transition point of the HE_{11} mode is plotted. At radii $R < 3.4/k_0$, the cutoff radius for the HE_{12} mode, considered here the waveguide is a single mode channel, as any higher modes are display a cutoff. Note that the hole always supports propagating mode, far below $\lambda_0/2$ at which the perfect electric conductor (PEC) waveguide displays a cutoff. This is a unique result of the finite conductivity of the surrounding metal which is not taken into account in coupled mode models [Carretero-Palacios11]. The modal shape of the HE_{11} also proves favorable for coupling to a dipole perpendicular to the axis of symmetry of the wire. The mode function electric fields are given by [Snyder83]

$$\mathbf{E}_\rho = -\frac{a_- J_0(k_{\perp,1}\rho) + a_+ J_2(k_{\perp,1}\rho)}{J_1(k_{\perp,1}R)} \cos(\phi) \tag{3.53}$$

$$\mathbf{E}_\phi = \frac{a_- J_0(k_{\perp,1}\rho) - a_+ J_2(k_{\perp,1}\rho)}{J_1(k_{\perp,1}R)} \sin(\phi) \tag{3.54}$$

$$\mathbf{E}_z = -\frac{ik_{\perp,1}}{k_z} \frac{J_1(k_{\perp,1}\rho)}{J_1(k_{\perp,1}R)} \cos(\phi), \tag{3.55}$$

with

$$a_\pm = \frac{1}{2}\left(\frac{1}{R}\left(\frac{1}{k_{\perp,2}^2} - \frac{1}{k_{\perp,1}^2}\right) \frac{1}{\frac{1}{k_{\perp,1}}\frac{J_m'}{J_m} - \frac{1}{k_{\perp,2}}\frac{H_m'}{H_m}} \pm 1\right). \tag{3.56}$$

This mode has a non vanishing x electric field component

$$E_x \propto a_- / J_1(k_{\perp,1}R), \tag{3.57}$$

allowing the coupling to the on axis dipole. The dispersion curve allows tailoring of the coupling of the dipole to the mode. In Fig. (3.16) the decay rate of the emitter is plotted for two different pit radii, namely $k_0R = 0.6$ and $k_0R = 1.4$. As expected from the dispersion curve, below the transition point the hole depth plays very little influence on the decay rate pattern since the coupling to the propagating mode is weak, and the decay rate is mainly determined by the proximity to the sharp edges of the pit, as discussed for the shallow limit case (3.6.2). However, for the for width $k_0R > 1.1$ plotted in Fig. (3.16a), the coupling to the propagating mode is enabled beyond $k_0L > 1/2$. Here the optimal coupling position is determined by the waveguide mode. When the depth of the pit is equal to the $\lambda_{wg}/2$ the formation of a standing wave in the hole is obtained and the decay rates are maximal. We note here the discrepancy with experiments conducted [Miyazaki06, Kurokawa07] on a two dimensional

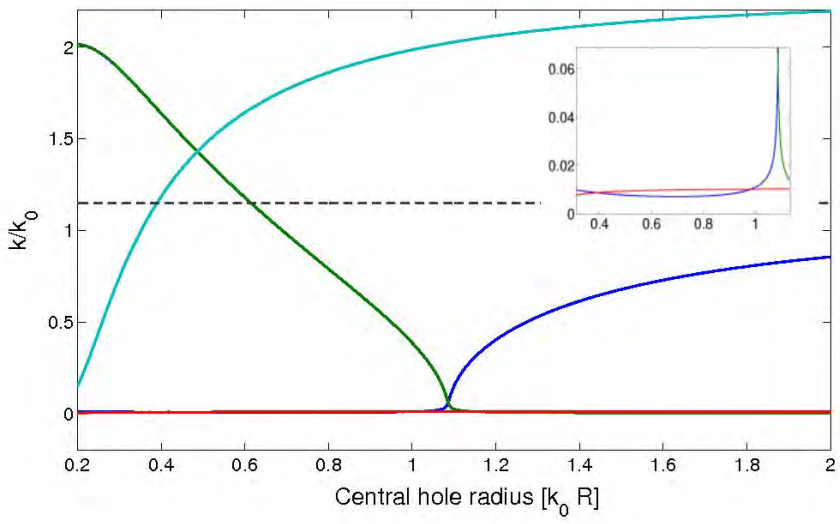

Figure 3.20: Dispersion curves for the HE_{11} mode in the central hole in the deep hole limit. In blue and green the real $\Re\{k_z\}$ and imaginary $\Re\{k_z\}$ parts of the wavenumber in the direction of the axis of symmetry, respectively. In .

Metal-Insulator-Metal (MIM) slit structure. In these experiments with one end closed slit, the coupling to the resonances appeared at depths of odd multiplication of the guided wave length. In those experiments, the resonances are investigated by illumination of the slit from the outside external. The resonance is then constrained to have a maximum of the perpendicular electric field at the slit entrance, in order to couple to it. Here the radiation source is internal in the pit, and so enhanced coupling to the standing wave can occur in different position independent of the field amplitude at the open end.

3.6.3 Directional radiation and collection efficiency with a central pit

In Sec. (3.6.2) we observed enhanced coupling of the dipole emitter to the surface, when introducing a hole on the axis of symmetry beneath the emitter position. This enhanced coupling was expressed by rapid decay rate relative to the free space decay rate of the emitter. We have identified two decay channels associated with modes localized at the central hole. For our purpose it is important however to consider the coupling of these modes to the propagating surface plasmons, and subsequently to directional radiation by means of the coupling grating as we discussed in Sec. (3.5).

Though the decay rates are significantly increased when coupling to the edge or waveguide modes, neither of these modes is phased matched to the surface plasmon propagating on the surface. In Fig. (3.21), normalized decay rates into the cone of $0.6NA$, above the surface, associated with plasmonic fraction of the energy reaching the grating, are plotted for the parameter range of the shallow pit. The coupling to the plasmon

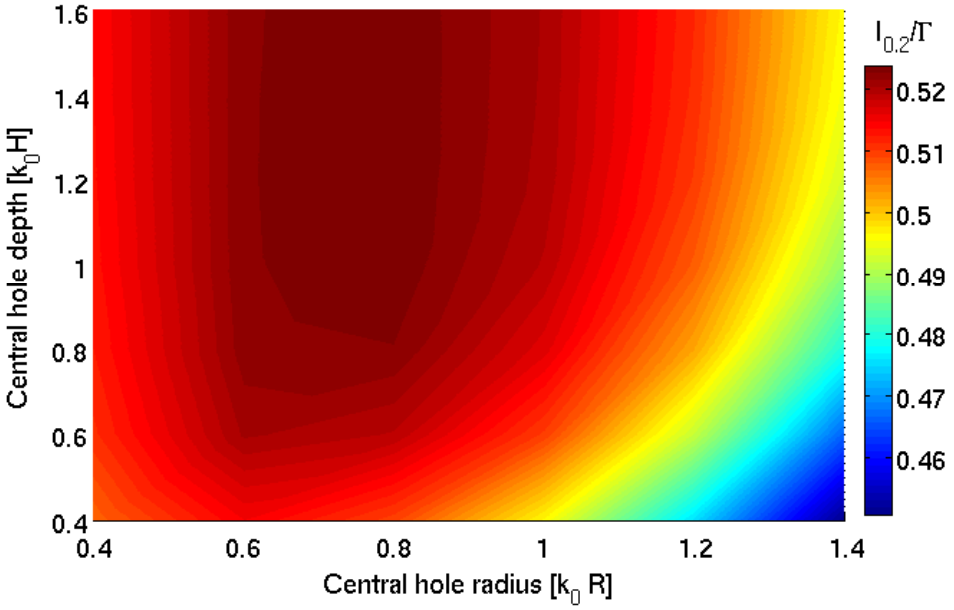

Figure 3.21: Fraction of the total energy emitted by the dipole radiated into an angle of 0.6 NA about the symmetry axis of the lens, for the shallow central hole regime.

is seen to be constant at around 50% of the dipole energy. The same limit is observed in the deep limit plotted in Fig. (3.22). Another distinct feature is the appearance of a dip in the radiated power. This illustrates the claim made in the previous subsection. When the enhancement due to the standing wave in the hole is such that the field amplitude at the open end is small, the coupling to the surface modes outside the hole is inhibited, resulting in radiation from the grating. These results are in agreement with the two dimensional results of [Lalanne05] where diffraction from the edge of the hole into evanescent modes was accounted for the weak coupling. Even with the limited collection efficiency, enhanced decay rate can be beneficial for solid state applications as other decohering processes in the semiconductor can be suppressed.

3.7 Conclusions

To conclude, we have shown that a plasmonic lens, constructed of a planar metallic surface with concentric grooves, and a central hole can serve as an effective coupler to a single dipole emitter placed on the axis of symmetry. The system in mind for this design, already used for investigating plasmonic and photonic interaction with single emitters, is that of self-assembled InGaAs quantum dots [Andersen10]. We have optimized the grating height showing coupling efficiencies of 70% of the dipole emission can be directed into a cone of NA 0.6 above the surface, facilitating simple experimental collection. This is achieved using a cavity effect generated by the in plane scattering at the grating edge, which we show to

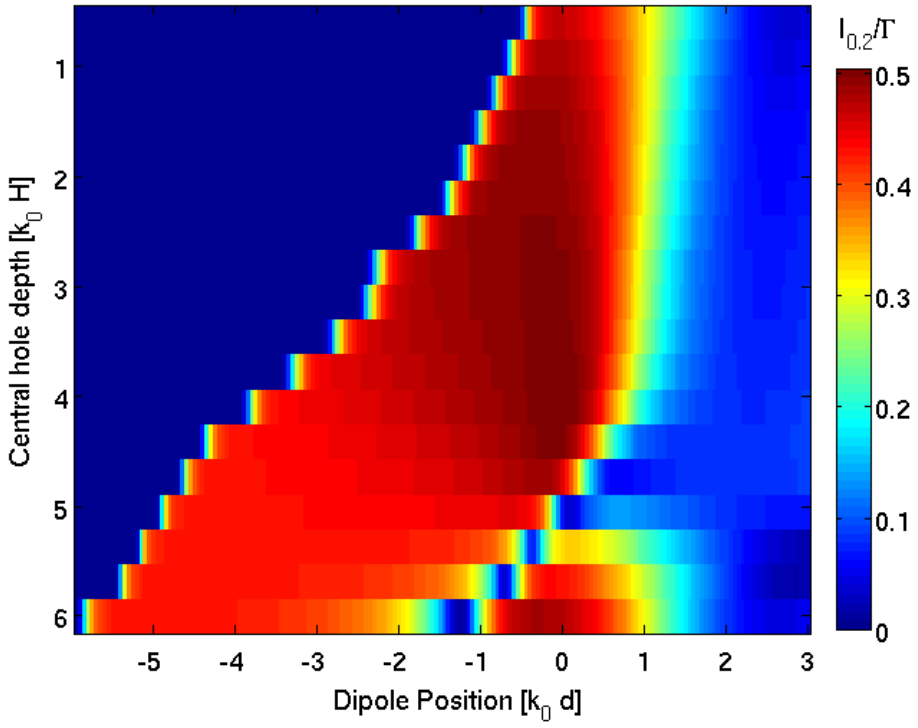

Figure 3.22: Fraction of the total energy emitted by the dipole radiated into an angle of 0.6 NA about the symmetry axis of the lens in the regime of the deep central hole.

increase the coupling to the plasmonic decay channel by a factor of three. To further improve the coupling to quantum dots having their dipole moment aligned along the surface, we have introduced a cylindrical groove on the symmetry axis beneath the quantum dot. We have analyzed the effect for two regimes of the holes depth and dipole position. We showed coupling to shape resonances on the hole edge for shallow grooves, resulting in increase of the emitter's total decay rate by a factor of 25. A stronger coupling to the guided HE_11 mode in the hole was observed for deep grooves, with an increase of the total decay rate by a factor of 45. However, both coupling mechanisms seem to detuned from the surface plasmon mode, and therefore a limited extraction rate via the grating coupler of about 50% was obtained. These results suggest the plasmonic lens can become a valuable tool in interacting with quantum dots, bypassing the need for lossy waveguide structures.

Part II

Breakdown of classical physics

Chapter 4

Non classicality criterion for conjugated variable of a single degree of freedom

4.1 Introduction

In this chapter we provide a conceptually simple demonstration of one of the key discrepancies between classical and quantum mechanics, valid for systems of a single degree of freedom: classical systems can always be described by a joint probability distribution for x and p, the two canonically conjugated coordinates of a system, whereas such a description does not apply in quantum mechanics due to the Heisenberg uncertainty principle. This discrepancy is most evident when the phase space description of the state of a system is examined. Classically, the phase space distribution $W(x_i, p_i)$ is the joint probability of finding the system in an infinitesimal area around $x = x_i, p = p_i$, and hence it obeys all the requirements of a probability distribution including being a non-negative function. As mentioned, in the case of a quantum phase space formulation, introduced by Wigner [Mandel95], the Heisenberg uncertainty renders this definition meaningless, as a joint probability distribution for x and p does not exist. The phase space distribution is only defined through the single coordinate (marginal) distributions, projected from the distribution function [Nha08] and this relaxation of constraints allows for negative values of the function in areas smaller than $\hbar$. This negativity is not directly observable due to the vacuum fluctuations preventing simultaneous measurement of x and p. However, one can still infer the phase space distribution from measurements of only a single observable at a time and detect such negativities, thereby illuminating the failure of classical theory.

The usage of these negativities as markers of non-classicality has been discussed and demonstrated in several quantum optics systems (see, e.g., [Leibfried96, Lvovsky01, Zavatta04, Ourjoumtsev06, Mari11]), using tomographic techniques. Often such methods search for the quantum state most compatible with the experimental data using statistical inference or variational techniques[Hradil97, Benichi11] and thus inherently rely on quantum mechanics. These methods are therefore not applicable for demonstrating the absence of a classical description. Alternatively, given

measurements of all the coordinate distributions, the underlying state can be uniquely determined, and the phase space distribution fully calculated using the inverse Radon transformation [Welsch99] without relying on quantum mechanics. Though such methods have been used in quantum optics for demonstrating various states, the mathematical transformation involved is highly complicated. Furthermore the numerical stability of the inverse transformation is problematic, leading to numerical uncertainty at high frequencies, and sometimes results in unphysical states [Lvovsky09]. These limitations are a drawback for using tomographic techniques for validating the breakdown of a classical description, and the application of these methods is usually cumbersome.

Our simple, unambiguous demonstration of the absence of a classical probability distribution is based on recent theoretical work by Bednorz and Belzig [Bednorz11] that verifies the negativity of the Wigner function based on moments. As discussed in detail below, their results lead to a hierarchy of inequalities, such that violation of any one inequality indicates negativity of the Wigner function. Full tomographic reconstruction with the associated numerical complexities is thereby avoided. We extend this approach such that it can be applied to quadrature measurement of a single photon state, and use the experimental data from the heralded single photon generation to directly disprove the existence of a joint probability of the position and momentum for this system.

4.2 Probing phase space indirectly

We start by re-iterating the key results of Bednorz and Belzig, through a reformulation that relies only on classical mechanics. The phase space of a system with a single degree of freedom is fully characterized by a two-dimensional phase space distribution $W(x,p)$. That is, given the phase space distribution, the ensemble averaged result of any measurable quantity A can be obtained by

$$\langle A \rangle = \int dxdp\, W(x,p)\, A(x,p)\,, \tag{4.1}$$

where $A(x,p)$ is the decomposition of the quantity A in terms of the generalized coordinate x and its canonically conjugated momentum p.

To disprove the existence of a classical probability distribution we examine the ensemble average of a non-negative test function $\mathfrak{F}(x,p)$ over a classically explainable system, which must have a proper distribution function that results in the ensemble average of $\mathfrak{F}$ be non-negative:

$$\langle \mathfrak{F} \rangle = \int dxdp\, W(x,p)\, \mathfrak{F}(x,p) \geq 0. \tag{4.2}$$

Violating this condition is a direct proof of the absence of a joint probability distribution. The condition can, however, be violated in quantum mechanics, where $W(x,p)$ is the Wigner function that can contain negative values. The objective therefore is to optimize a test function such that it will be dominant at the possible negative areas of the distribution function. For a rotationally invariant phase space both the phase space

distribution and the test function can be described solely by the phase space radius r, defined by $r^2 = x^2 + p^2$. For reasons to become clear later, we choose a specific form for the test function $\mathfrak{F}$, writing it as a square of an Nth order, even polynomial M with real coefficients $\{C_i\}_N$;

$$\langle \mathfrak{F} \rangle = \langle M^2 \rangle = \left\langle \left(1 + \sum_{n=1}^{N/2} C_{2n} r^{2n} \right)^2 \right\rangle . \tag{4.3}$$

Minimizing the above expression for a given order N is done by straightforward linear optimization of the coefficients $\{C_i\}_N$:

$$\sum_{l=1}^{N/2} \langle r^{2(l+j)} \rangle C_{2l} = -\langle r^{2j} \rangle, \tag{4.4}$$

for all $j = 1, 2, ..., N/2$. Notice that the linearity of the problem ensures that the obtained minimum of $\langle \mathfrak{F} \rangle$ is global and therefore the most optimal indicator of a possible violation of Eq. (4.2) for a given polynomial order N. It is important to emphasize that this is only a sufficient criterion for non-classicality, and an optimized positive average for a chosen N does not ensure a classical probability distribution, since the negativity may only be exhibited by the inclusion of higher order terms in M. However, it is clear that increasing the polynomial order N cannot increase the minimized value of $\langle \mathfrak{F} \rangle$, and we conjecture that the limit of $N \to \infty$ will exhibit any negativity of the Wigner function, as the polynomial can represent an arbitrarily (analytical) sharp peaked function $\mathfrak{F}$ focused at the negativity. Assuming the existence of all moments (e.g., due to an exponentially decaying tail of the phase space distribution at large r), this then becomes a necessary criterion for the negativity of the distribution function. We also note here, that similar polynomial expansion has been discussed [Shchukin04, Korbicz05] in the context of the P-function distribution. The P-function is, however, only defined within the framework of quantum mechanics, and hence cannot be used to prove the absence of a classical description.

It is also here that the natural connection to photon antibunching arises. If the Hamiltonian is that of the harmonic oscillator, r^2 is directly related to the intensity, and the above relation can be expressed in terms of coherence functions. For example, when considering the second order polynomial $M = 1 + C_2 r^2$, the optimal test function is found to be such for which $C_2 = -\langle r^2 \rangle / \langle r^4 \rangle$ and the negativity criterion is then

$$\frac{\langle r^2 \rangle^2}{\langle r^4 \rangle} > 1. \tag{4.5}$$

Replacing $I = r^2$ immediately yields $g^{(2)} < 1$, the antibunching criterion.

We assume that, as is the case for many systems, the system in question can only be experimentally accessed by measuring one of the canonically conjugated variables (e.g., x or p) at a time. Since we are restricted to single coordinate measurement at a time, neither the intensity nor the phase space distribution function is directly accessible. For this method to be applicable to such experimental data, the functional $\langle \mathfrak{F} \rangle$ must be

expressed in terms of the moments of the projected coordinates $\langle Q_\alpha^n \rangle$, where

$$Q_\alpha = \cos\alpha\, x + \sin\alpha\, p,\ P_\alpha = \cos\alpha\, x - \sin\alpha\, p \tag{4.6}$$

is a measureable rotated coordinate. To do this we use the identity

$$\left(x^2+p^2\right)^N = A_{2N} \sum_{m=1}^{2N} \left(\cos\left(\frac{m\pi}{2N}\right) x + \sin\left(\frac{m\pi}{2N}\right) p\right)^{2N}, \tag{4.7}$$

where

$$A_{2N} = \begin{pmatrix} 2N \\ N \end{pmatrix}^{-1} \frac{2^{2N}}{2N}. \tag{4.8}$$

This is where quantum and classical approaches diverge. While classically Eq. (4.7) represents a measurable physical quantity, it is missing the key vacuum uncertainty, allowing for the breakdown of the classical description.

It is interesting to note the implication of identity (4.7). For the $2m$th moment of the radial distribution to be known, we need $2m$ 'cuts' in phase space; i.e., different coordinate measurements at equally distributed angles. Regardless of any assumption about the underlying state, the average of Eq. (4.7) directly gives

$$\langle r^{2N} \rangle = A_{2N} \sum_{m=1}^{2N} \left\langle \left(Q_{m\pi/2N}\right)^{2N} \right\rangle. \tag{4.9}$$

In the special case of a symmetric distribution function these moments are all identical, and Eq. (4.9) reduces to

$$\langle r^{2N} \rangle = \begin{pmatrix} 2N \\ N \end{pmatrix}^{-1} 2^{2N} \langle x^{2N} \rangle. \tag{4.10}$$

The radial moments can thus be indirectly calculated from the quadrature measurements. Substituting these radial moments into Eq. (4.2) using the functional form of $\mathfrak{F}(x,p)$ given by Eq. (4.3), we get, for a given set of measured moments $\{\langle x^{2k} \rangle\}_k$, a necessary condition for classicality of the underlying state. If Eq. (4.2) is violated by the solutions of Eq. (4.4), the underlying state cannot be explained by a proper phase space probability distribution, and one cannot assign a joint probability distribution to x and p.

4.3 Experimental verification

To demonstrate the absence of a joint probability distribution we are going to consider the phase space description of a single photon state. In phase space this can be described by the first excited state of a harmonic oscillator, which is rotationally invariant and contain negative parts in the Wigner functions. Fig. 4.1 shows the optimal functional forms obtained for the this state for low polynomial orders. As higher order terms are included, the optimized test function is increasingly probing the negative

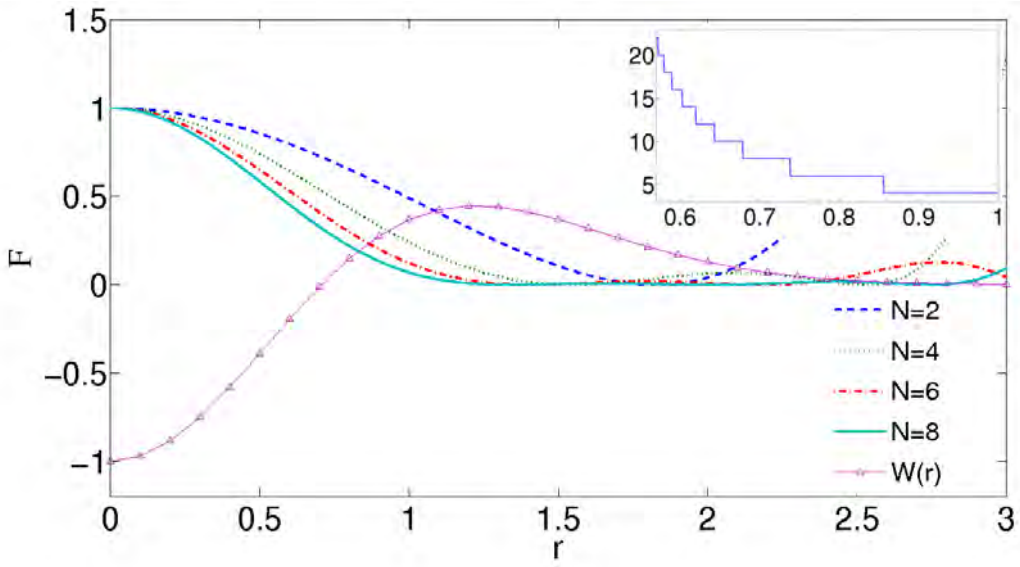

Figure 4.1: Profiles of the test function $\mathfrak{F}$ minimizing the expectation value $\langle\mathfrak{F}\rangle$ for the first excited state of a quantum harmonic oscillator, as a function of the phase space radius, for different orders N (see text) plotted against the profile of the corresponding Wigner function. As the order of the polynomial increases, the function becomes centered around the negativity, decreasing elsewhere. In this case, negative expectation values are obtained starting at $N = 4$. Inset shows the polynomial order required to observe negative expectation values, as a function of the single-photon fractional content in a mixture with vacuum. As the fraction of vacuum is increased, the state approaches a classically describable state and higher moments are needed to observe the negativity.

part of W, yielding a negative expectation value. We note that negative expectation values appear only from the fourth order onward. This is because the peak of the test function at the position of the negativity must be narrower than Heisenberg's uncertainty in order not to smear the negativity; this is in full agreement with Ref. [Bednorz11].

The experimental demonstration is achieved with single photons generated by an heralded cavity-enhanced non-degenerate parametric down-conversion. The equivalence between a single mode electromagnetic field and an harmonic oscillator allows us to describe the EM field by a phase space of a single degree of freedom. The down-conversion process produces two photons, and as one is detected as a trigger, the result is a single photon state where the losses introduce a statistically mixed component of vacuum. The projection measurements (quadratures) are obtained by measuring the statistics of the noise, using an optical homodyne detection scheme. In this scheme, the weak investigated optical field is overlapped with a strong laser pulse on a beam splitter, and the interference of the two fields is detected and subtracted. The phase of the strong laser field determines the angle α (Eq. (4.6)) of the measured coordinate. Measurements were taken without fixing the phase of the local oscillator, thus smearing the resulting distribution. This enables us to treat the results as rotationally invariant even if non-invariant features existed prior to smearing. Such measurements will generate a rotationally invariant re-

constructed state for any underlying state, but this does not necessarily average out negativities in the Wigner function (see, e.g., [Leonhardt05]). For details of the experimental setup and the charactarization of the resulting single photon see Ref. [Neergaard-Nielsen07].

The data set contained 180,000 measured quadratures. We have here revised the optimization of the functional to also account for statistical uncertainties inherent to a limited data set. This is done by optimizing

$$G = \frac{\langle \mathfrak{F} \rangle}{\langle \sigma_{\mathfrak{F}} \rangle}, \tag{4.11}$$

where $\sigma_{\mathfrak{F}} = \sqrt{\langle \mathfrak{F}^2 \rangle - \langle \mathfrak{F} \rangle^2}$ is the standard deviation of $\mathfrak{F}$. The results are shown in Fig. 4.2. The fact that the expectation value for our test function is negative with certainty of almost twenty standard deviations, clearly demonstrates that the measured state in this experiment cannot be explained by classical theory, unambiguously negating the possibility of existence of a joint probability distribution for x and p. The appearance of negative values from the twelfth order polynomials and higher indicate the quantum mechanical description of this state in terms of a Wigner function includes negative valued areas. We note that the minimized function from Eq. (4.3) is monotonically decreasing for increasing order N, and the onset of negativity at a certain order therefore means that all higher orders will also be negative. This suggests a sequential authentication procedure for an unknown state. As mentioned above, for a pure single photon state, negative expectation values are observable from the 4-th order polynomial onwards. The twelfth order polynomial required here is due to the vacuum component of the field, requiring higher orders of the polynomial as shown in the inset of Fig. 4.2, and is in agreement with the results obtained in Ref. [Neergaard-Nielsen07] reporting 62% fraction of single photon in the resulting mixed state.

4.4 Conclusions

In conclusion, we have experimentally demonstrated the non-existence of a joint probability distribution of two canonical variables. This is done by violation of an inequality derived without the assumptions of quantum mechanics, thus allowing for it as proof of the absence of a classical description in systems not immediately evident to display quantum behavior. The procedure used here can thus provide a simple, practical tool for demonstrating the non-classicality of a state based on quadrature measurements, where the existence of a classical joint distribution of two conjugated variables can be negated. In this way, this procedure is closely linked to other criteria [Leggett85, Klyachko08, Lapkiewicz11] demonstrating contextuality of measurements, and thus disproving the classical local hidden variable view. Unlike Ref. [Leggett85, Klyachko08, Lapkiewicz11], which are applicable to discrete variables, the method demonstrated here applies for continuous variables such as position and momentum, collective spin operators [Fernholz08] and quadrature phase operators. This makes it useful to systems containing many particles, where criteria based on counting particles are not easily implemented

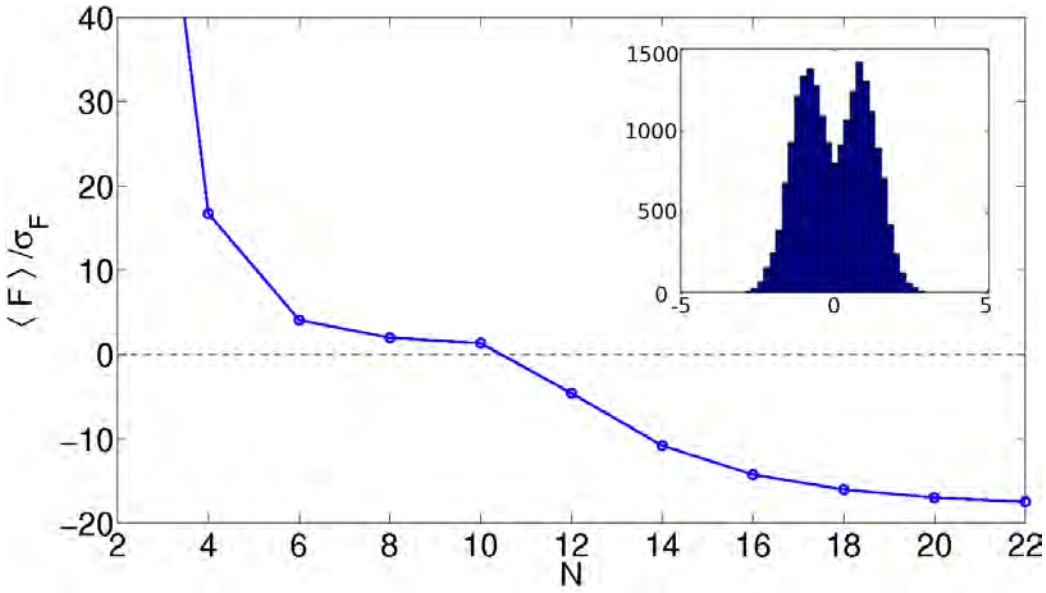

Figure 4.2: Expectation value for the square of a polynomial relative to its standard deviation, as a function of the polynomial's order for the experimental data. Negativity by almost 20 standard deviations disproves the existence of a joint probability distribution for x and p. The inset shows a histogram of the raw measured quadrature data (arbitrary units).

and interpreted. This method complements the full tomographic reconstruction techniques in that it is simpler and avoids numerical complexities of inverse transformations. These kinds of conceptual proofs, when extended to different detection schemes, can shed more light on the quantum to classical correspondence, especially where the control of claimed macroscopic quantum states is in question.

Part III

Appendices

Appendix A

Boundary Elements Method for an axially symmetric interface

A.1 Boundary Element Method

In this Appendix we describe in detail the approximations applied to solve numerically the problem of a dipole above a corrugated metallic surface with cylindrical symmetry. We used the Boundary Element Method [García de Abajo02], and we provide a review of this method, along with the specific details of our current implementation.

Writing the macroscopic Maxwell equations in the frequency domain

$$\nabla \cdot (\epsilon \mathbf{E}) = 4\pi\rho, \qquad \nabla \cdot (\mu \mathbf{H}) = 0$$
$$\nabla \times \mathbf{E} - \frac{ik}{\mu}\mathbf{H} = 0, \qquad \nabla \times \mathbf{H} + ik\epsilon\mathbf{E} = \frac{4\pi\mathbf{j}}{c}$$

with ϵ and μ being the dielectric constant and magnetic permeability, respectively, and $k = \omega/c$. These equations can be written in terms of the vector and scalar potentials A and Φ

$$\left(\nabla^2 + i\mu\epsilon k^2\right) A = -\frac{4\pi}{c}\left(\mu j + m\right) \tag{A.1}$$
$$\left(\nabla^2 + i\mu\epsilon k^2\right) \Phi = -4\pi\left(\frac{\rho}{\epsilon} + \sigma_s\right) \tag{A.2}$$

where a Laurentz-like gauge was used, $\nabla \cdot A = i\mu\epsilon k\Phi$. The additional source term represent spatial variation of the material properties ϵ, μ:

$$\sigma_s = \frac{1}{4\pi}\left(\epsilon E\right) \cdot \nabla\frac{1}{\epsilon} \tag{A.3}$$
$$m = -\frac{c}{4\pi}\left(ik\Phi\nabla\left(\epsilon\mu\right) + H \times \nabla\mu\right). \tag{A.4}$$

In this work, we consider non magnetic materials, setting $\mu = 1$ everywhere. We shall also focus on sharp interfaces between homogeneous material. In this case the additional sources represent surface charges and currents on the interface between the two materials, mediating the effect of the fields on one side of the interface to the other. Led by this understanding, the core idea of the boundary elements method is that introduction of fictitious boundary charges and currents, determined by the

boundary conditions on the interface, enables one to calculate the fields on both side of the interface using the homogeneous material solution.

Namely, writing the solution to the potentials

$$\Phi(\mathbf{r})|_{\mathbf{r}\in V_i} = \frac{1}{\epsilon_i}\int d\mathbf{u} G_i(\mathbf{r},\mathbf{u})\rho(\mathbf{u}) + \int_{S_i} d\mathbf{s} G_i(\mathbf{r},\mathbf{s})\sigma_i(\mathbf{s}) \tag{A.5}$$

$$\mathbf{A}(\mathbf{r})|_{\mathbf{r}\in V_i} = \frac{1}{c}\int d\mathbf{u} G_i(\mathbf{r},\mathbf{u})\mathbf{j}(\mathbf{u}) + \int_{S_i} d\mathbf{s} G_i(\mathbf{r},\mathbf{s})\mathbf{h}_i(\mathbf{s}) \tag{A.6}$$

where the homogeneous Green's function is used

$$G_i(\mathbf{r},\mathbf{r}') = \frac{e^{ik_i|\mathbf{r}-\mathbf{r}'|}}{|\mathbf{r}-\mathbf{r}'|}, \tag{A.7}$$

$k_i = \sqrt{\epsilon_i}k$ being the wave number in the material, allows for calculation of the electromagnetic fields everywhere if the surface charge and current $\{\sigma, \mathbf{h}\}$ on both sides of the interface can be determined.

As $\mathbf{A}$ has three coordinates, Φ is a scalar, and both are to be calculated on both sides of the interface, Eq. (A.6) gives rise to eight component linear integral equations (for $\{\sigma, \mathbf{h}\}$):

$$\begin{aligned}\int d^2s G_1(\mathbf{s},\mathbf{s}')\,\sigma_1(\mathbf{s}') - \int d^2s G_2(\mathbf{s},\mathbf{s}')\,\sigma_2(\mathbf{s}') = \\ = \frac{1}{\epsilon_2}\int d^3r G_2(\mathbf{s},\mathbf{r})\,\rho_2(\mathbf{r}) - \frac{1}{\epsilon_1}\int d^3r G_1(\mathbf{s},\mathbf{r})\,\rho_1(\mathbf{r})\end{aligned} \tag{A.8}$$

$$\begin{aligned}\int d^2s G_1(\mathbf{s},\mathbf{s}')\,\mathbf{h}_1(\mathbf{s}') - \int d^2s G_2(\mathbf{s},\mathbf{s}')\,\mathbf{h}_2(\mathbf{s}') = \\ = \frac{1}{c}\int d^3r G_2(\mathbf{s},\mathbf{r})\,\mathbf{j}_2(\mathbf{r}) - \frac{1}{c}\int d^3r G_1(\mathbf{s},\mathbf{r})\,\mathbf{j}_1(\mathbf{r})\end{aligned} \tag{A.9}$$

$$\begin{aligned}\int d^2s\,(\mathbf{n}_s\cdot\nabla)\,G_1(\mathbf{s},\mathbf{s}')\,\mathbf{h}_1(\mathbf{s}') - \int d^2s\,(\mathbf{n}_s\cdot\nabla)\,G_2(\mathbf{s},\mathbf{s}')\,\mathbf{h}_2(\mathbf{s}') - \\ - ik\mathbf{n}_s\left(\epsilon_1\int d^2s G_1(\mathbf{s},\mathbf{s}')\,\sigma_1(\mathbf{s}') - \epsilon_2\int d^2s G_2(\mathbf{s},\mathbf{s}')\,\sigma_2(\mathbf{s}')\right) = \boldsymbol{\alpha}\end{aligned} \tag{A.10}$$

$$\begin{aligned}\epsilon_1\int d^2s\,(\mathbf{n}_s\cdot\nabla)\,G_1(\mathbf{s},\mathbf{s}')\,\sigma_1(\mathbf{s}') - \epsilon_2\int d^2s\,(\mathbf{n}_s\cdot\nabla)\,G_2(\mathbf{s},\mathbf{s}')\,\sigma_2(\mathbf{s}') - \\ - ik\mathbf{n}_s\left(\epsilon_1\int d^2s G_1(\mathbf{s},\mathbf{s}')\,\mathbf{h}_1(\mathbf{s}') - \epsilon_2\int d^2s G_2(\mathbf{s},\mathbf{s}')\,\mathbf{h}_2(\mathbf{s}')\right) = D\end{aligned} \tag{A.11}$$

The source terms in these equations are the volume integral containing the known real currents and charges distributions in the problem, and are described in Sec. (A.1.3). Note, that the volume integrals in the above equations can be calculated directly for the known charge and current distributions (we calculate the dipole source terms for the lens geometry in Sec. (**??**)) To solve these equations, the interface is discretized, to form a set of linear algebraic equation. In this work, the two dimensional surface integral are further reduced using the symmetry of the lens. We discuss this below.

A.1.1 Cylindrical coordinates

The cylindrical symmetry of the problem is used to reduce the surface integrals in Eqs. (**??**) to one dimensional integrals in the following manner. Any scalar quantity f can be decomposed in cylindrical coordinates into its angular Fourier components:

$$f = \sum_{m=0}^{\infty} f_m(\rho, z) e^{im\phi} \tag{A.12}$$

where

$$f_m = \frac{1}{2\pi} \int_0^{2\pi} d\phi \, f e^{-im\phi}, \tag{A.13}$$

and the integral of the Green's function:

$$I = \sum_m \int \rho' d\rho' d\phi' \sqrt{1 + (dz/d\rho)^2 \,|_{\rho'}} \, G(\rho, z, \phi, \rho', z', \phi') f_m(\rho', z') e^{im\phi'}. \tag{A.14}$$

The same decomposition can be applied to the Green's function. Using the symmetry of the angular dependence of the distance in cylindrical coordinates, where

$$\left|\mathbf{r} - \mathbf{r}'\right| = \sqrt{\rho^2 + \rho'^2 + (z - z')^2 - 2\rho\rho' \cos(\phi - \phi')}, \tag{A.15}$$

it is enough to use the single coordinate Fourier decomposition

$$G = \sum_m G_m e^{im(\phi - \phi')}, \qquad G_m = \frac{1}{2\pi} \int d\psi G e^{-im\psi}, \tag{A.16}$$

and we get

$$I = 2\pi \sum_m e^{im\phi} \int \rho' d\rho' \sqrt{1 + (dz/d\rho)^2 \,|_{\rho'}} \, G_m(\rho, \rho', |z - z'|) f_m(\rho', z'). \tag{A.17}$$

The same decomposition can be applied to the Green's function gradient

$$H = (\mathbf{n}_s \cdot \nabla) \, G \tag{A.18}$$

The gradient has a singularity at the origin, yet the integral can be shown to equal [García de Abajo02]

$$Hf = \int d^2 s \left[\frac{\mathbf{n}_s \cdot (\mathbf{s} - \mathbf{s}')}{|\mathbf{s} - \mathbf{s}'|^3} \left(ik|\mathbf{s} - \mathbf{s}'| - 1 \right) e^{ik|\mathbf{s} - \mathbf{s}'|} \pm 2\pi\delta(\mathbf{s} - \mathbf{s}') \right] f(\mathbf{s}'), \tag{A.19}$$

with the minus (plus) sign coresponding to the side of the interface $\mathbf{n}_s$ is pointing to (from). For the integral part of A.19 the angular decomposition is again defined as

$$H_m = \frac{1}{2\pi} \int d\psi \frac{\mathbf{n}_s \cdot (\mathbf{s} - \mathbf{s}')}{R^3} \left(ikR - 1 \right) e^{ikR} e^{-im\psi}, \tag{A.20}$$

where

$$R = \sqrt{\rho^2 + \rho'^2 + (z - z')^2 - 2\rho\rho' \cos(\phi - \phi')}. \tag{A.21}$$

Some care is needed preforming the above decomposition of the intergral into angular moments when vectorial field $\mathbf{f}$ are involved, as the cylindrical unit vectors are also functions of the angle ϕ. A detailed examples of the involved treatment appears in **??** below.

A.1.2 Discretization and numerical solution

In order to solve the set of linear integral equations **??** numerically,the integrals are discretised as following; The interface is described by a grid,

$$(f_m)_b = f_m(\rho_b, z(\rho_b)) \tag{A.22}$$

$$(G_m)_{a,b} = 2\pi \int_{\delta S_b} \rho' d\rho' \sqrt{1 + \left(\frac{dz}{d\rho}|_{\rho_b}\right)^2}\, G_m(\rho_a, \rho', |z_a - z'|) \tag{A.23}$$

where δS_b is a radius element around ρ_b. In this way the integral can be written as a matrix product

$$I_m(\rho_a) = (G_m)_{a,b} \cdot (f_m)_b \tag{A.24}$$

A.1.3 Source terms

Source terms are defined through the 4-vector potential for a dipole positioned above the symmetry axis of the lens, at $\mathbf{r}_p = (0, 0, d)$, described by a current density

$$\mathbf{j} = -i\omega \mathbf{p} \delta(\mathbf{r} - \mathbf{r}_p) \tag{A.25}$$

This gives

$$\begin{aligned}\mathbf{A}_1(\mathbf{s}) &= \frac{1}{c}\int d\mathbf{r}' \, \frac{e^{ik_1|\mathbf{r}'-\mathbf{s}|}}{|\mathbf{r}'-\mathbf{s}|}\mathbf{j}(\mathbf{r}') \\ &= -ik\mathbf{p}\int d\mathbf{r}' \, \frac{e^{ik_1|\mathbf{r}'-\mathbf{s}|}}{|\mathbf{r}'-\mathbf{s}|}\delta(\mathbf{r}-\mathbf{r}_p) = -ik\mathbf{p}\frac{e^{ik_1|\mathbf{r}_p-\mathbf{s}|}}{|\mathbf{r}_p-\mathbf{s}|}\end{aligned}$$

The angular Fourier components are then calculated as stated above:

$$A_1^m(\mathbf{s}) = \frac{1}{2\pi}\int_0^{2\pi} d\phi e^{-im\phi}\left[-ik\mathbf{p}\frac{e^{ik_1|\mathbf{r}_p-\mathbf{s}|}}{|\mathbf{r}_p-\mathbf{s}|}\right]$$

where $\mathfrak{D}$ is the distance function described above. Since the dipole is located at $\rho = 0$, the fraction in the integrand does depend on the angle *phi*. Assuming $\mathbf{p} = p_x\hat{x} + p_z\hat{z}$, and using $\hat{x} = \cos\phi\,\hat{\rho} - \sin\phi\,\hat{\phi}$, we get

$$\begin{aligned}A_1^m(\mathbf{s}) &= \frac{-ik}{2\pi}\frac{e^{ik_1|\mathbf{r}_p-\mathbf{s}|}}{|\mathbf{r}_p-\mathbf{s}|}\int_0^{2\pi} d\phi\, e^{-im\phi}\left[p_x\cos\phi\,\hat{\rho} - p_x\sin\phi\,\hat{\phi} + p_z\,\hat{z}\right] = \\ &= \frac{-ik}{2\pi}\frac{e^{ik_1|\mathbf{r}_p-\mathbf{s}|}}{|\mathbf{r}_p-\mathbf{s}|}\int_0^{2\pi} d\phi\, e^{-im\phi}\left[\frac{p_x}{2}\left(e^{i\phi}\left(\hat{\rho}+i\hat{\phi}\right) + e^{-i\phi}\left(\hat{\rho}-i\hat{\phi}\right)\right) + p_z\,\hat{z}\right] = \\ &= -ik\frac{e^{ik_1|\mathbf{r}_p-\mathbf{s}|}}{|\mathbf{r}_p-\mathbf{s}|}\left[\frac{p_x}{2}\left(\delta_{m,1}\left(\hat{\rho}+i\hat{\phi}\right) + \delta_{m,-1}\left(\hat{\rho}-i\hat{\phi}\right)\right) + p_z\delta_{m,0}\,\hat{z}\right]\end{aligned}$$

To calculate the charge density for the dipole, we look at the continuity equation

$$\nabla \mathbf{J} = -\frac{\partial \varrho}{\partial t} = i\omega\varrho \tag{A.26}$$

where time dependence of $e^{-i\omega t}$ is assumed for all quantities. Substituting the current density (A.25) leads to $\varrho = -\mathbf{p}\cdot\nabla_r\delta(\mathbf{r}-\mathbf{r}_p)$, and plugging this density into the potential expression yields after partial integration (note sign change):

$$\begin{aligned}
\Phi_1 &= \frac{1}{\epsilon_1}\int d\mathbf{r}'\,\delta(\mathbf{r}'-\mathbf{r}_p)\mathbf{p}\cdot\nabla_{\mathbf{r}'}\left(\frac{e^{ik_1|\mathbf{r}'-\mathbf{s}|}}{|\mathbf{r}'-\mathbf{s}|}\right) = \\
&= \frac{1}{\epsilon_1}\int d\mathbf{r}'\,\delta(\mathbf{r}'-\mathbf{r}_p)\frac{\mathbf{p}\cdot(\mathbf{r}'-\mathbf{s})}{|\mathbf{r}'-\mathbf{s}|^3}\left(ik_1|\mathbf{r}'-\mathbf{s}|-1\right)e^{ik_1|\mathbf{r}'-\mathbf{s}|} = \\
&= \frac{1}{\epsilon_1}\frac{\mathbf{p}\cdot(\mathbf{r}_p-\mathbf{s})}{|\mathbf{r}_p-\mathbf{s}|^3}\left(ik_1|\mathbf{r}_p-\mathbf{s}|-1\right)e^{ik_1|\mathbf{r}_p-\mathbf{s}|}
\end{aligned}$$

The angular Fourier components are calculated in a similar manner to the vector potential, noting that only $\mathbf{p}\cdot(\mathbf{r}'-\mathbf{s})$ depends on the angle of $\mathbf{s}$;

$$\begin{aligned}
\Phi_1^m &= \frac{1}{\epsilon_1}\frac{\left(ik_1|\mathbf{r}_p-\mathbf{s}|-1\right)}{|\mathbf{r}_p-\mathbf{s}|^3}e^{ik_1|\mathbf{r}_p-\mathbf{s}|}\frac{1}{2\pi}\int d\phi\, e^{-im\phi}\mathbf{p}\cdot(\mathbf{r}_p-\mathbf{s}) = \\
&= \frac{1}{\epsilon_1}\frac{(ik_1R-1)}{R^3}e^{ik_1R}\frac{1}{2\pi}\int d\phi\, e^{-im\phi}\left(-p_x\rho_s\cos\phi + p_z(d-z_s)\right) = \\
&= \frac{1}{\epsilon_1}\frac{\left(ik_1|\mathbf{r}_p-\mathbf{s}|-1\right)}{|\mathbf{r}_p-\mathbf{s}|^3}e^{ik_1|\mathbf{r}_p-\mathbf{s}|}\times \\
&\times\left(-\frac{p_x}{2}\rho_s\left(\delta_{m,1}+\delta_{m,-1}\right)+p_z(d-z_s)\,\delta_{m,0}\right)
\end{aligned}$$

For calculating $\boldsymbol{\alpha}$, defined as

$$\boldsymbol{\alpha} = (\mathbf{n}_s\cdot\nabla_s)(\mathbf{A}_2-\mathbf{A}_1) + ik\mathbf{n}_s(\epsilon_1\Phi_1-\epsilon_2\Phi_2) \tag{A.27}$$

we make use of the definition of convective operators in cylindrical coordinates,

$$\begin{aligned}
(\mathbf{v}\cdot\nabla)\mathbf{w} = &\left(v_\rho\frac{\partial w_\rho}{\partial\rho}+\frac{v_\phi}{\rho}\frac{\partial w_\rho}{\partial\phi}+v_z\frac{\partial w_\rho}{\partial z}-\frac{v_\phi}{\rho}w_\phi\right)\hat{\rho}+ \\
&+\left(v_\rho\frac{\partial w_\phi}{\partial\rho}+\frac{v_\phi}{\rho}\frac{\partial w_\phi}{\partial\phi}+v_z\frac{\partial w_\phi}{\partial z}+\frac{v_\phi}{\rho}w_\rho\right)\hat{\phi}+ \\
&+\left(v_\rho\frac{\partial w_z}{\partial\rho}+\frac{v_\phi}{\rho}\frac{\partial w_z}{\partial\phi}+v_z\frac{\partial w_z}{\partial z}\right)\hat{z}.
\end{aligned}$$

Using the symmetry, meaning $\mathbf{n}_\phi = 0$

$$\begin{aligned}
(\mathbf{n}_s\cdot\nabla)\mathbf{A} = &\left(n_\rho\frac{\partial A_\rho}{\partial\rho}+n_z\frac{\partial A_\rho}{\partial z}\right)\hat{\rho}+\left(n_\rho\frac{\partial A_\phi}{\partial\rho}+n_z\frac{\partial A_\phi}{\partial z}\right)\hat{\phi}+ \\
&+\left(n_\rho\frac{\partial A_z}{\partial\rho}+n_z\frac{\partial A_z}{\partial z}\right)\hat{z}.
\end{aligned}$$

Lack of ϕ-dependence also means that the the m-coefficients can be trivially calculated by replacing $\mathbf{A}$ with $\mathbf{A}^m$. Since $\mathbf{A}^m = f(\mathbf{s})\,\mathbf{a}$, with a a constant vector, the derivatives can be expressed as

$$\frac{\partial A^m}{\partial \tau} = \left[\frac{\partial}{\partial R}\left(-ik\frac{e^{ik_1 R}}{R}\right)\right]\frac{\partial\left|\mathbf{r}_p-\mathbf{s}\right|}{\partial\tau} = -ik\frac{(ik_1R-1)\,e^{ik_1R}}{R^3}\,\hat{\tau}\cdot\left(\mathbf{s}-\mathbf{r}_p\right) \tag{A.28}$$

for τ either ρ, z. This gives:

$$\begin{aligned}(\mathbf{n}_s\cdot\nabla)\,\mathbf{A}_1^m = -ik\frac{\left(ik_1\left|\mathbf{r}_p-\mathbf{s}\right|-1\right)e^{ik_1\left|\mathbf{r}_p-\mathbf{s}\right|}}{\left|\mathbf{r}_p-\mathbf{s}\right|^3}\,\left(\mathbf{n}_s\cdot\left(\mathbf{s}-\mathbf{r}_p\right)\right)\times\\ \times\left[\frac{p_x}{2}\left(\delta_{m,1}\left(\hat{\rho}+i\hat{\phi}\right)+\delta_{m,-1}\left(\hat{\rho}-i\hat{\phi}\right)\right)+p_z\delta_{m,0}\,\hat{z}\right]\end{aligned}$$

Such that finally

$$\begin{aligned}\boldsymbol{\alpha}^m &= -\left(\mathbf{n}_s\cdot\nabla_s\right)\mathbf{A}_1 + ik\mathbf{n}_s\epsilon_1\Phi_1 =\\ &= ik\frac{\left(ik_1\left|\mathbf{r}_p-\mathbf{s}\right|-1\right)e^{ik_1\left|\mathbf{r}_p-\mathbf{s}\right|}}{\left|\mathbf{r}_p-\mathbf{s}\right|^3}\times\\ &\times\left\{\left[(d-z_s)\left(\delta_{m,0}\,n_\rho p_z-\frac{1}{2}\left(\delta_{m,1}+\delta_{m,-1}\right)\,n_z p_\rho\right)\right]\hat{\rho}+\right.\\ &+\left[\left(n_\rho\rho_s+n_z\left(z_s-d\right)\right)\frac{i}{2}\left(\delta_{m,1}-\delta_{m,-1}\right)\right]\hat{\phi}+\\ &\left.+\left[n_\rho\rho_s p_z\,\delta_{m,0}-\frac{1}{2}n_z\rho_s p_x\left(\delta_{m,1}+\delta_{m,-1}\right)\right]\hat{z}\right\}\end{aligned}$$

The last source term is defined as

$$D = \mathbf{n}_s\cdot\left[\epsilon_1\left(ik\mathbf{A}_1-\nabla_s\Phi_1\right)-\epsilon_2\left(ik\mathbf{A}_2-\nabla_s\Phi_2\right)\right] = \epsilon_1\mathbf{n}_s\cdot\left(ik\mathbf{A}_1-\nabla_s\Phi_1\right) \tag{A.29}$$

The second term can be calculated in a similar fashion to (A.28). Since

$$\nabla_s\Phi = \frac{\partial\Phi}{\partial\rho}\hat{\rho}+\frac{1}{\rho}\frac{\partial\Phi}{\partial\phi}\hat{\phi}+\frac{\partial\Phi}{\partial z}\hat{z} \tag{A.30}$$

and the second term can be dropped since $n_\phi = 0$. Using

$$\frac{\partial}{\partial R}\frac{(ik_1R-1)}{R^3}e^{ik_1R} = \frac{-k_1^2R^2-3ik_1R+3}{R^4}e^{ik_1R} \tag{A.31}$$

and

$$\frac{\partial\left|\mathbf{r}_p-\mathbf{s}\right|}{\partial\tau} = \frac{\hat{\tau}\cdot\left(\mathbf{s}-\mathbf{r}_p\right)}{\left|\mathbf{r}_p-\mathbf{s}\right|} \tag{A.32}$$

we find

$$\begin{aligned}&\left(\epsilon_1\mathbf{n}_s\cdot\nabla_s\Phi_1\right)^m =\\ &\quad= e^{ik_1\left|\mathbf{r}_p-\mathbf{s}\right|}\left\{\frac{-k_1^2\left|\mathbf{r}_p-\mathbf{s}\right|^2-3ik_1\left|\mathbf{r}_p-\mathbf{s}\right|+3}{\left|\mathbf{r}_p-\mathbf{s}\right|^5}\mathbf{n}_s\cdot\left(\mathbf{s}-\mathbf{r}_p\right)\times\right.\\ &\quad\times\left(-\frac{1}{2}p_x\rho_s\left(\delta_{m,1}+\delta_{m,-1}\right)+p_z\left(d-z_s\right)\delta_{m,0}\right)+\\ &\quad\left.+\frac{\left(ik_1\left|\mathbf{r}_p-\mathbf{s}\right|-1\right)}{\left|\mathbf{r}_p-\mathbf{s}\right|^3}\left(-\frac{1}{2}p_x n_\rho\left(\delta_{m,1}+\delta_{m,-1}\right)-p_z n_z\delta_{m,0}\right)\right\}\end{aligned}$$

note that the inner product $\mathbf{n}_s \cdot (\mathbf{s} - \mathbf{r}_p)$ is invariant to rotations, because of the symmetry and position of the dipole and need not be decomposed to angular components. This result can now be substituted into D to give:

$$\begin{aligned} D^m = & \left\{ \frac{k^2}{|\mathbf{r}_p - \mathbf{s}|} \left(\frac{p_x}{2} n_\rho \left(\delta_{m,1} + \delta_{m,-1} \right) + p_z n_z \delta_{m,0} \right) - \right. \\ & - \frac{\left(ik_1 \left| \mathbf{r}_p - \mathbf{s} \right| - 1 \right)}{\left| \mathbf{r}_p - \mathbf{s} \right|^3} \left(-\frac{1}{2} p_x n_\rho \left(\delta_{m,1} + \delta_{m,-1} \right) - p_z n_z \delta_{m,0} \right) - \\ & - \frac{-k_1^2 \left| \mathbf{r}_p - \mathbf{s} \right|^2 - 3ik_1 \left| \mathbf{r}_p - \mathbf{s} \right| + 3}{\left| \mathbf{r}_p - \mathbf{s} \right|^5} \mathbf{n}_s \cdot \left(\mathbf{s} - \mathbf{r}_p \right) \times \\ & \left. \times \left(-\frac{1}{2} p_x \rho_s \left(\delta_{m,1} + \delta_{m,-1} \right) + p_z \left(d - z_s \right) \delta_{m,0} \right) \right\} e^{ik_1 \left| \mathbf{r}_p - \mathbf{s} \right|} \end{aligned}$$

A.1.4 Far Field Radiation

For the far field, we use the the assumption $r \gg \lambda_{spp}, d$ to write

$$G(|\mathbf{r} - \mathbf{r}'|) = \frac{e^{ikr}}{r} e^{-ik\hat{\mathbf{r}} \cdot \mathbf{r}'} \tag{A.33}$$

Which, upon introduction of a radial direction

$$\mathbf{A} = \frac{e^{ikr}}{r} \left[-ik\mathbf{p} e^{-ikd\cos\theta} + \int ds\, e^{-ik\hat{\mathbf{r}} \cdot \mathbf{s}} \mathbf{h}(s) \right] \tag{A.34}$$

The power radiated per solid angle is given by

$$\frac{dP}{d\Omega} = \frac{c}{8\pi} \Re \left(r^2 \hat{\mathbf{r}} \cdot \mathbf{E} \times \mathbf{H}^* \right). \tag{A.35}$$

Note, that since $\mathbf{E} = ik\mathbf{A} - \nabla\Phi$ and $\Phi \propto e^{ikr}/r$, the gradient of Φ is in the radial direction and proportional to $\frac{1}{r^2}$, and does not contribute to the radiated power. Therefore

$$\frac{dP}{d\Omega} = \frac{c}{8\pi} \Re \left(r^2 \hat{\mathbf{r}} \cdot \left((ik\mathbf{A}) \times (\nabla \times \mathbf{A})^* \right) \right). \tag{A.36}$$

For the calculation of $\mathbf{A}$, we use

$$\begin{aligned} \int ds\, e^{-ik_1 \hat{\mathbf{r}} \cdot \mathbf{s}} \mathbf{h}(s) &= \int ds\, e^{-ik_1 (\rho_s \cos(\phi - \phi_s) \sin\theta + z_s \cos\theta)} \mathbf{h}(s) = \\ &= \int d\phi_s \int \rho_s d\rho_s\, \mathfrak{F}(\rho_s)\, e^{-ik_1 z_s \cos\theta} e^{-ik_1 \rho_s \sin(\frac{\pi}{2} - \phi + \phi_s) \sin\theta} \mathbf{h}(s) = \\ &= \int d\phi_s \int \rho_s d\rho_s\, \mathfrak{F}(\rho_s)\, e^{-ik_1 z_s \cos\theta} \times \\ &\times \left(\sum_{n=-\infty}^{\infty} J_n(k_1 \rho_s \sin\theta) e^{-in(\frac{\pi}{2} - \phi + \phi_s)} \right) \mathbf{h}(s), \end{aligned}$$

where $\mathfrak{F}(\rho_s) = \sqrt{1 + \left. \frac{dz}{d\rho} \right|_{\rho_2}^2}$. treating this integral in the same way as the near field Green's function we define

$$[G_m^{far\ field}]_a = 2\pi \int_{\rho_a - \Delta\rho}^{\rho_a + \Delta\rho} \rho_s d\rho_s\, \mathfrak{F}(\rho_s)\, e^{-ik_1 z_s \cos\theta} J_m(k_1 \rho_s \sin\theta) e^{-\frac{im\pi}{2}}, \tag{A.37}$$

leading to

$$A_r^m = \frac{e^{ik_1 r}}{r}\left[-i2k\pi\left(\frac{1}{2}p_x\sin\theta(\delta_{m,1}+\delta_{m,-1})+p_z\cos\theta\delta_{m,0}\right)e^{-ik_1 d\cos\theta}+\right.$$
$$\left.+\frac{1}{2}\left(G_{m+1}^{far\,field}(h_\rho^m+ih_\phi^m)+G_{m-1}^{far\,field}(h_\rho^m-ih_\phi^m)\right)\sin\theta+G_m^{far\,field}h_z^m\cos\theta\right]$$
$$A_\phi^m = \frac{e^{ik_1 r}}{r}\left[k\pi p_x(\delta_{m,-1}-\delta_{m,1})e^{-ik_1 d\cos\theta}+\right.$$
$$\left.+\frac{i}{2}\left(-G_{m+1}^{far\,field}(h_\rho^m+ih_\phi^m)+G_{m-1}^{far\,field}(h_\rho^m-ih_\phi^m)\right)\right]$$
$$A_\theta^m = \frac{e^{ik_1 r}}{r}\left[-i2k\pi\left(\frac{1}{2}p_x\cos\theta(\delta_{m,1}+\delta_{m,-1})-p_z\sin\theta\delta_{m,0}\right)e^{-ik_1 d\cos\theta}+\right.$$
$$\left.+\frac{1}{2}\left(G_{m+1}^{far\,field}(h_\rho^m+ih_\phi^m)+G_{m-1}^{far\,field}(h_\rho^m-ih_\phi^m)\right)\cos\theta-G_m^{far\,field}h_z^m\sin\theta\right].$$

Together with (where only terms proportional to $\frac{1}{r}$ are kept)

$$(\nabla\times\mathbf{A})_\phi = \frac{1}{r}\frac{\partial}{\partial r}(rA_\theta) = ik_1A_\theta$$
$$(\nabla\times\mathbf{A})_\theta = -\frac{1}{r\sin\theta}\frac{\partial}{\partial r}(r\sin\theta A_\phi) = -ik_1A_\phi$$

gives

$$\frac{dP}{d\Omega}^m = \frac{ckk_1}{8\pi}\Re\left(\left|-i2k\pi\left(\frac{1}{2}p_x\cos\theta(\delta_{m,1}+\delta_{m,-1})-p_z\sin\theta\delta_{m,0}\right)e^{-ik_1 d\cos\theta}+\right.\right.$$
$$+\frac{1}{2}\left(G_{m+1}^{far\,field}(h_\rho^m+ih_\phi^m)+G_{m-1}^{far\,field}(h_\rho^m-ih_\phi^m)\right)\cos\theta-G_m^{far\,field}h_z^m\sin\theta\Big|^2$$
$$+\left|k\pi p_x(\delta_{m,-1}-\delta_{m,1})e^{-ik_1 d\cos\theta}+\right.$$
$$\left.\left.+\frac{i}{2}\left(-G_{m+1}^{far\,field}(h_\rho^m+ih_\phi^m)+G_{m-1}^{far\,field}(h_\rho^m-ih_\phi^m)\right)\right|^2\right)$$

List of Figures

Bibliography

[Agam92] Oded Agam, Shmuel Fishman, and R. Prange, *Experimental realizations of quantum chaos in dielectric waveguides*, Physical Review A, **45**(9), 6773 (1992)

[Akimov07] A V Akimov, A Mukherjee, C L Yu, D E Chang, A S Zibrov, P R Hemmer, H Park, and M D Lukin, *Generation of single optical plasmons in metallic nanowires coupled to quantum dots.*, Nature, **450**(7168), 402 (2007)

[Andersen10] Mads Lykke Andersen, Sø ren Stobbe, Anders Sø ndberg Sø rensen, and Peter Lodahl, *Strongly modified plasmon-matter interaction with mesoscopic quantum emitters*, Nature Physics, **7**(3), 215 (2010)

[Aouani11a] Heykel Aouani, Oussama Mahboub, Nicolas Bonod, Eloïse Devaux, Evgeny Popov, Hervé Rigneault, Thomas W Ebbesen, and Jérôme Wenger, *Bright unidirectional fluorescence emission of molecules in a nanoaperture with plasmonic corrugations.*, Nano letters, **11**(2), 637 (2011)

[Aouani11b] Heykel Aouani, Oussama Mahboub, Eloïse Devaux, Hervé Rigneault, Thomas W Ebbesen, and Jérôme Wenger, *Plasmonic antennas for directional sorting of fluorescence emission.*, Nano letters, **11**(6), 2400 (2011)

[Archambault10] Alexandre Archambault, Francois Marquier, Jean-Jacques Greffet, and Christophe Arnold, *Quantum theory of spontaneous and stimulated emission of surface plasmons*, Physical Review B, **82**(3) (2010)

[Arndt99] Markus Arndt, Olaf Nairz, Julian Vos-Andreae, Claudia Keller, Gerbrand van der Zouw, and Anton Zeilinger, *Wave-particle duality of C60 molecules*, Nature, **401**(6754), 680 (1999)

[Babadjanyan00] a. J. Babadjanyan, N. L. Margaryan, and Kh. V. Nerkararyan, *Superfocusing of surface polaritons in the*

conical structure, Journal of Applied Physics, **87**(8), 3785 (2000)

[Ballester09] D. Ballester, M. Tame, C. Lee, J. Lee, and M. Kim, *Long-range surface-plasmon-polariton excitation at the quantum level*, Physical Review A, **79**(5) (2009)

[Bednorz11] Adam Bednorz and Wolfgang Belzig, *Fourth moments reveal the negativity of the Wigner function*, Phys. Rev. A, **83**(5), 52113 (2011)

[Bender98] Carl Bender and Stefan Boettcher, *Real Spectra in Non-Hermitian Hamiltonians Having PT Symmetry*, Physical Review Letters, **80**(24), 5243 (1998)

[Benichi11] Hugo Benichi and Akira Furusawa, *Optical homodyne tomography with polynomial series expansion*, Phys. Rev. A, **84**, 032104 (2011)

[Bergmann98] K. Bergmann, B. W. Shore, H. Theuer, B. Shore, and BW Shore, *Coherent population transfer among quantum states of atoms and molecules*, Reviews of Modern Physics, **70**(3), 1003 (1998)

[Boardman82] A.D. Boardman, *Electromagnetic Surface Modes*, John Wiley & Sons Ltd (1982)

[Bochner33] S. Bochner, *Monotone Funktionen, Stieltjessche Integrale und harmonische Analyse*, Mathematische Annalen, **108**(1), 378 (1933)

[Born28] M. Born and V. Fock, *Beweis des Adiabatensatzes*, Zeitschrift für Physik, **51**(3-4), 165 (1928)

[Born99] Max Born and Emil Wolf, *Principles of Optics: Electromagnetic Theory of Propagation, Interference and Diffraction of Light*, Cambridge University Press (1999)

[Bulu11] Irfan Bulu, Thomas Babinec, Birgit Hausmann, Jennifer T. Choy, and Marko Loncar, *Plasmonic resonators for enhanced diamond NV- center single photon sources*, Optics Express, **19**(6), 5268 (2011)

[Carretero-Palacios11] S. Carretero-Palacios, O. Mahboub, F. J. Garcia-Vidal, L. Martin-Moreno, Sergio G. Rodrigo, C. Genet, and T. W. Ebbesen, *Mechanisms for extraordinary optical transmission through bull's eye structures*, Optics Express, **19**(11), 10429 (2011)

[Catrysse05] Peter B. Catrysse, Hocheol Shin, and Shanhui Fan, *Propagating modes in subwavelength cylindrical holes*, Journal of Vacuum Science & Technology B: Microelectronics and Nanometer Structures, **23**(6), 2675 (2005)

[Chan11] Jasper Chan, T P Mayer Alegre, Amir H Safavi-Naeini, Jeff T Hill, Alex Krause, Simon Gröblacher, Markus Aspelmeyer, and Oskar Painter, *Laser cooling of a nanomechanical oscillator into its quantum ground state.*, Nature, **478**(7367), 89 (2011)

[Chang06] D. Chang, A. Sø rensen, P. Hemmer, and M. Lukin, *Quantum Optics with Surface Plasmons*, Physical Review Letters, **97**(5), 53002 (2006)

[Chang07a] —, *Strong coupling of single emitters to surface plasmons*, Physical Review B, **76**(3), 35420 (2007)

[Chang07b] Darrick E. Chang, Anders S. Sø rensen, Eugene A. Demler, and Mikhail D. Lukin, *A single-photon transistor using nanoscale surface plasmons*, Nature Physics, **3**(11), 807 (2007)

[Dzsotjan10] David Dzsotjan, Anders Sø rensen, and Michael Fleischhauer, *Quantum emitters coupled to surface plasmons of a nanowire: A Green's function approach*, Physical Review B, **82**(7), 1 (2010)

[Falk09] Abram L. Falk, Frank H. L. Koppens, Chun L. Yu, Kibum Kang, Nathalie de Leon Snapp, Alexey V. Akimov, Moon-Ho Jo, Mikhail D. Lukin, and Hongkun Park, *Near-field electrical detection of optical plasmons and single-plasmon sources*, Nature Physics, **5**(7), 475 (2009)

[Fernholz08] T. Fernholz, H. Krauter, K. Jensen, J. F. Sherson, A. S. Sørensen, and E. S. Polzik, *Spin Squeezing of Atomic Ensembles via Nuclear-Electronic Spin Entanglement*, Phys. Rev. Lett., **101**, 073601 (2008)

[Furusawa98] A. Furusawa, J. L. Sørensen, S. L. Braunstein, C. A. Fuchs, H. J. Kimble, and E. S. Polzik, *Unconditional Quantum Teleportation*, Science, **282**(5389), 706 (1998), `http://www.sciencemag.org/content/282/5389/706.full.pdf`

[García de Abajo02] F. García de Abajo and a. Howie, *Retarded field calculation of electron energy loss in inhomogeneous dielectrics*, Physical Review B, **65**(11), 1 (2002)

[Garcia-Vidal10a] F. J. Garcia-Vidal, T. W. Ebbesen, and L. Kuipers, *Light passing through subwavelength apertures*, Reviews of Modern Physics, **82**(1), 729 (2010)

[Garcia-Vidal10b] F. J. Garcia-Vidal, L. Martin-Moreno, T. W. Ebbesen, and L. Kuipers, *Light passing through subwavelength apertures*, Rev. Mod. Phys., **82**, 729 (2010)

[Gonzalez-Tudela11] A. Gonzalez-Tudela, D. Martin-Cano, E. Moreno, L. Martin-Moreno, C. Tejedor, and F. Garcia-Vidal, *Entanglement of Two Qubits Mediated by One-Dimensional Plasmonic Waveguides*, Physical Review Letters, **106**(2) (2011)

[Gonzalez-Tudela12] A. Gonzalez-Tudela, P. A. Huidobro, L. Martin-Moreno, C. Tejedor, and F. J. Garcia-Vidal, *Theory of the strong coupling between quantum emitters and propagating surface plasmons*, 5 (2012), 1205.3938

[Gramotnev05] D. K. Gramotnev, *Adiabatic nanofocusing of plasmons by sharp metallic grooves: Geometrical optics approach*, Journal of Applied Physics, **98**(10), 104302 (2005)

[Gramotnev07] Dmitri Gramotnev, David Pile, Michael Vogel, and Xiang Zhang, *Local electric field enhancement during nanofocusing of plasmons by a tapered gap*, Physical Review B, **75**(3), 2 (2007)

[Gramotnev08] D. K. Gramotnev, K. C. Vernon, and D. F. P. Pile, *Directional coupler using gap plasmon waveguides*, Applied Physics B, **93**(1), 99 (2008)

[Grønbech-Jensen10] Niels Grønbech-Jensen, Jeffrey E. Marchese, Matteo Cirillo, and James A. Blackburn, *Tomography and Entanglement in Coupled Josephson Junction Qubits*, Phys. Rev. Lett., **105**, 010501 (2010)

[Hammerer10] Klemens Hammerer, Anders S. Sørensen, and Eugene S. Polzik, *Quantum interface between light and atomic ensembles*, Rev. Mod. Phys., **82**, 1041 (2010)

[Hradil97] Z. Hradil, *Quantum-state estimation*, Phys. Rev. A, **55**, R1561 (1997)

[Huck09] Alexander Huck, Stephan Smolka, Peter Lodahl, Anders Sø rensen, Alexandra Boltasseva, Jiri Janousek, and Ulrik Andersen, *Demonstration of Quadrature-Squeezed Surface Plasmons in a Gold Waveguide*, Physical Review Letters, **102**(24) (2009)

[Johnson72] P. B. Johnson and R. W. Christy, *Optical Constants of the Noble Metals*, Physical Review B, **6**(12), 4370 (1972)

[Jun11] Young Chul Jun, Kevin C Y Huang, and Mark L Brongersma, *Plasmonic beaming and active control over fluorescent emission.*, Nature communications, **2**, 283 (2011)

[Kiesel11] T. Kiesel, W. Vogel, B. Hage, and R. Schnabel, *Direct Sampling of Negative Quasiprobabilities of a Squeezed State*, Phys. Rev. Lett., **107**, 113604 (2011)

[Kimble08] H J Kimble, *The quantum internet.*, Nature, **453**(7198), 1023 (2008)

[Klimov04] V. Klimov and M. Ducloy, *Spontaneous emission rate of an excited atom placed near a nanofiber*, Physical Review A, **69**(1) (2004)

[Klyachko08] Alexander A. Klyachko, M. Ali Can, Sinem Binicioğlu, and Alexander S. Shumovsky, *Simple Test for Hidden Variables in Spin-1 Systems*, Phys. Rev. Lett., **101**, 020403 (2008)

[Knight03] Jonathan C Knight, *Photonic crystal fibres.*, Nature, **424**(6950), 847 (2003)

[Kolesov09] Roman Kolesov, Bernhard Grotz, Gopalakrishnan Balasubramanian, Rainer J. Stöhr, Aurélien A. L. Nicolet, Philip R. Hemmer, Fedor Jelezko, and Jörg Wrachtrup, *Wave-particle duality of single surface plasmon polaritons*, Nature Physics, **5**(7), 470 (2009)

[Korbicz05] J. K. Korbicz, J. I. Cirac, Jan Wehr, and M. Lewenstein, *Hilbert's 17th Problem and the Quantumness of States*, Phys. Rev. Lett., **94**, 153601 (2005)

[Kretschmann68] E Kretschmann and H Raether, *Radiative decay of non radiative surface plasmons excited by light*, Zeitschrift für Naturforschung A, **23**, 2135 (1968)

[Kurokawa07] Yoichi Kurokawa and Hideki Miyazaki, *Metal-insulator-metal plasmon nanocavities: Analysis of optical properties*, Physical Review B, **75**(3) (2007)

[Lalanne05] P. Lalanne, J. Hugonin, and J. Rodier, *Theory of Surface Plasmon Generation at Nanoslit Apertures*, Physical Review Letters, **95**(26) (2005)

[Lapkiewicz11] Radek Lapkiewicz, Peizhe Li, Christoph Schaeff, Nathan K Langford, Sven Ramelow, Marcin Wieśniak, and Anton Zeilinger, *Experimental non-classicality of an indivisible quantum system.*, Nature, **474**(7352), 490 (2011)

[Lee11a] K. G. Lee, X. W. Chen, H. Eghlidi, P. Kukura, R. Lettow, A. Renn, V. Sandoghdar, and S. Götzinger, *A planar dielectric antenna for directional single-photon emission and near-unity collection efficiency*, Nature Photonics, **5**(3), 166 (2011)

[Lee11b] Noriyuki Lee, Hugo Benichi, Yuishi Takeno, Shuntaro Takeda, James Webb, Elanor Huntington, and Akira Furusawa, *Teleportation of Nonclassical Wave Packets of Light*, Science, **332**(6027), 330 (2011), `http://www.sciencemag.org/content/332/6027/330.full.pdf`

[Leggett85] A. J. Leggett and Anupam Garg, *Quantum mechanics versus macroscopic realism: Is the flux there when nobody looks?*, Phys. Rev. Lett., **54**, 857 (1985)

[Leibfried96] D. Leibfried, D. M. Meekhof, B. E. King, C. Monroe, W. M. Itano, and D. J. Wineland, *Experimental Determination of the Motional Quantum State of a Trapped Atom*, Phys. Rev. Lett., **77**, 4281 (1996)

[Leonhardt05] Ulf Leonhardt, *Measuring the Quantum State of Light (Cambridge Studies in Modern Optics)*, Cambridge University Press (2005)

[Lerman09] Gilad M Lerman, Avner Yanai, and Uriel Levy, *Demonstration of nanofocusing by the use of plasmonic lens illuminated with radially polarized light.*, Nano letters, **9**(5), 2139 (2009)

[Leskova85] T.A. Leskova and N.I. Gapotchenko, *Fabry-Perot type interferrometer for surface polaritons: Resonance effects*, Solid State Communications, **53**(4), 351 (1985)

[Lezec02] H J Lezec, A Degiron, E Devaux, R A Linke, L Martin-Moreno, F J Garcia-Vidal, and T W Ebbesen, *Beaming light from a subwavelength aperture.*, Science (New York, N.Y.), **297**(5582), 820 (2002)

[Liu05] Zhaowei Liu, Jennifer M Steele, Werayut Srituravanich, Yuri Pikus, Cheng Sun, and Xiang Zhang, *Focusing surface plasmons with a plasmonic lens.*, Nano letters, **5**(9), 1726 (2005)

[Longhi07] S. Longhi, G. Della Valle, M. Ornigotti, and P. Laporta, *Coherent tunneling by adiabatic passage in an optical waveguide system*, Physical Review B, **76**(20), 201101 (2007)

[López-Tejeira07] F. López-Tejeira, Sergio G. Rodrigo, L. Martín-Moreno, F. J. García-Vidal, E. Devaux, T. W. Ebbesen, J. R. Krenn, I. P. Radko, S. I. Bozhevolnyi, M. U. González, J. C. Weeber, and A. Dereux, *Efficient unidirectional nanoslit couplers for surface plasmons*, Nature Physics, **3**(5), 324 (2007)

[Lvovsky01] A I Lvovsky, H Hansen, T Aichele, O Benson, J Mlynek, and S Schiller, *Quantum State Reconstruction of the Single-Photon Fock State*, Phys. Rev. Lett., **87**(5), 50402 (2001)

[Lvovsky09] A. I. Lvovsky and M. G. Raymer, *Continuous-variable optical quantum-state tomography*, Rev. Mod. Phys., **81**, 299 (2009)

[Mandel95] Leonard Mandel and Emil Wolf, *Optical Coherence and Quantum Optics*, Cambridge University Press (1995)

[Mari11] A. Mari, K. Kieling, B. Melholt Nielsen, E. S. Polzik, and J. Eisert, *Directly Estimating Nonclassicality*, Phys. Rev. Lett., **106**, 010403 (2011)

[Martín-Cano10] Diego Martín-Cano, Luis Martín-Moreno, Francisco J García-Vidal, and Esteban Moreno, *Resonance energy transfer and superradiance mediated by plasmonic nanowaveguides.*, Nano letters, **10**(8), 3129 (2010)

[Martín-Cano11] Diego Martín-Cano, Alejandro González-Tudela, L. Martín-Moreno, F. García-Vidal, Carlos Tejedor, and Esteban Moreno, *Dissipation-driven generation of two-qubit entanglement mediated by plasmonic waveguides*, Physical Review B, **84**(23) (2011)

[Mills75] D. Mills, *Attenuation of surface polaritons by surface roughness*, Physical Review B, **12**(10), 4036 (1975)

[Mišta10] Ladislav Mišta, Radim Filip, and Akira Furusawa, *Continuous-variable teleportation of a negative Wigner function*, Phys. Rev. A, **82**, 012322 (2010)

[Miyazaki06] Hideki T. Miyazaki and Yoichi Kurokawa, *Controlled plasmon resonance in closed metal/insulator/metal nanocavities*, Applied Physics Letters, **89**(21), 211126 (2006)

[Morandotti99] R. Morandotti, U. Peschel, J. Aitchison, H. Eisenberg, and Y. Silberberg, *Experimental Observation of Linear and Nonlinear Optical Bloch Oscillations*, Physical Review Letters, **83**(23), 4756 (1999)

[Mostafazadeh02] Ali Mostafazadeh, *Pseudo-Hermiticity versus PT symmetry: The necessary condition for the reality of the spectrum of a non-Hermitian Hamiltonian*, Journal of Mathematical Physics, **43**(1), 205 (2002)

[Neergaard-Nielsen07] J S Neergaard-Nielsen, B M Nielsen, H Takahashi, A I Vistnes, and E S Polzik, *High purity bright single photon source*, Opt. Express, **15**(13), 7940 (2007)

[Nha08] Hyunchul Nha, *Complete conditions for legitimate Wigner distributions*, Phys. Rev. A, **78**(1), 12103 (2008)

[Nielsen04] Michael A. Nielsen and Isaac L. Chuang, *Quantum Computation and Quantum Information (Cambridge Series on Information and the Natural Sciences)*, Cambridge University Press (2004)

[Novotny94] L. Novotny and C. Hafner, *Light propagation in a cylindrical waveguide with a complex, metallic, dielectric function*, Physical Review E, **50**(5), 4094 (1994)

[Ong93] T.T. Ong, V. Celli, and A.A. Maradudin, *The impedance of a curved surface*, Optics Communications, **95**(1-3), 1 (1993)

[Otto68] Andreas Otto, *Excitation of nonradiative surface plasma waves in silver by the method of frustrated total reflection*, Zeitschrift für Physik, **216**(4), 398 (1968)

[Ourjoumtsev06] Alexei Ourjoumtsev, Rosa Tualle-Brouri, and Philippe Grangier, *Quantum Homodyne Tomography of a Two-Photon Fock State*, Phys. Rev. Lett., **96**, 213601 (2006)

[Peierls76] Rudolf Peierls, *The Momentum of Light in a Refracting Medium*, Proceedings of the Royal Society of London. Series A, Mathematical and Physical Sciences (1934-1990), **347**(1651), 475 (1976)

[Pertsch99] T. Pertsch, P. Dannberg, W. Elflein, A. Bräuer, and F. Lederer, *Optical Bloch Oscillations in Temperature Tuned Waveguide Arrays*, Physical Review Letters, **83**(23), 4752 (1999)

[Pitarke07] J M Pitarke, V M Silkin, E V Chulkov, and P M Echenique, *Theory of surface plasmons and surface-plasmon polaritons*, Reports on Progress in Physics, **70**(1), 1 (2007), `0611257v1`

[Polzik92] E. Polzik, J. Carri, and H. Kimble, *Spectroscopy with squeezed light*, Physical Review Letters, **68**(20), 3020 (1992)

[Popov05] Evgeny Popov, Nicolas Bonod, Michel Neviï¿½re, Hervï¿½ Rigneault, Pierre-Franï¿½ois Lenne, and Patrick Chaumet, *Surface plasmon excitation on a single subwavelength hole in a metallic sheet*, Applied Optics, **44**(12), 2332 (2005)

[Regal08] C. A. Regal, J. D. Teufel, and K. W. Lehnert, *Measuring nanomechanical motion with a microwave cavity interferometer*, Nature Physics, **4**(7), 555 (2008)

[Sakoda05] Kazuaki Sakoda, *Optical Properties of Photonic Crystals*, vol. 80 of *Springer Series in Optical Sciences*, Berlin/Heidelberg: Springer-Verlag (2005)

[Schwartz07] Tal Schwartz, Guy Bartal, Shmuel Fishman, and Mordechai Segev, *Transport and Anderson localization in disordered two-dimensional photonic lattices.*, Nature, **446**(7131), 52 (2007)

[Shchukin04] E Shchukin, Th Richter, and W Vogel, *Nonclassical quadrature distributions*, Journal of Optics B: Quantum and Semiclassical Optics, **6**(6), S597 (2004)

[Sipe81] J E Sipe, *The dipole anten&a problem in surface physics: a new approach j.e. sipe **, Surface Science, **5**, 489 (1981)

[Smith04] D R Smith, J B Pendry, and M C K Wiltshire, *Metamaterials and negative refractive index.*, Science (New York, N.Y.), **305**(5685), 788 (2004)

[Snyder65] A. Snyder, *Surface mode coupling along a tapered dielectric rod*, IEEE Transactions on Antennas and Propagation, **13**(5), 821 (1965)

[Snyder83] Allan W Snyder and J. D. (John D.) Love, *Optical waveguide theory / Allan W. Snyder, John D. Love*, London ; New York : Chapman and Hall (1983), includes bibliographical references and indexes

[Steele06] Jennifer M. Steele, Zhaowei Liu, Yuan Wang, and Xiang Zhang, *Resonant and non-resonant generation and focusing of surface plasmons with circular gratings*, Optics Express, **14**(12), 5664 (2006)

[Stockman04] Mark Stockman, *Nanofocusing of Optical Energy in Tapered Plasmonic Waveguides*, Physical Review Letters, **93**(13), 1 (2004)

[Sudarshan63] E C G Sudarshan, *Equivalence of Semiclassical and Quantum Mechanical Descriptions of Statistical Light Beams*, Phys. Rev. Lett., **10**(7), 277 (1963)

[Teufel11] J D Teufel, T Donner, Dale Li, J W Harlow, M S Allman, K Cicak, A J Sirois, J D Whittaker, K W Lehnert, and R W Simmonds, *Sideband cooling of micromechanical motion to the quantum ground state.*, Nature, **475**(7356), 359 (2011)

[Toigo77] F. Toigo, A. Marvin, V. Celli, and N. Hill, *Optical properties of rough surfaces: General theory and the small roughness limit*, Physical Review B, **15**(12), 5618 (1977)

[Tong03] Limin Tong, Rafael R Gattass, Jonathan B Ashcom, Sailing He, Jingyi Lou, Mengyan Shen, Iva Maxwell, and Eric Mazur, *Subwavelength-diameter silica wires for low-loss optical wave guiding.*, Nature, **426**(6968), 816 (2003)

[Verhagen09] Ewold Verhagen, Marko Spasenović, Albert Polman, and L. Kuipers, *Nanowire Plasmon Excitation by Adiabatic Mode Transformation*, Physical Review Letters, **102**(20) (2009)

[Veronis08] Georgios Veronis and Shanhui Fan, *Crosstalk between three-dimensional plasmonic slot waveguides*, Optics Express, **16**(3), 2129 (2008)

[Vetsch10] E. Vetsch, D. Reitz, G. Sagué, R. Schmidt, S. T. Dawkins, and A. Rauschenbeutel, *Optical Interface Created by Laser-Cooled Atoms Trapped in the Evanescent Field Surrounding an Optical Nanofiber*, Physical Review Letters, **104**(20) (2010)

[Vogel00] Werner Vogel, *Nonclassical States: An Observable Criterion*, Phys. Rev. Lett., **84**(9), 1849 (2000)

[Weigert03] Stefan Weigert, *Completeness and orthonormality in PT-symmetric quantum systems*, Physical Review A, **68**(6) (2003)

[Welsch99] Dirk-Gunnar Welsch, Werner Vogel, and TomÃ¡Å¡ OpatrnÃ$\frac{1}{2}$, *II Homodyne Detection and Quantum-State Reconstruction*, Elsevier, vol. 39 of *Progress in Optics*, 63 – 211 (1999)

[Wigner32] E Wigner, *On the Quantum Correction For Thermodynamic Equilibrium*, Phys. Rev., **40**(5), 749 (1932)

[Witthaut12] D. Witthaut, M. D. Lukin, and A. S. Sø rensen, *Photon sorters and QND detectors using single photon emitters*, EPL (Europhysics Letters), **97**(5), 50007 (2012)

[Yanai09] Avner Yanai and Uriel Levy, *Plasmonic focusing with a coaxial structure illuminated by radially polarized light*, Optics Express, **17**(2), 924 (2009)

[Zavatta04] Alessandro Zavatta, Silvia Viciani, and Marco Bellini, *Tomographic reconstruction of the single-photon Fock state by high-frequency homodyne detection*, Phys. Rev. A, **70**, 053821 (2004)

[Zayats03] Anatoly V Zayats and Igor I Smolyaninov, *Near-field photonics: surface plasmon polaritons and localized surface plasmons*, Journal of Optics A: Pure and Applied Optics, **5**(4), S16 (2003)

[Zhang10] Maoguo Zhang, Jinglei Du, Haofei Shi, Shaoyun Yin, Liangping Xia, Baohua Jia, Min Gu, and Chunlei Du, *Three-dimensional nanoscale far-field focusing of radially polarized light by scattering the SPPs with an annular groove.*, Optics express, **18**(14), 14664 (2010)